HelmholtzZentrum münchen
German Research Center for Environmental Health

Development and test of a new scanning geometry for Computed Tomography

PhD Thesis
of
Hugo de las Heras

Sinolegala, 2008

Gedruckt mit Unterstützung des
Deutschen Akademischen Austauschdienstes

TECHNISCHE UNIVERSITÄT MÜNCHEN

Helmholtz Zentrum München, Institut für Strahlenschutz

Development and test of a new scanning geometry for Computed Tomography

Hugo de las Heras Gala

Vollständiger Abdruck der von der Fakultät für Physik der Technischen Universität München zur Erlangung des akademischen Grades eines

Doktors der Naturwissenschaften

genehmigten Dissertation.

Vorsitzender: Univ.-Prof. Dr. J. L. van Hemmen

Prüfer der Dissertation:

1. Hon.-Prof. Dr. H. G. Paretzke
2. Univ.-Prof. Dr. K. Schreckenbach

Die Dissertation wurde am 30.10.2008 bei der Technischen Universität München eingereicht und durch die Fakultät für Physik am 19.01.2009 angenommen.

“Das Urbild eines guten Kunstwerks ist nicht eine wirkliche, lebende Gestalt,
obwohl sie der Anlass dazu sein kann”

- Goldmund von Hermann Hesse.

Contents

Zusammenfassung **vii**

1 Introduction **1**
- 1.1 Milestones of Computed Tomography . . . 2
- 1.2 Current systems for Computed Tomography . . . 2
  - 1.2.1 Data acquisition in a CT-scanner . . . 3
  - 1.2.2 Intrinsic drawbacks of current CT-scanners . . . 4
- 1.3 Collective dose from Computed Tomography . . . 5
- 1.4 Concern about health effects of low-dose radiation . . . 7

2 Theoretical Background **9**
- 2.1 A new scanning geometry . . . 9
  - 2.1.1 Description of the concept . . . 9
  - 2.1.2 The two kinds of Radon Data . . . 11
  - 2.1.3 The case of this work . . . 12
- 2.2 The OPED reconstruction algorithm . . . 15
  - 2.2.1 The relation to the scanning geometry . . . 15
  - 2.2.2 Mathematical introduction . . . 17
  - 2.2.3 The reconstruction formula . . . 19
  - 2.2.4 Intuitive explanation . . . 20
  - 2.2.5 Comparison of OPED to Filtered BackProjection . . . 21
- 2.3 Image quality assessment . . . 22
  - 2.3.1 Reconstruction accuracy . . . 22
  - 2.3.2 Spatial Resolution . . . 23

I Simulation studies **25**

3 Dosimetric radiation transport simulation **27**
- 3.1 Parameters of the simulation . . . 27
- 3.2 Results . . . 28
- 3.3 Correction for scattered radiation . . . 28

4 Sinogram interpolation **31**
- 4.1 The need for interpolation . . . 31
- 4.2 Test objects and methods . . . 33
- 4.3 1-D interpolation . . . 34
  - 4.3.1 The interpolating functions . . . 34

4.3.2 The drawback of our 1-D interpolation 35
4.4 2-D interpolation 37
4.5 Results 38
4.5.1 1-D interpolation 38
4.5.2 2-D interpolation 41

II Experimental Part 47

5 Materials and Methods 49
5.1 A test-device for CT D'OR 49
5.1.1 Design 49
5.1.2 Detectors 51
5.1.3 Shielding elements 52
5.1.4 Data acquisition software 53
5.1.5 The rotation desk 53
5.2 Test objects 53
5.2.1 Organic phantoms 53
5.2.2 Plexiglas semi-disk phantoms 54
5.2.3 Head-slice phantom 55
5.3 First experimental set-up 56
5.3.1 Detector Calibration 56
5.3.2 Homogenization factors 58
5.3.3 Data acquisition 59
5.3.4 Empty scan 60
5.4 Second experimental set-up 62
5.4.1 Clinical C-arm device 62
5.4.2 The slice width 63
5.4.3 Conformance of both detector sets 64
5.4.4 Data acquisition 66

6 Data Treatment 67
6.1 Operations needed for each data set 67
6.1.1 Data from the mask detectors 67
6.1.2 Data from the flat panel detector 70
6.2 The data set merging into the full sinogram 72
6.3 The reconstruction code-program OPED 73

7 Results 75
7.1 Results from the first set-up 75
7.1.1 The first reconstruction: a pepper slice 76
7.1.2 Other organic phantom reconstructions 76
7.1.3 Image quality assessment 81
7.2 Results from the set-up with flat panel detector 83
7.2.1 The two independent data sets 83
7.2.2 The final combined reconstruction 87

8 Discussion **89**
8.1 Image Quality 89
8.2 Drawbacks of the test-device developed in this work 90
8.2.1 Different detector sensitivities 92
8.3 Comparison to conventional devices 92
8.4 Problems with the clinical C-arm device 96
8.4.1 Heel effect 96
8.4.2 Automatic brightness normalization 96

9 Summary and Outlook **97**
9.1 Experimental dosimetric comparison 97
9.2 Suggestions for an improved prototype 98

Bibliography **101**

Acknowledgments **113**

Appendix **115**
Appendix A: Technical properties of CsI(Tl) 116
Appendix B: Technical properties of the x-ray tube at the HMGU 117
Appendix C: Curriculum Vitae 118

Front-page image: sinogram of two circles with different radius, scanned over 180°.
First-page sentence: "The original idea of a good piece of art is not a real, living figure, although such a figure can be the motivation for it" (Goldmund by Hermann Hesse).

Abbreviations

All abbreviations are introduced in the text, but a list of them is included here for easy reference:

CT	Computed Tomography
DICOM	Digital Imaging and Communications in Medicine
ED	External Detector
EFOMP	European Federations of Organizations of Medical Physics
FBP	Filtered Back-Projection
GSF	Gesellschaft für Strahlenforschung
Gy	Gray
HMGU	Helmholtz Zentrum München (German Research Center for Environmental Health)
IDL	Interactive Data Language
ICRP	International Comission on Radiological Protection
LNT	linear no threshold
MTF	Modulation Transfer Function
NMSE	Normalized Mean Standard Error
NPS	Noise Power Spectrum
OPED	Orthogonal Polynomial Expansion on Disc
PSF	Point Spread Function
PTB	Physikalisch-Technische Bundesanstalt
Sv	Sievert
SSDL	Secondary Standard Dosimetry Laboratory
TLD	Thermoluminiscence Dosimeter
TPS	Thin Plate Spline
TUM	Technical University of Munich

Zusammenfassung

Diese Arbeit präsentiert eine neue Scangeometrie für Computertomographie mit doppelter optimaler Ablesung, genannt CT D'OR (CT with Dual Optimum Reading). Mit dieser Geometrie sammelt man die Radon Daten, nachdem der Röntgenfächer durch eine Maske kollimiert worden ist. Diese Eigenschaft ermöglicht eine effiziente Datensammlung und verringert möglicherweise die Patientendosis. Durch eine Monte Carlo Simulation wird gezeigt, dass man mit CT D'OR Bilder gleichwertiger Qualität wie mit normaler CT-Aufnahmetechnik bekommen kann. Desweiterem wird mit einem in dieser Arbeit entwickelten Demonstrationsgerät gezeigt, dass die Scangeometrie CT D'OR Daten für zwei unabhängige, sich gegenseitig ergänzende Rekonstruktionen sammelt.

Zunächst wird die Motivation für diese Arbeit beschrieben: CT Untersuchungen generieren einen hohen Anteil der medizinischen Strahlenexposition der Bevölkerung in Industrieländern. Der gegenwärtige Stand von CT-Systemen und möglichen Theorien zu den Effekten geringer Strahlenexposition werden dargestellt. Im Anschluß werden die theoretischen Grundlagen der Scangeometrie CT D'OR und des Rekonstruktionsalgorithmus OPED (Orthogonal Polynomial Expansion on Disc), die in der Arbeit benutzt werden, erklärt.

Der Algorithmus und die Scanngeometrie werden durch Simulationstudien untersucht: Interpolationsfunktionen werden eingeführt, die manchmal im Rahmen von OPED und CT D'OR nötig werden. Durch eine Monte Carlo Simulation werden Vergleiche mit konventionellen CT-Technologien vorgestellt.

Die Entwicklung des im Rahmen dieser Arbeit entstandenen Demonstrationsgeräts, die benutzten Versuchsobjekte und der Aufbau der Experimente werden beschrieben. Die erforderliche Verarbeitung der aufgenommenen Daten, die man vor der Rekonstruktion durchführen muss, wird dann ausführlich erläutert. Die Rekonstruktionen bestätigen bestimmte Eigenschaften von OPED und CT D'OR und lassen den Schluß zu, dass das Konzept von CT D'OR funktioniert. Die Bildqualität der Rekonstruktionen wird kommentiert, und eine kritische Auseinandersetzung mit Nachteilen unseres Demonstrators inklusive Verbesserungsvorschläge wird geführt.

Dadurch könnte ein zukünftiger Prototyp von CT D'OR möglicherweise die Röntgendosis des Patienten bei gleicher oder besserer Bildqualität verringern. Das könnte im Endeffekt dazu beitragen, die durch die medizinische Bildgebung steigende Strahlenexposition der Bevölkerung in Industrieländern zu reduzieren.

Chapter 1

Introduction

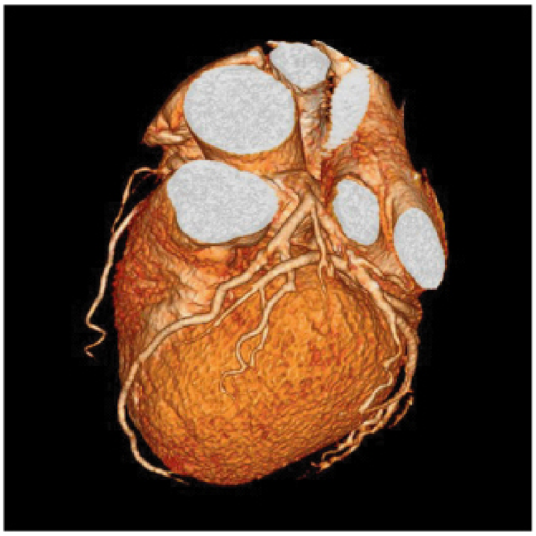

Figure 1.1: A visualized cardiac-CT.

Computed Tomography (CT) has become an indispensable tool for medical diagnosis because of its extraordinary properties for imaging: CT-scanners are able to produce images of anatomical structures with sub-millimeter resolution (figure 1.1), and they can even dynamically observe the heart beat in real-time[1].

Nevertheless, the radiation exposure related to these examinations together with their increasing use, has already caused concern at the International Commission on Radiological Protection [ICRP 07] and has recently reached the media of industrialized countries[2], especially after the publication of a recent article [Brenner 07] focusing on the potential health effects of CT-studies.

The motivation for this work was therefore to develop a new CT-device that can use less X-ray dose to obtain the same or better image quality. The theoretical dose reduction achievable at an equivalent image quality was to be assessed with a Monte Carlo simulation. A simplified test-device was to be designed and constructed to check if the new geometry of data acquisition can produce the expected reconstructions. Additionally, a new reconstruction algorithm that also shows advantages against conventional algorithms was to be used.

This introduction starts with a brief description of the historical development of CT devices (section 1.1). Afterwards, the basics of current CT-technology are presented in section 1.2, including some of its intrinsic problems, which can be partially solved using the new ideas presented in the rest of this work. Section 1.3 contains a comparison of CT-dose to the dose due to other medical imaging modalities and due to other radiation sources. Finally, a very brief discussion on the concern about the potential health effects of low-dose radiation is included in section 1.4.

---

[1] See video in [Berenson 08].

[2] See examples of articles in newspapers of Germany [Rögener 07], USA [Rabin 07a; Berenson 08; Press 07], Spain [Rabin 07b] and the UK [Boseley 07].

1.1 Milestones of Computed Tomography

The first generation of CT-scanners for clinical application was developed during the 1960's and the 1970's[3] by many small contributions [Kalender 06], among which were the pysicist's Cormack [Cormack 63] and the engineer's Hounsfield [Hounsfield 73]. Both received the Nobel Prize in Medicine in 1979 for their work, which used ideas from the early works by H A Lorentz [Cormack 92] and J H Radon [Radon 17]. This first generation used the so-called pencil-beam to obtain the data; one source irradiated one detector element at the opposite side of the patient. The problem of this technique is the very long scan-time (about one hour for one slice), since the whole assemble had to be stopped after each translation in order to reorientate the object. A partial solution came with the second generation in 1972 [Brooks 76], where several detector elements in a row were irradiated by a narrow fan beam. This allowed for the collection of several projections during one translation; one slice could be scanned in 10 to 20 seconds.

The use of a wide fan gave birth to the third generation of scanners in 1976 [Brooks 76]; the source and the detectors conform a single unit that continuously rotates around the patient. This allows for the scan of a slice in less than one second. The main problem of this generation was, at first, that the gantry had to be rotated consecutively in opposite directions to avoid the entanglement of the cables. This problem was solved using the so called slip rings, which gave birth to spiral-CT [Kalender 90]. This generation has been lately improved by larger detectors that have more than one row of elements; multi-detector CT are currently the most common devices world-wide [Kachelrieß 00].

Further advanced prototypes for Computed Tomography like the fourth or the fifth generation, have not been successfully commercialized because the improvements they provided were not worth the higher price of constructing them (see [Hsieh 03], pp. 12-16).

Currently developing ideas are Cone-Beam CT with one or two flat panel detectors ([ICRP 07], §18), and "Dual Source CT" [Flohr 06], which includes an additional source-detector sytem rotating 90° after the first one. At an early stage of developement is Inverse Geometry CT [Schmidt 04; Silver 05].

1.2 Current systems for Computed Tomography

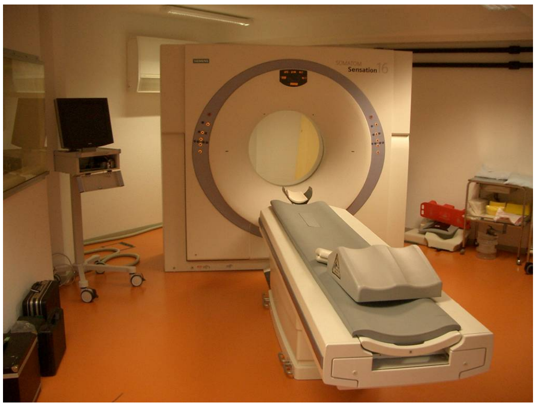

Figure 1.2: A typical CT scanner.

The external appearance of a typical CT scanner is shown in figure 1.2: the gantry has an internal diameter of 82 cm to permit patients being moved through it [NHS 05]. Inside, there is an X-ray source and a detector in the shape of an arc. Both rotate together around the patient, acquiring data that can be reconstructed to form 3-D images like the one shown in figure 1.1. However, for practical reasons, in this work we will concentrate on 2-D scans of one single slice of data. How typical CT-devices acquire the data for one such slice is explained in section 1.2.1. Intrinsic problems of the current technology are described in section 1.2.2. We want to overcome these drawbacks with the device developed and tested in this work.

---

[3] Earlier attempts for radiological tomography in the first half of the XX$^{\text{th}}$ century are described in detail in [Webb 90].

1.2.1 Data acquisition in a CT-scanner

The acquisition of data during a CT-scan is exemplified in figure 1.3; each position of the source provides a projection or "view" of data in the detector or "arc". Each one of these views contains information about the absorption properties of the scanned object. The data collected in each view are collocated after each other as columns of a matrix, which is called "fan-data", because the rays from the source take the form of a fan.

Nevertheless, most algorithms for reconstruction of the CT-data into a radiological image require the data to be collected in projections of parallel rays, not of rays in the shape of a fan. Therefore, the matrix of fan-data must be transformed into a matrix of parallel data (this process will be treated in detail in section 4.1). This final matrix of parallel data is called "sinogram" because the curve generated in this matrix takes a sinusoidal form if you scan a single point (see [Kak 88], pp.92,94 or [Hsieh 03], pp 43-46).

Current CT-scanners acquire about 4000 views distributed over 360°, and the arc contains typically 1000 detectors, that is, CT-scans collect 1000 rays per view. Therefore, the fan-data matrices have a typical size of 4000 x 1000 pixels. Such a matrix for a single slice of thickness 0.5 to 1 mm can be acquired in 0.33 s, thus data for whole organs or the whole body can be acquired in 5 to 20 s with a spatial resolution of 12 to 25 line-pairs cm^{-1} [Kalender 06].

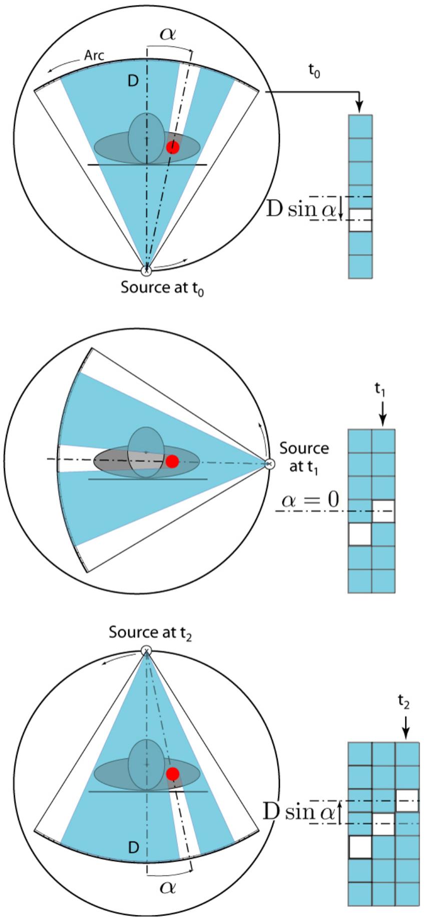

Figure 1.3: **From top to bottom, three successive projections or "views" over** 180°, generating a fan-data matrix of three columns. Note that the shade caused by the X-ray absorption of the red point generates a curve in the matrix.

1.2.2 Intrinsic drawbacks of current CT-scanners

Some technical precautions that can be taken with current devices for CT are being currently studied and discussed, along with practical solutions to make a better use of them and make the best out of the radiation the patient is exposed to. See for example chapter 3 of the report [ICRP 07], and more recently [Theocharopoulos 07] or the European Project [EUCT 07]. The problems we want to discuss here are, however, of another kind. They are intrinsic, unavoidable problems of current CT-scanners. They are schematically depicted in figure 1.4 and enumerated in the following:

a. Scattered radiation generates additional noise in the images.

b. The large weight of the latest commercial models of CT devices limits the rotational speed of the gantry, thus organ movement artefacts cannot be reduced further [Hsieh 03].

c. The data interpreted as a straight ray by the reconstruction algorithms are collected in a region that has a non-straight form. This shape (very strongly exaggerated in figure 1.4 c.) is generated by all trajectories travelling from the source to a detector during the time that this detector acquires a single reading. This effect introduces inhomogeneity in the resolution of current devices.

d. In order to acquire the data for a slice (a so-called "half scan"), it is necessary to irradiate the patient during a minimum gantry rotation of 180° plus the fan angle, because the slice-data would otherwise be incomplete (see [Kalender 05], p. 63).

e. The parallel data arrangement, which are computationally more efficient and stable (represented in figure 1.4 e. by black dots) do not correspond to the fan-data acquired in the scanners (white dots) [Hsieh 03], pp. 76-8. Therefore, an interpolation process called "rebinning" is usually necessary before carrying out the reconstruction [Kalender 05], pp. 255-6. This interpolation from fan-beam to parallel-beam geometry is often not appropriate, especially for a wide fan, because the density of rays is different in the centre of the field of view from the density in the outskirts. However, the rebinning interpolation kernels do not take this into account (they use constant support) [Tischenko 08].

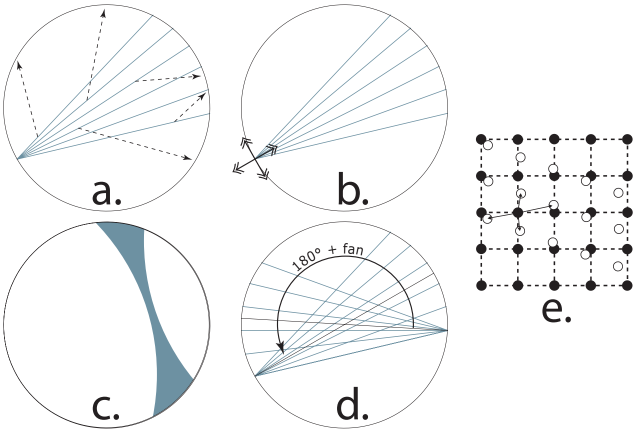

Figure 1.4: **Intrinsic problems of current CT-devices** (see text above).

1.3 Collective dose from Computed Tomography

The dose from CT-scanners represents the largest contribution to the radiation burden from artificial sources of an average German, even though it only represents 7 % of the medical examinations using X-rays (figure 1.5). In other industrialized countries like the USA and Japan, the contribution from CT-scanners to the overall dose is even larger [Brix 05].

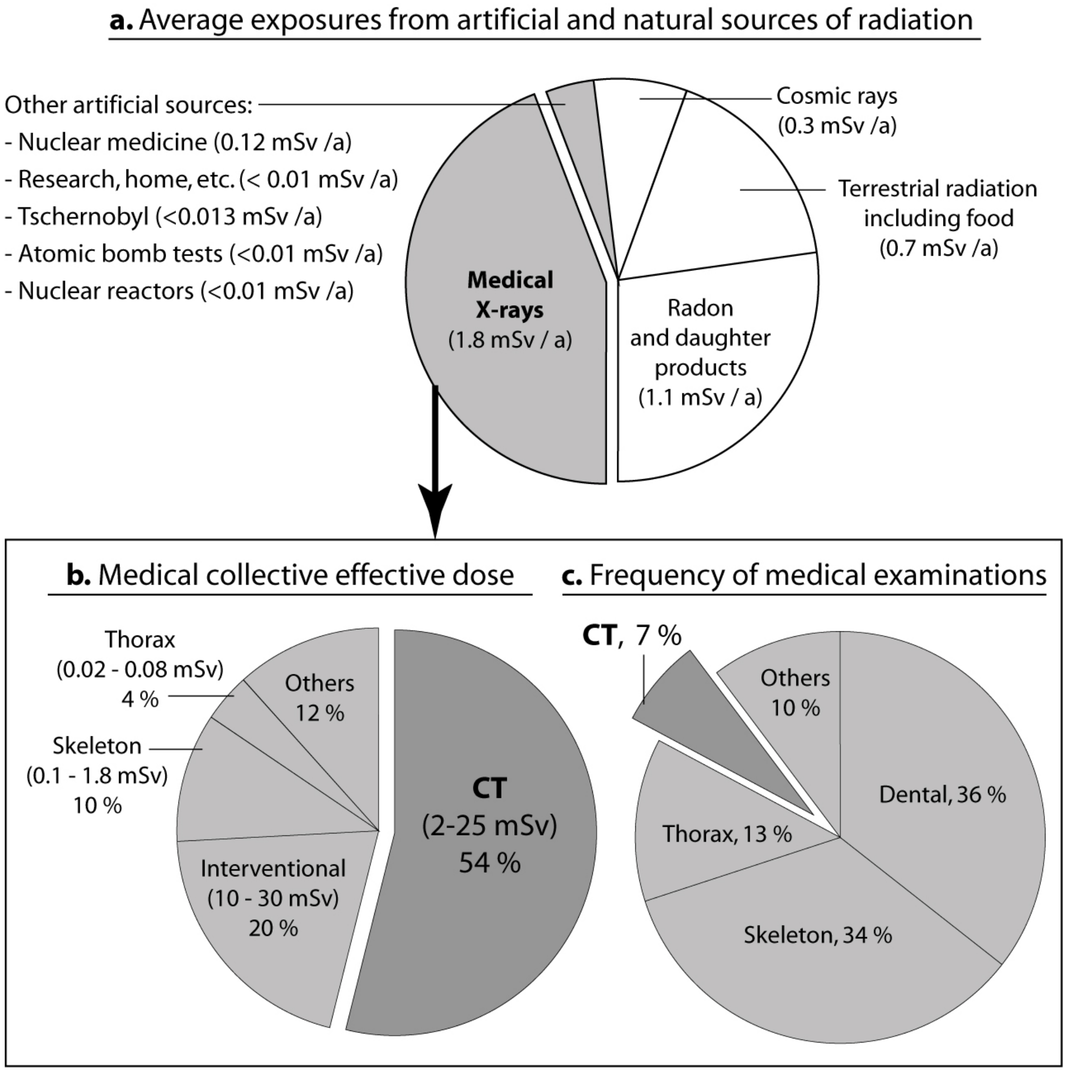

Figure 1.5: **Statistics on radiation exposure of an average citizen in Germany**; **a.** Percental contribution of each source of radiation in 2006 (average annual dose values are shown in brackets). **b.** Contribution of each X-ray modality to the collective effective dose from medical X-rays in 2004 (the dose range per individual examination is additionally shown in brackets). CT-examinations can be divided into cranial CT (2 - 4 mSv), spine (2 - 11 mSv), thorax (6 - 10 mSv) and abdomen (10 - 25 mSv). **c.** Contribution of each X-ray examination to the total amount of X-ray examinations in Germany in 2004. All data were taken from [BMU 06].

Furthermore, the use of CT scanning has increased by more than 800 % globally in the last two decades [ICRP 07]. The evolution since 1996 of the corresponding mean effective doses to the population can be observed in figure 1.6.

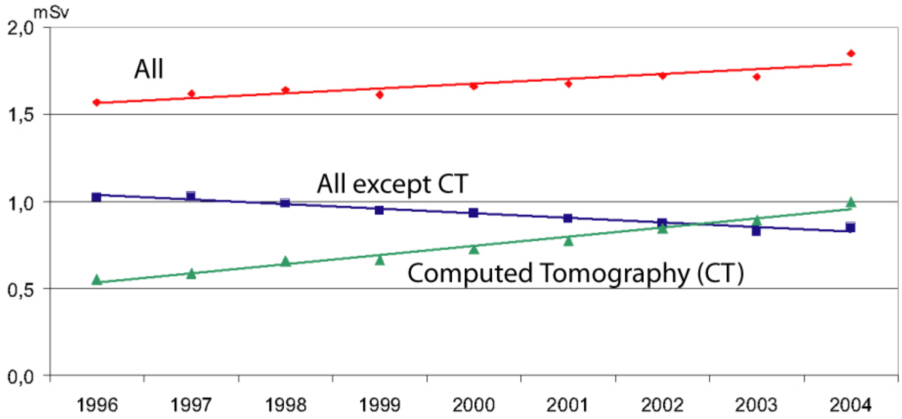

Figure 1.6: Temporal evolution of the dose from medical X-ray examinations to an average citizen in Germany [BfS 08b].

An explanation for this trend may be the lack of information discovered in the study [Lee 04], where it was found that “Only half of the radiologists and almost none of the patients or emergency-department physicians believed CT examinations might increase a patient’s risk for cancer”[4].

As a result, the International Commission for Radiation Protection has recommended that “dose reduction should remain a high priority for manufacturers” [ICRP 07]. Furthermore, the campaign “Image Gently” [Goske 08], motivated by the recent articles [Brenner 07; Hall 08], has been launched to make physicians conscious of precautions to be taken when imaging children.

---

[4] As cited in [Voress 07] by the student Matthew Voress of Toledo (Ohio), whose very informative and greatly structured article was very useful in preparation of this part of the introduction.

1.4 Concern about health effects of low-dose radiation

The effects of ionizing radiation are classified into two groups:

1. **Deterministic effects** appear in a dose-dependent manner of severity after the application of radiation above a given threshold. The higher the amount of the irradiation above this threshold, the greater is the effect. For teratogenic effects (malformations) in the embryo, for example, the local radiation of the mother must be above 100 mSv [BfS 08a]. Symptoms of sickness appear above 1 Gy. Cataracts are estimated to appear at a threshold of 2 Gy after an acute irradiation, or 5 Gy in fractionated doses [Voress 07][5]. Other effects are erythema, impairment of the central nervous system and desquamation, which appear between 0.5 and 5 Gy. Death of an adult can happen after an acute whole-body irradiation of 4 Gy [BfS 08a].
2. **Stochastic effects** are based on probability; a low dose might cause a detectable damage, but it is also possible that a higher dose may have no final effect in the exposed person. The most typical stochastic effect is the development of leukemia and other cancers. In this case, it is the probability of an advanced health effect that increases with the received dose, but not its severity. These effects are studied mostly by observations among the survivors of the atomic bombs of Hiroshima and Nagasaki; most excess cancers have been observed only above an exposition of 100 to 500 mSv.

There is no agreement yet about the effects of low-dose radiation. The International Commission on Radiological Protection, as well as the American Association of Physicists in Medicine, recommend that patient doses need to be kept as low as reasonably achievable (ALARA principle) [ICRP 07; AAPM 08], but some theories defend that low doses might even decrease the risk of developing cancer (see figure 1.7) through the activation of an adaptive response that may protect against radiation effects ("hormesis", [Feinendegen 05]). However, "the general scientific consensus is currently in favour of the so-called linear no threshold (LNT) model as the most appropriate dose-response relationship for radiation protection purposes at low doses" [Wall 06].

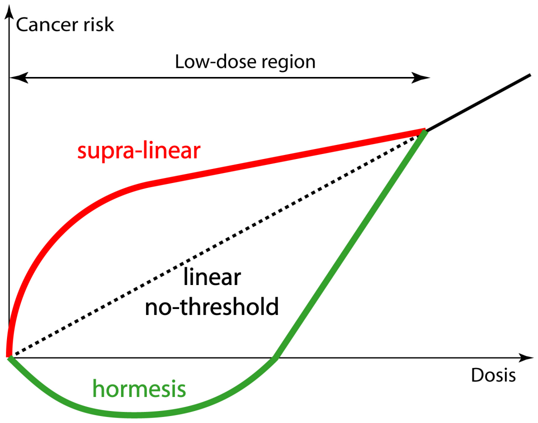

Figure 1.7: **Theories for the effects of low-dose radiation**. Note that the theory of hormesis defends a favourable effect in tissues receiving low-dose ionizing radiation.

---

[5] New studies among the Chernobyl survivors tend to show that cataracts may form even after doses of less than 1 Gy [Worgul 07].

Chapter 2

Theoretical Background

This chapter contains the explanations of the concepts used in the rest of this work (many assertions of this chapter will be verified with examples in chapters 6 and 7).

Section 2.1 presents the concept for a new scanning geometry called CT D'OR (CT with Dual Optimum Reading), patented before this work was started [Tischenko 07]. Section 2.2 presents the algorithm OPED (Orthogonal Polynomial Expansion on Disc) for reconstruction of tomographic data, whose geometry is ideally represented by the data geometry for CT D'OR [Xu 06a; Tischenko 06]. Both tools are especially suitable to work together , but they can also be used independently with conventional technologies. The tools used and developed in this work to assess image quality are briefly introduced in section 2.3.

2.1 A new scanning geometry

The new scanning geometry for which a test-device was developed in this thesis[1], is called CT D'OR (CT with Double Optimum Reading), because it acquires two sets of complementary data using an optimum geometry. The concept of CT D'OR was presented at the Conference SPIE Medical Imaging in 2006 [Tischenko 06].

In section 2.1.1, the general idea of CT D'OR is presented, including how it, in principle, solves or reduces the problems described in chapter 1. Section 2.1.2 describes in detail the acquisition of the two independent and complementary sets of tomographic data. Section 2.1.3 explains the differences between the ideal geometry and the actual device that was constructed for this work.

2.1.1 Description of the concept

The main idea[2] is based on collimating the X-ray beam through a circular mask of detectors that are shielded on the side of the X-ray source (see figure 2.1). Since the space between detectors has the same size as the shieldings, the amount of rays passing through the patient in a whole rotation of the source is just one half of the radiation that he would receive if the mask were not there. At the same time, two independent sets of data, allowing independent reconstructions, are acquired with this new geometry: one with the mask-detectors, and another one with the arc-detector of the gantry (in the following, arc). These two sets of data are complementary, hence the name of CT with Dual Optimal Reading or CT D'OR.

---

[1] All papers, posters, talks and awards related to this subject can be found in the attached CD.

[2] For a visual, animated description of CT D'OR please see the file `Data_Acquisition.ppt` in the CD.

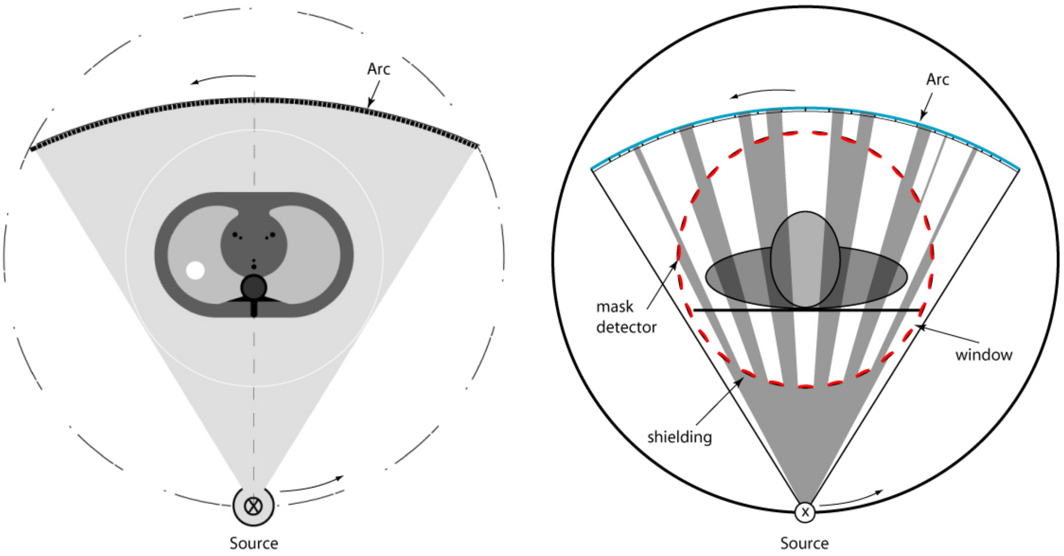

Figure 2.1: **A conventional 3^{rd}-generation CT (left) in comparison to the concept of CT D'OR (CT with Dual Optimal Reading, right)**. In CT D'OR, the X-rays are collimated through the windows and are received by either the mask detectors or by corresponding detector regions or "bins" of the arc detector.

The shieldings and the detectors serve to collimate the rays, Thus the following advantages reduce the problems of current technologies described in figure 1.4.

a. A direct correction for scattered radiation: during the time that the detectors are shielded against direct radiation, they receive only scattered radiation. The readings in these moments can be used to estimate the scattered radiation received during the measurements of direct radiation [Schlattl 08; Schlattl 06].

b. Stability of the measurements against slight movements of the gantry due to centrifugal forces: due to the collimation, the trajectory of a photon will always be part of a correct ray (grey stripes in figure 2.1), no matter where exactly the photon comes from.

c. Data acquisition over perfectly straight stripes, marked in grey in figure 2.2: the density of photon-trajectories traversing the stripe has a similar form to the one shown in figure 1.4 c., but in the case of CT D'OR, those trajectories certainly fill out a straight region.

d. The geometry of data collection with CT D'OR in a 360°-turn is equivalent to parallel data over 180°. The patient exposition during the additional fan-angle turn of the source is not necessary.

e. The acquisition of parallel data directly: This device acquires the data that are optimal for OPED [Xu 06a] (section 2.2), but it can also be used with other reconstruction algorithms. This feature will be shown in detail in section 2.1.2.

A difference of CT D'OR against a 4^{th}-generation CT-scanner, is that the mask may be added as a static inner ring inside the gantry, without the need of major changes in the current technology of a conventional CT-scanner, because the gantry and source designs can be kept unchanged.

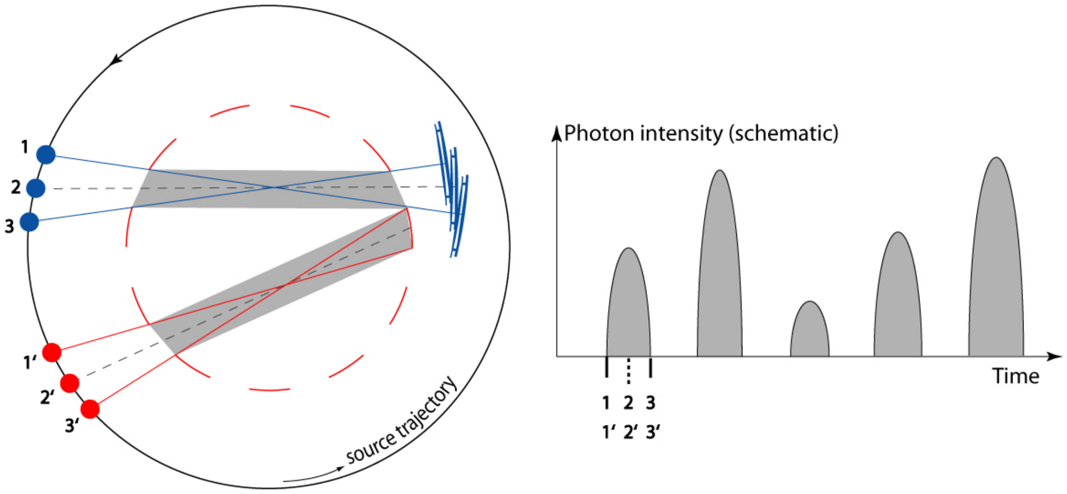

Figure 2.2: **Data acquisition in CT D'OR (ideal case).** Every detector is recurrently exposed to radiation (during the source positions 1 to 3 or 1' to 3') and shielded. Therefore, each one of the pieces of data or "rays", represented by a grey stripe, are acquired in the form of peaks in both the mask and the arc detectors, as schematically shown on the right.

2.1.2 The two kinds of Radon Data

The input data for a reconstruction algorithm are named "Radon data" in honour of the bohemian mathematician J. H. Radon[3] (see equation 2.5 in next section). The scanning geometry CT D'OR allows for the acquisition of two independent, but complementary sets of Radon data. Each one produces a single self-contained sinogram and a corresponding reconstruction. However, both sets of data must be rearranged into one more detailed sinogram that allows for a final reconstruction with twice as much resolution. The structure of the single sets of data is depicted in figure 2.3. It is best understood with the animations included in the file `Data_Acquisition.ppt` in the CD, but it will also be described in the following, along with the process of data-rearrangement.

Data from the mask detectors

Think of one single detector of the mask and imagine the source rotating 360° around the mask and irradiating the detector through all collimator slits of the ring. If the trajectories of all those photons are painted in grey, they group in rays that take the form of an inversed fan[4], as shown on the left of figure 2.3.

Data from the arc detectors

Think of one small portion of the arc (called "bin") and imagine the source rotating 360° around the mask and irradiating that single bin. All photons received must have travelled through two windows before reaching that bin. If one paints in grey the trajectories of all those photons, one sees that they group in rays with the structure shown on the right of figure 2.3. In this case one does not obtain a direct fan, but rays at a certain distance off the center in all possible directions. Each one of those rays belongs to a different fan or "view". For example, for the central bin of the arc, all rays pass very close to the centre of the ring.

---

[3] The noble gas Radon took its name just as a variation of the radiactive element Radium.

[4] "Inversed fan" because there is a detector at the intersection of the rays, instead of the X-ray source.

Each ray from window to window is acquired twice: once in one direction, and once more in the opposite direction (in a different bin). Hence the amount of different data is only one half of the data obtained with the mask detectors, and therefore the resolution will be lower. Nevertheless, these data will also have a lower level of noise, because the two equal measurements can be averaged into a single one.

The virtual rays from one mask-detector to all other mask-detectors also form part of this same geometry, but they cannot be acquired because the photons are absorbed in the shielding elements. Therefore, these data (25 % of the total data acquired with CT D'OR) must be obtained through appropriate interpolation within the sinogram.

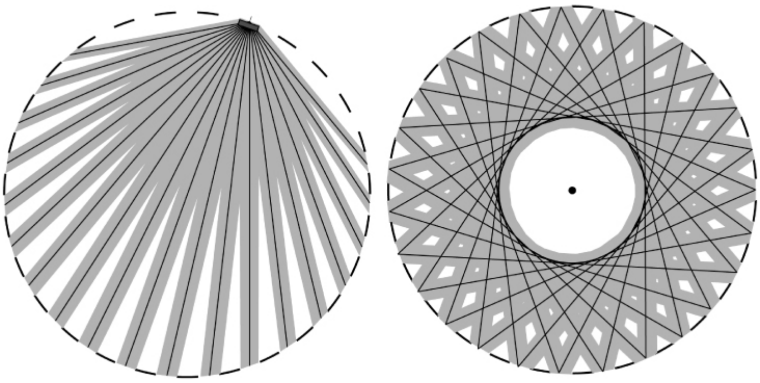

Figure 2.3: The schema of the data acquired by one single detector of the mask (left) and one bin of the arc (right) after the source has rotated 360° around the mask. Each ray is shown as a grey stripe, which is made up of all trajectories followed by photons reaching the given mask-detector or arc-bin.

Rearrangement of both data sets

If one represents each ray by its central line only and draws 3 neighbour-views of each kind together, one obtains the diagram shown in figure 2.4.

The two sets of measured data can be arranged in a larger matrix of fan-data, containing all rays from any window to all other windows and detectors. This matrix also contains empty cells corresponding to the virtual rays from one mask-detector to all other mask detectors. The total number of rays is thus 2N x (2N-1), where N is the number of detectors in the ring.

We can reorder this matrix into a parallel geometry where the projections are distributed over π. Interpolating the 1/4 of missing rays, introduced at the end of previous subsection ("data from the arc"), we obtain the full sinogram to be reconstructed. The final number of rays is then $2N$ [parallel views] $\times$ N [rays per view] $= 2N^2$.

2.1.3 The case of this work

The data acquisition schema in the case of the device built during this work is represented in figure 2.5. It is slightly different from the ideal case shown previously in figure 2.2, because the shielding elements and the windows do not have the same size. Furthermore, the effective surface of the detectors is smaller than the shieldings, as will be shown in detail in section

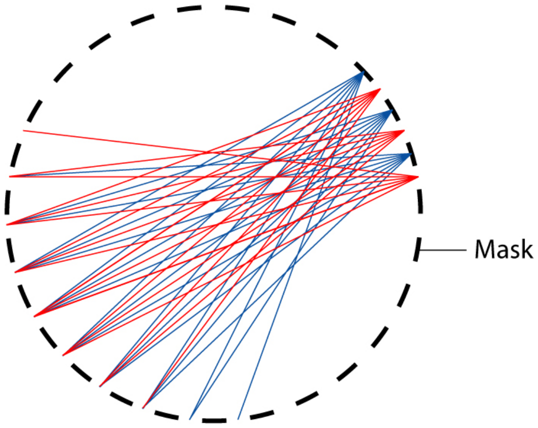

Figure 2.4: **Three views of each kind of measured data** (the rays are represented here by its central line only). The rays received in mask detectors are depicted in blue, and the ones received in the arc-detector are depicted in red. Observe that the fan-views of each kind are independent but complementary, and they are arranged in an alternating order.

5.1.1. These drawbacks are caused by the shape and the design of the mask-detectors we bought (which are presented in section 5.1.1 and 5.1.2 and discussed in section 9.2).

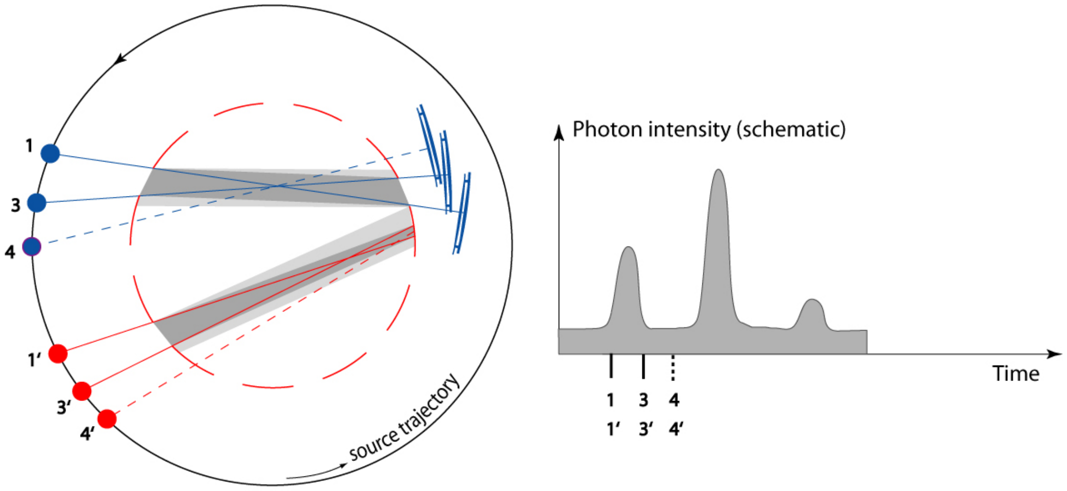

Figure 2.5: **Data acquisition when the windows are smaller than the shieldings**. Compare this figure to figure 2.2; The rays and the peaks obtained in the ideal case are still shown in light grey. The intermediate positions labelled 2 and 2' in figure 2.2 have been removed here for clarity. The new positions 4 and 4' indicate the moments where the detectors receive scattered radiation or radiation that has been partly absorbed in the shieldings.

Consequently, a device with shieldings of a larger size than the windows does not make use of all the potential of the idea, since some of the radiation passing through the patient is lost: all the blank space in figure 2.6 between any two parallel regions of the same colour (about 25 % of all surface) represents data that cannot be acquired with such a device. However, this effect is not a problem for the test of principle intended in this work.

In the case of the arc, the data related to the light-red portion between the two depicted red regions can obviously not be collected. Nevertheless, these regions form part of the data needed for the reconstruction, and must be thus obtained through interpolation within the acquired data.

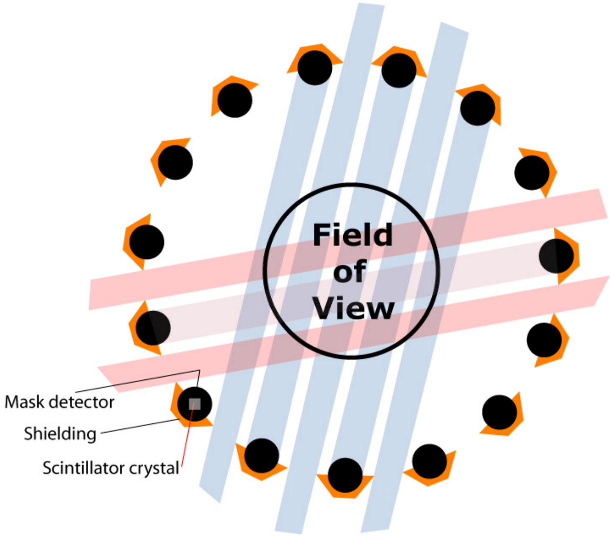

Figure 2.6: **The blank portions of potential data that are not acquired when windows are smaller than the shieldings**, as in the device developed in this work. The trajectories of photons traversing the Field of View and received in the mask are contained in the blue regions. The trajectories of photons received in the arc-detector are contained in the red regions. The light red region represents a ray that must be obtained through interpolation.

In the case of the mask-data, even more data are lost because the efficient thickness of the detectors (the thickness of the scintillator crystal) is only $\frac{1}{3}$ of their physical thickness (which was originally constructed of the same size as the windows). The photons detected in the mask detectors are therefore only

$$\frac{3}{4}[\text{passing through the windows}] \cdot \frac{1}{3}[\text{arriving at scintillator}] \rightarrow 25\%$$

of the photons that could be detected if the windows and the scintillators were of the same size. This problem is discussed in section 9.2.

In both kinds of data there are moments during which the detectors are only partly illuminated by the source (position 3 in figure 2.5). This half shade generates an extra dose in the scanned object because the data during that time are not useful for the reconstruction. Nevertheless, this half shade does not affect the results of this work. Only the photons received during full illumination of the detectors were used in the data treatment (see experimental data in figure 7.12).

2.2 The OPED reconstruction algorithm

Many algorithms have been proposed for the reconstruction of images from Radon data. Among them there are iterative reconstruction algorithms [Herman 76; Matej 96], analytical methods [Lakshminarayanan 75] and methods based on series expansions [Marr 74; Davison 81].

The most widely used algorithm in CT reconstruction is Filtered Back-Projection (FBP) [Shepp 74], mainly due to its relatively simple structure and its computational efficiency. Nevertheless, the FBP method requires additional operations like zero-padding in order to correct for the so-called "dishing" (or "cupping") and "dc" artefacts [Kak 88]. Furthermore, it uses a procedure called rebinning that converts fan data to parallel data; this procedure needs to overcome the inherent differences between the parallel beam geometry and fan beam geometry.

Recently a new algorithm for reconstruction of images from tomographic data has been proposed by Xu [Xu 06a; Xu 07]. The method, called OPED because it is based on **O**rthogonal **P**olynomial **E**xpansion on the **D**isc, has more recently been shown to be stable and accurate (see [Xu 06b]) and, moreover, it contains a clear advantage over the FBP method: the OPED algorithm is based on a geometry in which parallel rays are not equally spaced but follow the distribution of the zeros of Chebyshev polynomials of a given order. In some special cases discussed in chapter 4, such a geometry enables the conversion of fan beam data to parallel data by a simple relabeling, which means that the fan beam data can be used directly without rebinning.

In the following section 2.2.1, the relation of OPED to the scan-geometry of CT D'OR is explained. Then, a mathematical description of the algorithm is presented in sections 2.2.2 and 2.2.3 with a brief, more intuitive idea of it in section 2.2.4. At the end (section 2.2.5), a comparison of OPED with the algorithm FBP, introduced above, is given.

2.2.1 The relation to the scanning geometry

The algorithm requires parallel data from rays acquired at the precise positions mentioned above, and the geometry CT D'OR is able to acquire these parallel rays directly. This feature can be clearly appreciated in figure 2.7, and it is mathematically detailed in the following.

Data from the mask or "first-kind"-data

The fan-data from the mask-detectors can be directly reordered to a sinogram of parallel views. If there are N detectors in the mask, each parallel view contains N rays. These rays pass at a distance $R\,t_k$ off the centre, where R is the radius of the mask and

$$t_k = \cos\left(\frac{\pi(2k+1)}{2N}\right), k = 0, \dots, N-1, \tag{2.1}$$

are zeros of the Chebyshev polynomials of the first kind T_N of order N, defined as

$$T_N(t_k) := \cos\left[N \arccos(t_k)\right] = 0. \tag{2.2}$$

Thus the mask-data will also be called "first-kind data".

Data from the arc or "second-kind"-data

The fan-data from the arc can also be directly reordered to a sinogram of parallel views. If there are N detectors in the mask, each parallel view contains N-1 rays. In this case, these rays appear in the positions $R\,t'_k$, where R is the radius of the mask and

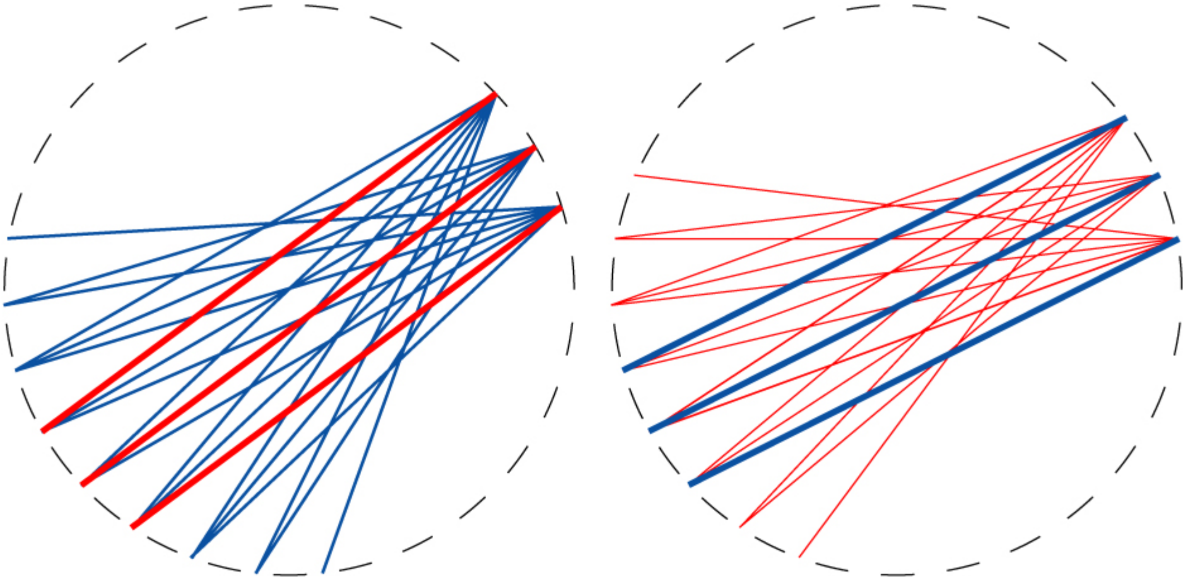

Figure 2.7: **Three fans of measured data (in the form of rays)** acquired by mask detectors (left) and by bins of the flat detector (right) after the source has rotated 40 degrees around this simplified mask of 27 detectors. Note that, in both cases, every ray of a fan is parallel to one ray of the other fans.

$$t'_k = \cos\left(\frac{\pi k}{N}\right), k = 1, \ldots, N-1, \tag{2.3}$$

are zeros of the Chebyshev Polynomials of the second kind U_{N-1} of order N-1, defined as

$$U_{N-1}(t'_k) = \frac{\sin N \arccos(t'_k)}{\sin \arccos(t'_k)} = 0. \tag{2.4}$$

The two geometries (mask and arc-rays) are illustrated in figure 2.8.

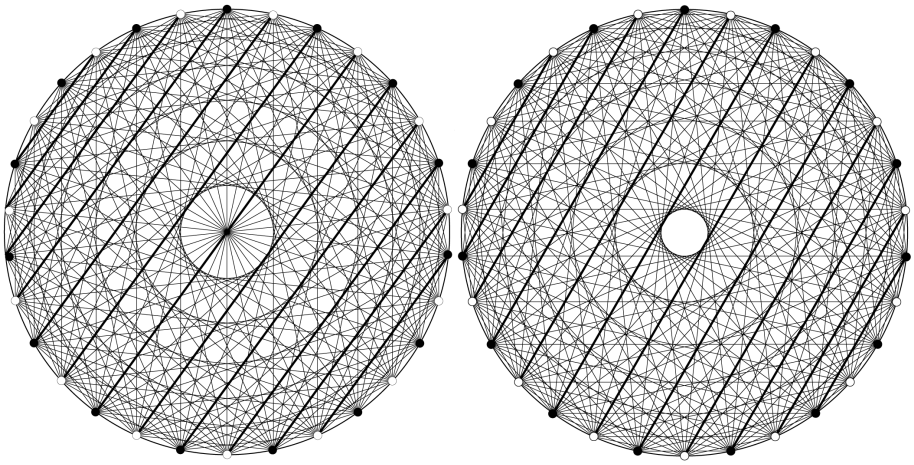

Figure 2.8: All rays in the geometry of the mask-data (left) and of the arc-data (right).

2.2.2 Mathematical introduction

The idea of the algorithm OPED is introduced in the following. It is based on treating the image that we want to reconstruct as a 2-D function that can be expanded in a certain basis of orthonormal polynomials. The coefficients of the expansion will be calculated using the radon data obtained in a CT-scanner [Xu 06a]. First, some definitions and propositions are necessary to describe the orthonormal basis, given in terms of the Chebyshev polynomials, in the Hilbert space $L^2(B_2)$ of square-integrable functions. Afterwards, we will use this property to justify the formula for the algorithm OPED.

Preliminaries

Let $B_2 = \{(x, y) : x^2 + y^2 \leq 1\}$ be the unit disc. Let f be a function

$$f : B_2 \to \mathbb{R}$$

such that

$$\int_{B_2} |f(x,y)|^2 \, dxdy < \infty \Longleftrightarrow f \in L^2(B_2).$$

1. The **Radon transform** of the function $f(t)$ is defined as

$$\mathfrak{R}_f(\varphi, t) = \int\limits_{B_2 \cap l(\varphi,t)} f(x,y) dxdy, \tag{2.5}$$

where

$$l(\varphi, t) := \{(x, y) \in \mathbb{R}^2,\ x\cos\varphi + y\sin\varphi = t\}.$$

That is, for a given angle φ and a given distance t (defined in figure 2.9), $\mathfrak{R}_f(\varphi, t)$ is a projection of the function f along the line $l(\varphi, t)$.

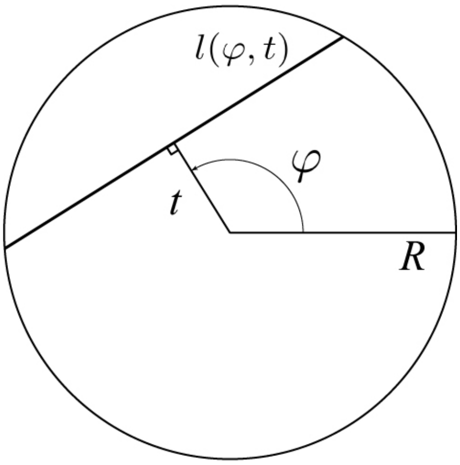

Figure 2.9: Ray geometry.

2. The **Ridge function** corresponding to the univariate function $f(t)$ is defined as

$$f(x,y;\theta) = f(x\cos\theta + y\sin\theta),$$

so that the bivariate function $f(x,y;\theta)$ is constant along its “ridges” $x\cos\theta + y\sin\theta = t$ at a fixed t. For simplicity of notation, we denote the **Ridge Chebyshev Polynomials** as

$$U_k(x\cos\theta + y\sin\theta) \equiv U_k(x,y;\theta).$$

3. The Chebyshev polynomials (of the second kind) generate an **orthogonal system with the weight** $\sqrt{1-t^2}$ on the interval $[-1,1]^5$, i.e.

$$\int\limits_{-1}^{1} U_m(t)\, U_n(t)\, \sqrt{1-t^2}\, dt = \int\limits_{0}^{\pi} \sin(m+1)\varphi\ \sin(n+1)\varphi\, d\varphi = \frac{\pi}{2}\delta_{m,n}.$$

4. The **Marr relation** [Marr 74], particularized to our case[6], expresses the Radon Transform of the Ridge polynomial $U_k(\cdot,\theta)$, and can be written as

$$\Re_{U_k(\cdot,\theta)}(\varphi,t) = 2\frac{\sqrt{1-t^2}}{k+1}U_k(t)U_k(\cos(\varphi-\theta))$$

5. The **view angle** θ is reduced to k positions $\theta_{k,j}$ equidistantly distributed in a circumference,

$$\theta_{k,j} = \frac{\pi j}{k+1}, \text{ where } 0 \le j \le k. \tag{2.6}$$

An orthonormal basis of polynomials in $L^2(B_2)$

With the help of the Marr relation, one can prove that

$$\frac{1}{\pi}\int_{B_2} U_k(x,y;\varphi)U_k(x,y;\theta)dxdy = \frac{1}{k+1}U_k(cos(\varphi-\theta)),$$

and using the corresponding view angles 2.6 one finds that

$$\begin{aligned}\frac{1}{\pi}\int_{B_2} U_k(x,y;\theta_{k,j})U_k(x,y,\theta_{k,i})dxdy &= \frac{1}{k+1}U_k(cos(\theta_{k,j}-\theta_{k,i}))\\ &= \frac{1}{k+1}\frac{\sin(j-i)\pi(k+1)}{\sin(j-i)\pi}\\ &= \delta_{j,i}.\end{aligned}$$

That is, the trigonometric polynomials $\{U_k(x,y;\theta_{k,j}), j = 0,\ldots,k\}$ are orthonormal. In order to show that they are also a basis in $L_2(B_2)$, we recall from Hilbert theory that all trigonometric polynomials generate a dense set of $L_2(B_2)$ [Dunkl 01]. That is, denoting with P_k the linear combination of $U_k(x,y;\theta_{k,j})$,

---

[5] See for example [Dunkl 01].

[6] Marr proved his relation for all orthogonal polynomials on the disc.

$$L_2(B_2) = \overline{\bigcup_{k=0}^{\infty} P_k}.$$

Hence, the set of polynomials

$$U_k(x, y; \theta_{k,j}) = U_k(x \cos\theta_{k,j} + y \sin\theta_{k,j}),\ 0 \le k \le \infty,\ 0 \le j \le k$$

generates an orthonormal basis in $L_2(B_2)$, as we wanted to show.

2.2.3 The reconstruction formula

According to the statement above, one can represent any function $f \in L_2(B_2)$ by its expansion on the basis of Chebyshev ridge polynomials as

$$f(x, y) = \sum_{k=0}^{\infty}\sum_{j=0}^{k} U_k(x, y; \theta_{k,j}) \underbrace{\frac{1}{\pi}\int\int_B f(x, y) U_k(x, y; \theta_{k,j}) dxdy}, \tag{2.7}$$

where the underbraced term represents the projection of the function over the corresponding basis vector $U_k(x, y; \theta_{k,j})$. The algorithm OPED serves to approximate the function f using its N Radon Projections $\mathfrak{R}_f(\varphi_\nu, t)$, obtained at the equidistant view angles

$$\varphi_\nu = \frac{2\pi}{N}\nu,\ \nu = 0, \ldots, N-1$$

with rays that are at a distance t off the centre of the field of view.

In order to obtain this practical formula, we start recalling Definition 2.5 and carrying out the change of variables $t = x\cos\theta_{k,j} + y \sin\theta_{k,j}$, thus obtaining the identity

$$\int\int_B f(x, y) U_k(x, y; \theta_{k,j}) dxdy = \int_{-1}^{1} \mathfrak{R}_f(\theta_{k,j}, t) U_k(t) dt. \tag{2.8}$$

This relation shows that the expression of f in basis of Chebyshev polynomials is related to expression of its Radon projections in the same basis. One can thus notice apparent similarity with the Fourier Slice Theorem in the framework of FBP.

Using 2.8, we can rewrite 2.7 into

$$f(x, y) = \sum_{k=0}^{\infty}\sum_{j=0}^{k} U_k(x, y; \theta_{k,j}) \frac{1}{\pi}\int_{-1}^{1} \mathfrak{R}_f(\theta_{k,j}, t) U_k(t) dt. \tag{2.9}$$

Then, we need to make use of the following two facts (proved in [Xu 06a]):

1. For any $0 \le k \le N-1$ and $0 \le \theta \le 2\pi$,

$$\frac{1}{N}\sum_{\nu=0}^{N-1} U_k(\cos(\theta - \varphi_\nu)) U_k(x, y; \varphi_\nu) = U_k(x, y; \theta). \tag{2.10}$$

2. For any k and $0 \leq \varphi \leq 2\pi$,

$$\sum_{j=0}^{k} U_k(\cos(\theta_{k,j} - \varphi))U_k(x, y; \theta_{k,j}) = (k+1)U_k(x, y; \varphi). \tag{2.11}$$

Truncating the summation over k to have N-1 terms, we obtain the final formula for the approximation $A_N f$ of f by its Radon Projections $\mathfrak{R}_f(\varphi_\nu, t)$,

$$A_N f(x, y) = \frac{1}{N} \sum_{\nu=0}^{N-1} \sum_{k=0}^{N-1} (k+1)U_k(x \cos\varphi_\nu + y \sin\varphi_\nu)\lambda_k(\varphi_\nu), \tag{2.12}$$

where the term

$$\lambda_k(\varphi_\nu) = \frac{1}{\pi} \int_{-1}^{1} \mathfrak{R}_f(\varphi_\nu, t)U_k(t)dt \tag{2.13}$$

can be approximated with a Gaussian quadrature that is exact for polynomials of order N [Xu 06a], thus obtaining

$$\lambda_k(\varphi_\nu) = \frac{1}{N} \sum_{j=0}^{N-1} \mathfrak{R}_f(\varphi_\nu, \cos\psi_j) \sin(k+1)\psi_j, \tag{2.14}$$

where $\cos\psi_j$ are zeros of the Chebyshev polynomials of the first or of the second kind.

Equations 2.12 and 2.14 form a direct formula to reconstruct the function f. For a comparison with the algorithm FBP, see section 2.2.5.

2.2.4 Intuitive explanation

The algorithm OPED consists of approximating the function $f(x, y)$ that we want to reconstruct as an expansion A_N in N Chebyshev Polynomials U_k of order k = 0,...,N-1. The formulae 2.12 and 2.14 of the previous section represent this expansion. If we write them together as

$$A_N f(x, y) = \underbrace{\frac{1}{N}}_{1} \sum_{\nu=0}^{N-1} \sum_{k=0}^{N-1} \underbrace{(k+1)}_{2} \underbrace{U_k(x \cos\varphi_\nu + y \sin\varphi_\nu)}_{3} \underbrace{\frac{1}{\pi} \int_{-1}^{1} \mathfrak{R}_f(\varphi_\nu, t)U_k(t)dt}_{4},$$

we realize that they contain the same terms as a conventional vectorial expansion:

1 is a normalization factor.

2 are reciprocals for the frequency. They are a weight for the corresponding components in the expansion.

3 is the corresponding basis vector, i.e. a Chebyshev ridge polynomial of the second kind.

4 is the corresponding coefficient of the expansion in those basis vectors, i.e. the scalar product of the Radon data (obtained with the CT-scanner) and the basis vectors. This integral is approximated with a Gaussian quadrature, as shown in equation 2.14.

2.2.5 Comparison of OPED to Filtered BackProjection

The main difference between OPED and Filtered BackProjection (FBP), the most often used algorithm for reconstruction, is that OPED needs no additional operations, such as filtering or zero-padding, and that OPED directly uses the data obtained in the CT-scanner, without any rebinning. This last difference is graphically explained in figure 2.10. The radon data needed by FBP are obtained by a special interpolation process within the measured data called "Rebinning" (upper graphs in figure 2.10). On the contrary, using OPED and the geometry CT D'OR, each radon data obtained in the scanner corresponds to a precise pixel in the sinogram, without Rebinning (lower graphs in figure 2.10). Nevertheless, OPED can also work with conventional geometries and CT D'OR can also work with conventional algorithms.

The artefacts produced typically by both algorithms OPED and FBP can be best observed close to large discontinuities, as in the profiles shown in figure 2.11. FBP suffers from the so-called "dishing" or "cupping" artefacts, whereas OPED suffers from the Gibbs effect[7].

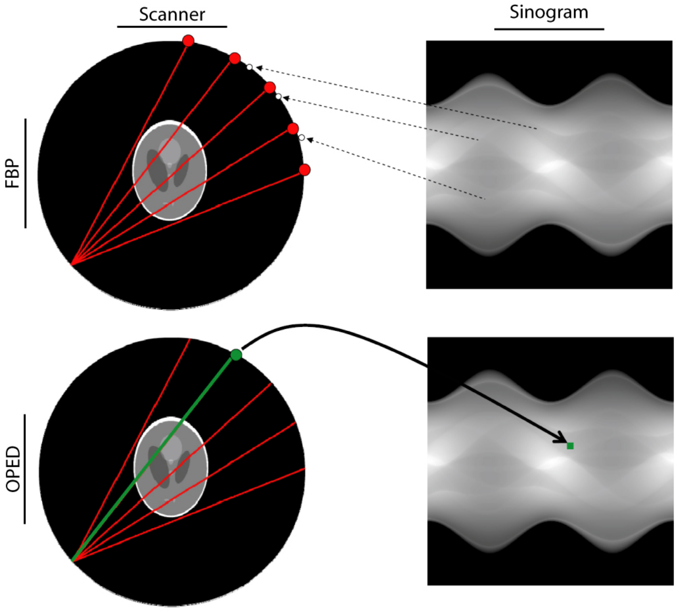

Figure 2.10: **Difference in obtaining data using FBP and OPED.**

---

[7] For a nice demonstration of the Gibbs phenomenon see [Trott 08].

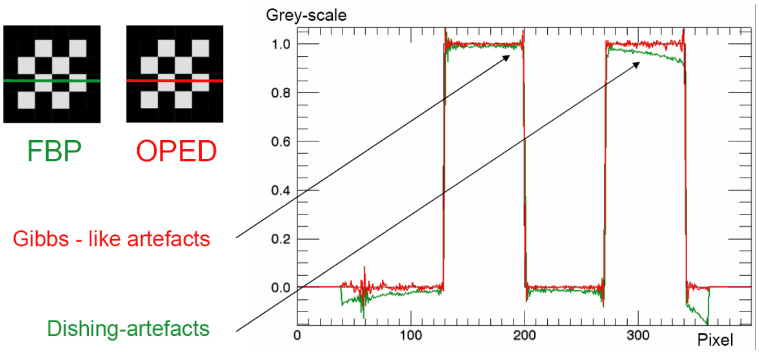

Figure 2.11: Profiles from chess board, reconstructed with OPED and FBP.

2.3 Image quality assessment

This section presents the measures used to quantify the image quality in this work, especially in chapter 4. We have used two properties for the analysis of image quality: reconstruction accuracy and spatial resolution.

2.3.1 Reconstruction accuracy

The reconstruction accuracy represents the difference between the original phantom and the obtained reconstruction. It is usually measured using the Normalized Mean Square Error (NMSE) [Barrett 04]. For a matrix R, representing the attenuation distribution in the reconstruction, and a matrix P, representing the attenuation distribution in the phantom, this measure is defined as

$$\mathrm{NMSE} = \frac{\|R - P\|}{\|P\|}, \tag{2.15}$$

where, for arbitrary matrices A and B,

$$\|A\|^2 = \langle A, A \rangle \qquad \mathit{and} \qquad \langle A, B \rangle = \sum_{i,j} (A_{ij} B_{ij}). \tag{2.16}$$

Another measure for the reconstruction accuracy is the Hilbert Angle (HA) [Wootters 81], defined as

$$\mathrm{HA} = \arccos \frac{\langle R, P \rangle}{\|R\| \|P\|}. \tag{2.17}$$

It also measures the deviation between the reconstruction and the original, but the HA has the advantage that it is invariant with respect to the grey-scale of the image.

The Mean Relative Error (MRE) has also been calculated for completeness. It is defined as

$$\mathrm{MRE} = \mathrm{mean} \left| \frac{R_{ij} - P_{ij}}{P_{ij}} \right|_{P_{ij} \neq 0}. \tag{2.18}$$

All previous measures are only sensible with reconstructions from simulated data, where the comparison with the original phantom is possible.

With both experimental and simulated data, we used the following standard deviation σ in homogeneous regions of the reconstruction as an estimate of the artifacts in the images,

$$\sigma = \sqrt{\frac{\sum \left(R_{ij} - \overline{R}\right)^2}{N-1}}, \tag{2.19}$$

where $\overline{R}$ stands for the mean of R in the chosen region and N is the amount of pixels in that region [Hsieh 03].

2.3.2 Spatial Resolution

The spatial resolution in the reconstructed images has been measured via the Modulation Transfer Function (MTF [Dainty 74]), following the Tilted Edge Method [Fujita 92] (see section 4.2) and an equivalent method using the Point Spread Function, described in the chapter of Materials and Methods in section 5.2.2. The MTF describes how much the imaging system reduces the amplitude of a sinusoidal entrance signal as a function of the frequency [Hoeschen 02]. In our case, the imaging system is the simulated scan with a limited number of projections and the reconstruction algorithm together.

Part I

Simulation studies

Chapter 3

Dosimetric radiation transport simulation

This chapter describes the Monte Carlo radiation transport simulations carried out to test the theoretical principles of the geometry CT D'OR (sections 3.1 and 3.2), and its ability to correct the scattered radiation (section 3.3).

3.1 Parameters of the simulation

To check the dose reduction potential of CT D'OR in principle, we simulated a set of fan-data as it would be acquired by a fan-geometry of equiangular rays. The code EGSnrc [Kawrakow 03] (Electron Gamma Shower, from the National Research Council of Canada) was used for the photon-transport calculations with the following parameters:

Distance Source-Detector: 50 cm

Distance Source-Axis: 25 cm

Fan Angle: 73.74° (Cone Angle: 0°)

Number of views: 394

Number of detectors: 393

Dimension of a mask- and arc- detector's pixel: 3.997mm x 5mm (height)
(This results in a circular bow of 180° around the source)

Number of photons: $5 \cdot 10^8$ per view

Diameter of the test object (see figure 3.1): 30cm

Spectrum: 120 kVp filtered with 1.2 mm Ti and 1.5 mm Al

A slice of the virtual phantom used in the simulations is shown on the top-left of figure 3.1. This phantom is a 30 cm-height cylinder with a diameter of 30 cm. It is filled with adipose tissue and contains a circle in the upper left that is filled half with air and half with lung tissue. In the right half, an ellipse filled with some soft tissue is embedded, which contains small circles of different sizes, filled alternately with water and slightly over-dense cartilage

($\rho = 1.2\ g/cm^3$). A small circle filled with original cartilage ($\rho = 1.1\ g/cm^3$) tissue can be found at the lower right. In the lower left region, the model contains three wedges, where the central one is composed of original cartilage and the others of mineral bone.

The simulated fan-data have 394 views and 393 rays per view and have been acquired with a fan-geometry (without mask). The corresponding sinogram can be ordinarily reconstructed by either OPED or the conventional algorithm FBP (Filtered BackProjection), by the latter after rebinning (as described in 4). On the other hand, this sinogram is the same that would be acquired with the geometry of CT D'OR, only with the following remarks:

- Using CT D'OR, one fourth of the data must be obtained through interpolation. In particular, the rays from one detector to another detector, which cannot be acquired in the device but form part of the geometry (see explanation in section 2.1.2).
- Using CT D'OR, the sinogram is obtained exposing the patient to 50 % of the radiation, because the shieldings and the windows of the ring have the same size (and the detectors and shieldings should have the same size too).

Therefore, we set the corresponding pixels in the fan-data to zero, interpolated the empty cells using cubic splines, and reordered the data to obtain a new sinogram, as it would be the sinogram obtained directly by CT D'OR. The intention of the simulation is therefore to show that this loss of 25 % of data does not imply a significant decrease in the quality of the reconstruction, whereas the dose reduction achieved is 50 % because the shields and the windows have the same size in this ideal simulation.

3.2 Results

The results from the simulation described in section 3.1 are shown in figure 3.1. The OPED reconstruction, smoothed with a low-pass filter, has the same quality as the FBP reconstruction, even though the program for OPED is not optimized yet. The reconstruction using the geometry of CT D'OR, where 25 % of the data have been obtained through interpolation, is shown on the right of figure 3.1. Observe that all reconstructions look alike, even in the pdf-file that can be found in the attached CD (the name of the pdf file is given in the beginning of the corresponding caption).

3.3 Correction for scattered radiation

This feature of CT D'OR has been analyzed in detail in [Schlattl 08] using the same Monte Carlo code that was used for the simulation introduced in section 3.1. A brief summary of that paper is presented here. Also the same phantom, of which a slice is shown at the top-left of figure 3.1, was used. A cone beam and 501 detector-window pairs were simulated, pursuing in total the history of 173 billion source photons. The results are summarized in figure 3.2.

A large amount of scatter radiation causes the so-called “cupping artefacts”, i.e. the reduced brightness in the center shown in figure 3.2 a. The scatter correction described in [Schlattl 08] produces ring-shaped artefacts (figure 3.2 b.) the cause of which might be understood after studying the influence of the object size and the preferred directions of scatter. Finally, figure 3.2 c. shows the corrected reconstruction in a more realistic case of a smaller amount of scatter radiation. Observe that it looks very similar to the middle reconstructions of figure 3.1, where no scatter radiation was taken into account.

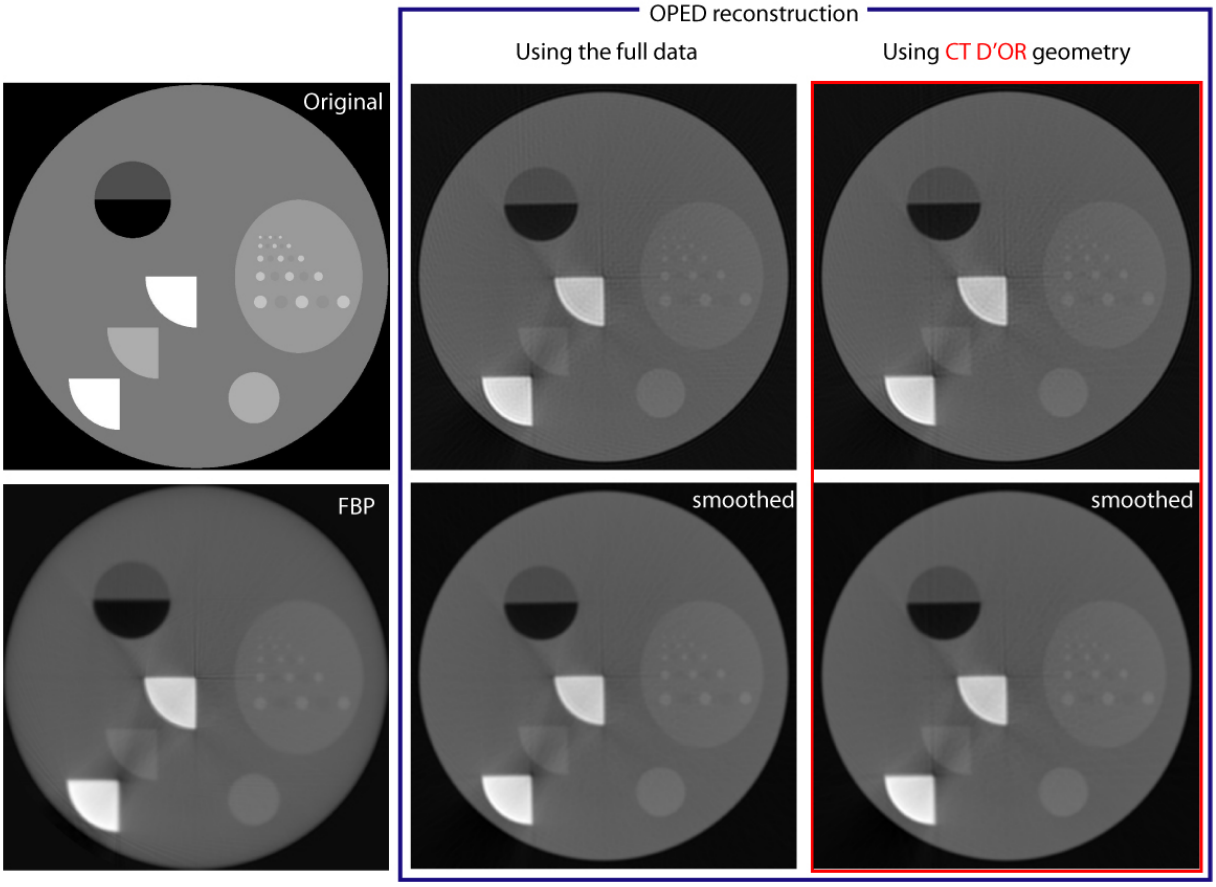
OPED reconstruction
Using the full data
Using CT D'OR geometry
Original
FBP
smoothed
smoothed

Figure 3.1: [`07-simulation.pdf`] **Results from the simulation described in section 3.1**. The original phantom is shown at the top-left. The reconstruction using FBP is shown directly below. The OPED reconstructions are shown inside the blue frame; the reconstruction using the CT D'OR geometry is shown on the right.

The correction for scattered radiation seems to be difficult to implement with the test-device developed in this work, because the amount of scatter radiation in the experimental data is not large enough. The radiation passing through the shieldings is higher, and therefore, during the time that the detector should theoretically receive only scatter radiation, it receives a high amount of direct radiation, which makes it difficult to distinguish the contribution from scattered photons. An example of this is shown in figure 3.3.

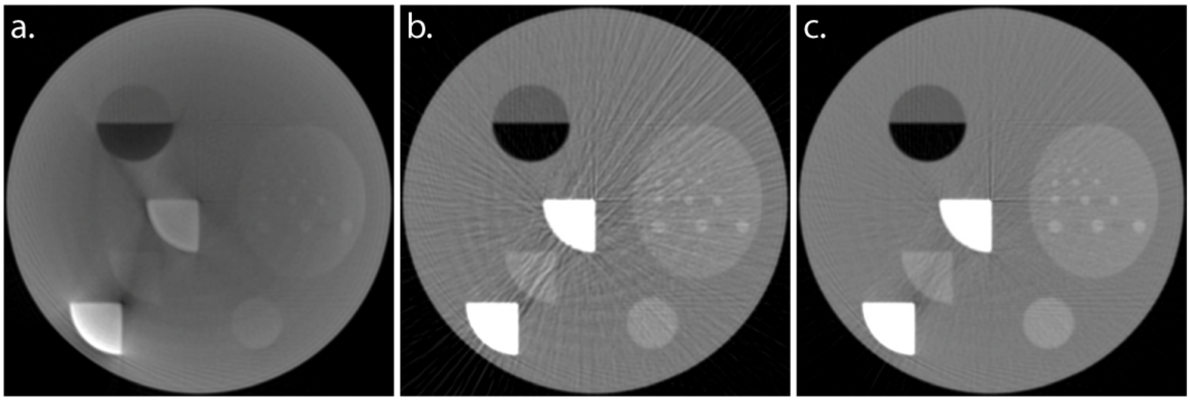

Figure 3.2: **Results from the simulated scatter correction** (taken from [Schlattl 08]). **a.** The reconstruction if the amount of scatter to primary rays ratio would be about 90 %, which is an exaggerated amount, so that the cupping artefacts can be well observed. **b.** The reconstruction after applying the scatter correction described in [Schlattl 08] to the data from **a.** and smoothing the result. **c.** The reconstruction after applying the correction to more realistic data, where the total scatter has been assumed to be 70 % less than in **a.**, and smoothing the result.

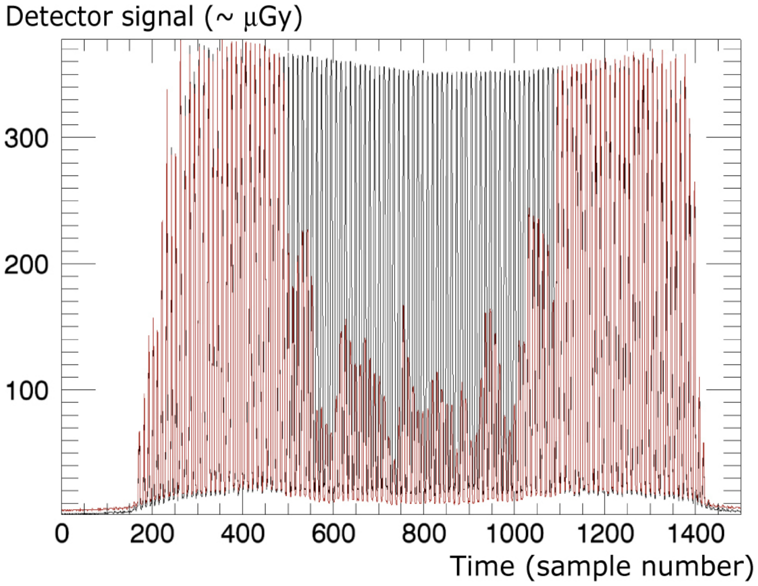

Figure 3.3: Detector signal at one detector over time during a phantom scan (red) and an empty scan (black) of the same region of the test-device developed in this work.

Chapter 4

Sinogram interpolation

The reconstruction methods with orthogonal polynomials like OPED have been always meant to need a strict geometry such as an equal number of views as rays per view, for example. We want to show that those methods, and OPED in particular, are in fact stable under variations of this condition. These variations are intended to make use of the full potential of OPED and improve the resolution of the resulting images. If we increase the number of rays inside a given fan without increasing the number of fan views, in the sinogram appear empty cells, which must be filled in by using interpolation between the measured data.

The need for this interpolation process is described in detail in section 4.1. Afterwards, the analytical phantoms used in the study are presented in section 4.2. 1-D interpolation alternatives are described in section 4.3, including the implicit drawback of these methods, which has motivated the search for appropriate 2-D interpolation alternatives, described in section 4.4. Our study concentrates on OPED, but the results may apply to any matrix when a large computational expense can become a problem; for example using the geometry of CT D'OR, as will be described in section 6.2 of chapter "data treatment".

4.1 The need for interpolation

For this discussion it is convenient to introduce a matrix representation of the Radon data. Fan beam representation and parallel beam representation (sinograms) are used most extensively for this purpose. In the fan beam representation, the k-th column of the matrix corresponds to the Radon data over the rays from the k-th source position or "view". On the parallel beam representation, the i-th column contains the Radon data over one parallel group of rays, which is characterized by a fixed view parameter ϕ_i. Within the latter representation, the j-th row contains the Radon data over the chords or rays which are tangent to the circle of radius t_j. If t_j are the zeros of the Chebyshev polynomial $T_N(t)$, where N is the number of views, then the sinogram will be referred to as a Chebyshev sinogram.

Since the number of views in the original OPED geometry is the same as the number of rays per fan view, say N, the fan beam matrix can be reordered straightforwardly into a Chebyshev sinogram and vice versa. Nevertheless, radon data from nN rays per view can be reconstructed by OPED, for any odd natural number n. This is achieved by means of adding empty cells to the acquired data set in order to match the original geometry, and then filling the cells through interpolation.

The acquisition of these higher resolution data sets is illustrated in figure 4.1. We will consider data sets for the case of $n = 3$. We chose this factor for practical reasons, since it is the lowest of the possibilities. Larger factors produce better reconstructions (figure 4.2), but the interpolation schemes are the same.

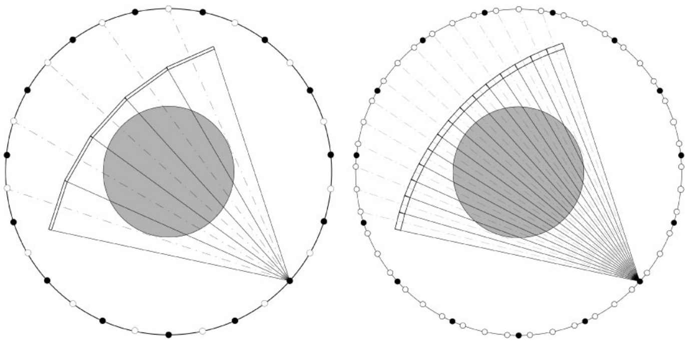

Figure 4.1: Left: the original OPED resolution for $N = 15$ views (represented by black dots) and N rays per view (white dots). Right: if $2N$ rays per fan view are added (resolution increase by a factor of n = 3), there are $2N$ views missing to match the original geometry.

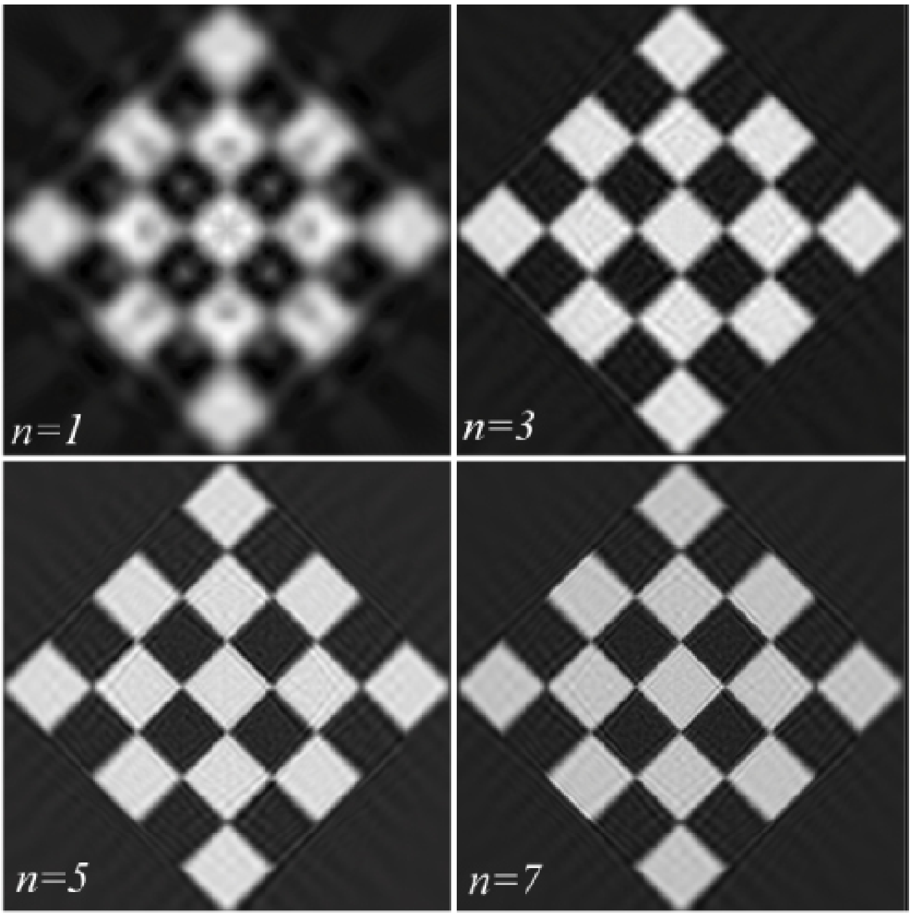

Figure 4.2: Justification of the interpolation process; reconstructions from fan data with $N = 111$ fan views made with different values of n.

In order to process this data, we need to add two free columns between every column of measured data in the fan beam representation (figure 4.3 a.). This is equivalent to adding positions of the source (or "views") for which no data are acquired. After reordering this data matrix, the resulting Chebyshev sinogram (figure 4.3 b.) presents the pattern depicted in figure 4.3 c; Every row contains two empty cells between every two measured Radon data. Those empty cells are the ones that must be filled in with interpolation before applying OPED to reconstruct the image.

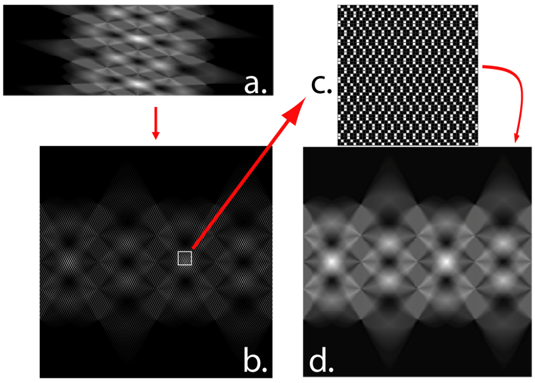

Figure 4.3: When the acquired fan data **(a.)** are reordered to a sinogram of parallel data in the case of $n = 3$ **(b.)**, the $2N$ missing views from figure 4.1 appear as two empty cells between every data point **(c.)**, which must be interpolated to obtain the final sinogram **(d.)**.

4.2 Test objects and methods

The parameters of the four analytic phantoms used in this study are displayed in table 4.1. The first and the second phantoms are binary chess boards with 2 x 2 and 5 x 5 cells, respectively. The third phantom, a Shepp-Logan head phantom [Shepp 74], was used to test the reconstruction accuracy of the reconstructed images. An edge phantom was used to test the spatial resolution in the reconstructed images using the method proposed by Fujita et al [Fujita 92], which requires a 3°-tilt of the edge. This method was developed to measure the MTF of digital flat-panel detectors and not for CT images, where also the reconstruction algorithm plays a role in the resolution. However, the program `MTF_Kante.pro` (included in the attached CD), written in IDL language by Egbert Buhr & Hartmut Illers (PTB Braunschweig) to implement Fujita's method, resulted useful to compare the results from our different interpolation schemes.

The fan-data for the simulated phantoms were generated using the programs `fan_data.pro` and `fan_data_sl.pro`, The Chebyshev sinograms were then created using `transformh.pro` and its subroutines[1]. The sinograms were then reconstructed using the algorithm OPED, explained previously in section 2.2.

---

[1] All program-codes can be found in the attached CD.

Table 4.1: Phantom data and reconstruction parameters

Phantom	Rotation(°)	Fan angle (°)	Number of views	Reconstruction grid
2 × 2 chess board	0	60	51	512 × 512
5 × 5 chess board	45	39	51, 89	512 × 512
Shepp-Logan	0	180	from 11 to 601	256 × 256
Edge Phantom	3	39	601	512 × 512

4.3 1-D interpolation

The missing data (black cells in figure 4.3 c.) can be generated using 1-D interpolation functions. This process is similar to the rebinning used for the reconstruction with FBP. However, in the framework of OPED, the measured data are left unchanged because they are already in appropriate positions, that is, they are already located at zeros of the Chebyshev polynomial $T_{3N}(t)$. Furthermore, rebinning, which is necessary for FBP, is fulfilled via two-dimensional interpolation in the space of the fan beam data. In our case, the interpolation is carried out directly within the Chebyshev sinogram. The measured data are equally spaced in the horizontal direction in the Chebyshev sinogram, as it can be seen in figure 4.3. Making use of this advantage, we interpolate the existing data for each fixed t_j. That is, we apply 1D-interpolation methods to every row of the sinogram.

4.3.1 The interpolating functions

There are many possibilities to interpolate in a 1D equidistant data set. We use linear interpolation, natural cubic splines [Bachvalov 87] and an intermediate compromise between them, the so-called “parametric” or “damped” splines [Späth 95].

The mathematical description of the parametric splines employed is given in the following. If ϕ_i is the ϕ-coordinate of the i^{th} measured data value, we define the dependent variables v and u as follows

$$v = \frac{\phi - \phi_i}{\phi_{i+1} - \phi_i}, \qquad i = 1, ..., N, \qquad \text{and} \tag{4.1}$$

$$u = 1 - v. \tag{4.2}$$

For the case of periodic Chebyshev sinograms we define $\phi_{N+1} = \phi_1$. Then the i^{th} section of a rational spline r_i is obtained as

$$r_i = A_i u + B_i v + C_i \frac{u^3}{pv+1} + D_i \frac{v^3}{pu+1}. \tag{4.3}$$

The parameters A_i, B_i, C_i and D_i are strictly determined by the smoothness conditions of the spline (the curve and its first two derivatives must be continuous) and the periodicity condition (r_N must join the data ϕ_N and ϕ_1). In the case of an exponential spline, its i^{th} section is defined as

$$e_i = A_i u + B_i v + C_i g_i(u) + D_i g_i(v), \tag{4.4}$$

where , ∀ u and p $\neq 0$,

$$g_i(u) = \frac{\sinh(pu) - u\sinh(p)}{\sinh(p) - p}. \tag{4.5}$$

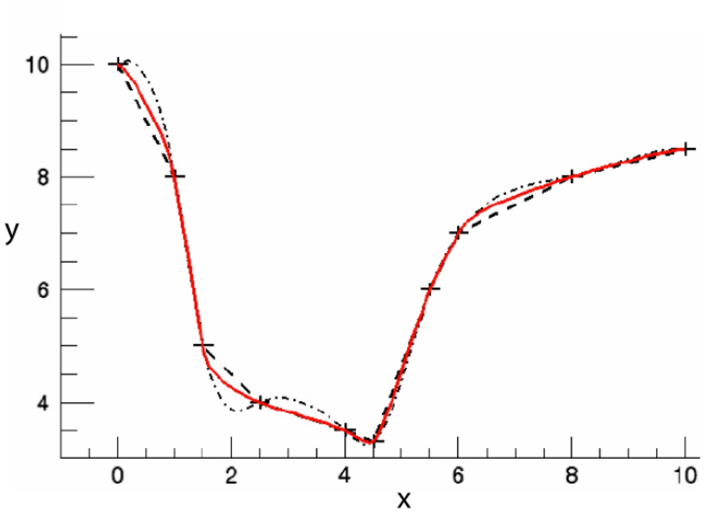

Figure 4.4: Behaviour of the different interpolating functions for an arbitrary sample of data: linear interpolation (dashed curve), cubic spline (dashed-dotted curve) and rational spline for a damping parameter $p = 5$ (bold, red curve). The original, sparse data values are shown by crosses. Note how the rational spline fits the data smoothly but with less variations than the cubic spline (data example taken from [Späth 95]).

A value of the damping parameter $p = 0$ in a parametric spline corresponds to a cubic spline, which consists of piecewise cubic polynomials. The higher the value of p, the more stretched the curve will be and thus closer to the linear interpolation segments. When p becomes infinity, the last two terms become zero and we obtain linear interpolation. The regarded values of p in our study were set between $p = 0$ and $p = 2$ with an increment 0.1. Results for the values $p = 5, 10, 20, 50, 80$ and $p = 100$ were also obtained. The algorithms for periodic rational splines and periodic exponential splines were taken from [Späth 95] and adapted to our special case in IDL language.

Linear interpolation hardly accounts for singularities, whereas cubic splines may depart too much from the measured data in some cases. Parametric splines, in particular the "rational" and "exponential" splines, were a priori estimated to be the most appropriate for our case because the total variation of the curve can be controlled by a parameter p, so that large differences from the measured data can be avoided. Figure 4.4 shows an example of the three methods for an arbitrary sample of data.

4.3.2 The drawback of our 1-D interpolation

The analysis of the MTF for the reconstruction of our simulated edge phantom showed a clear inhomogeneity (figure 4.5). The MTF is higher when measured in regions closer to the centre of the picture as when measured near the margins. The consequences can be identified in figure 4.6, where the reconstruction of a tilted 5x5 board is shown; the data for the reconstruction shown on the left were acquired with $n = 9$ to show this effect more clearly. The data on the right were acquired with $n = 3$ using the same total amount of rays. The reconstructed images show a "circular smoothing" behaviour, although this effect is only apparent in cases of high n.

The explanation is found in our interpolation process. The interpolation is carried out in

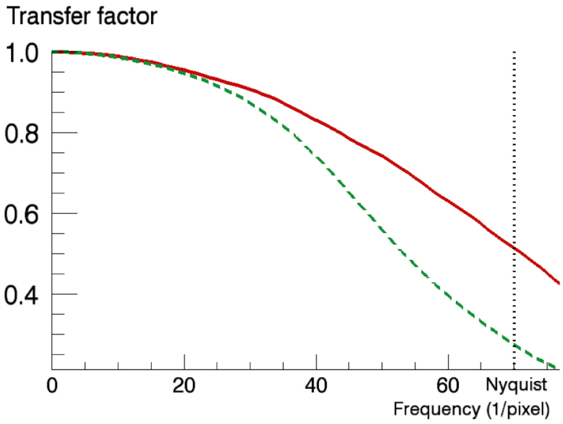

Figure 4.5: The MTF measured in a region close to the centre of the picture (solid, red line), and in a region closer to the margin (dashed, green line).

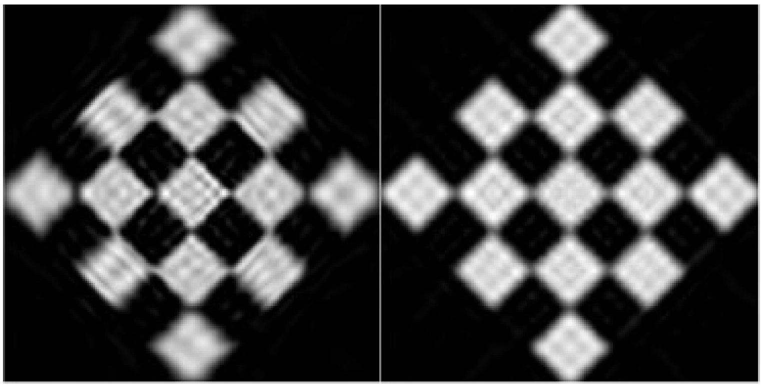

Figure 4.6: The drawback of the 1-D interpolation process can be observed in this reconstructed 5x5 chess board for $n = 9$ (left). However, this effect is not significant in the case studied in this article ($n = 3$, right).

rows corresponding to data collected over rays at a constant distance t off the center of the image. Therefore, each data row of the sinogram represents data from a different concentric circumferences with radius t in the image. In figure 4.7, each dot corresponds to one cell of the Chebyshev sinogram. The measured data are plotted as white dots and the empty cells in between are shown as black dots. It is evident that the measured neighboring data are more spaced in the outer circumferences. As a result, the higher uncertainty in the interpolation makes the data rows smoother in the outer regions in the image. Consequently, larger circular smoothing and lower spatial resolution appear as the distance to the center increases.

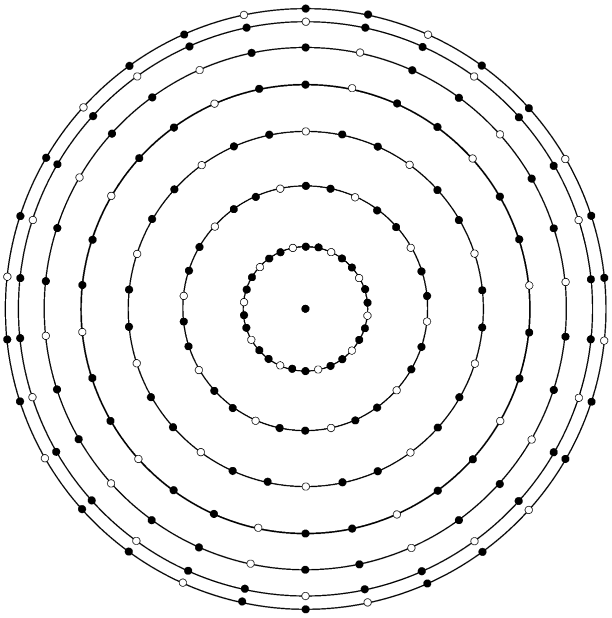

Figure 4.7: The explanation for the drawback of our 1D-interpolation process. Every row in the Chebyshev sinogram contains data from one of the concentric circumferences. Note the larger separation between data (white dots) in the outer circumferences.

4.4 2-D interpolation

This drawback of the chosen 1-D interpolation may be strongly reduced by using 2-D interpolation. It can be observed in figure 4.7 that the measured data are actually more concentrated in the outer regions than in the inner ones, i.e. the concentric circumferences are closer together in the outer regions than in the inner ones. This is due to the distribution of the zeros of the Chebyshev polynomials. An appropriate 2-D interpolation technique, capable of taking into account the measured data from the nearest rows (or circumferences), as well as those from their own row, should provide more accurate interpolated values and avoid the circular blurring. The suggestion of appropriate 2-D interpolation methods is, therefore, the topic of this section.

We have used the kernels and the local procedure presented in [zu Castell 08], which is very briefly introduced below[2]. Additionally, as outlook for this chapter, it would be recommendable to try the method of normalized convolution [Piroddi 04] for the interpolation task. This method has proved very successful for sparse data matrices where 90 % of the data is missing [Piroddi 04]. Therefore, we expect to obtain good results for our matrices, where only two thirds of the data are missing.

Interpolation using kernels

Data from sampling the two-dimensional Radon transform naturally lives in the projective plane. Thus, one should use the metric of the projective plane to define suitable similarity measures for scattered data interpolation of Radon data.

---

[2] The details of this method are not given here because they do not belong to the author of this work and they are being further developed yet. Please refer to castell@helmholtz-muenchen.de or R.Beatson@math.canterbury.ac.nz for details.

Interpreting the projective plane as a homogeneous space allows using concepts of harmonic analysis to derive a characterisation of the class of continuous, positive definite basis functions. They can then be identified with kernels on the sphere with an additional symmetry property. Therefore, examples for kernels for the projective plane can be obtained by symmetrisation of zonal kernels on the sphere.

For the interpolation of the sinograms, we used three types of kernels; the thin plate spline (TPS) is the analog for the projective space of the radial basis function which is tied up with minimizing linearized curvature. The spherical kernel is a function with polynomially decaying Fourier coefficients. The last example (local) is based on a slightly modified version of the standard interpolation procedure. For every point, the sixty closest data points have been fitted using the 3D-biharmonic basis function.

4.5 Results

Results with the 1-D interpolation functions discussed in chapter 4 are presented in section 4.5.1. Results obtained with 2-D methods are shown in section 4.5.2. These results can be applied to any large matrix where a large computational expense can become a problem, for example to produce the missing data using the scanning geometry CT D'OR.

4.5.1 1-D interpolation

In this section, results are presented first for linear and for cubic spline interpolation. Afterwards, the results obtained with parametric splines are presented separatedly. At the end, we summarize the reconstruction accuracy and the spatial resolution comparing all 1-D methods together[3].

Linear and cubic spline interpolation

The influence of linear and cubic spline interpolation within the sinogram of a chess-board phantom is shown in figure 4.8.

The bar diagram of figure 4.9 shows the relative decrease in the NMSE (defined in equation 2.15) with respect to the case of no interpolation, the corresponding value of which is denoted as NMSE_0, that is,

$$\mathrm{NMSE}_{\mathrm{Decrease}} = 100 \left| \frac{\mathrm{NMSE} - \mathrm{NMSE}_0}{\mathrm{NMSE}_0} \right| . \tag{4.6}$$

Natural cubic splines give, in general, the best results in the reconstruction accuracy (figure 4.9) and its computing time is not significantly increased in comparison to linear interpolation[4]. Although the improvement obtained by cubic splines also decreases with the number of views, the best choice for our interpolation process seems to be a cubic natural spline.

---

[3] These results were presented at the DGMP congress 2006 of the German Society for Medical Physics in Regensburg and the author achieved the DGMP Nachwuchspreis 2006 [de las Heras 08b].

[4] For the cases of 601 fan views, the interpolation of the corresponding 1803x1803 matrix using rational spline interpolation as described above needs about 45 seconds whereas the linear or the cubic spline interpolation take less than 5 seconds (using IDL programming language, Intel Pentium 4 computer, CPU 3.00 GHz, 1.00 GB RAM).

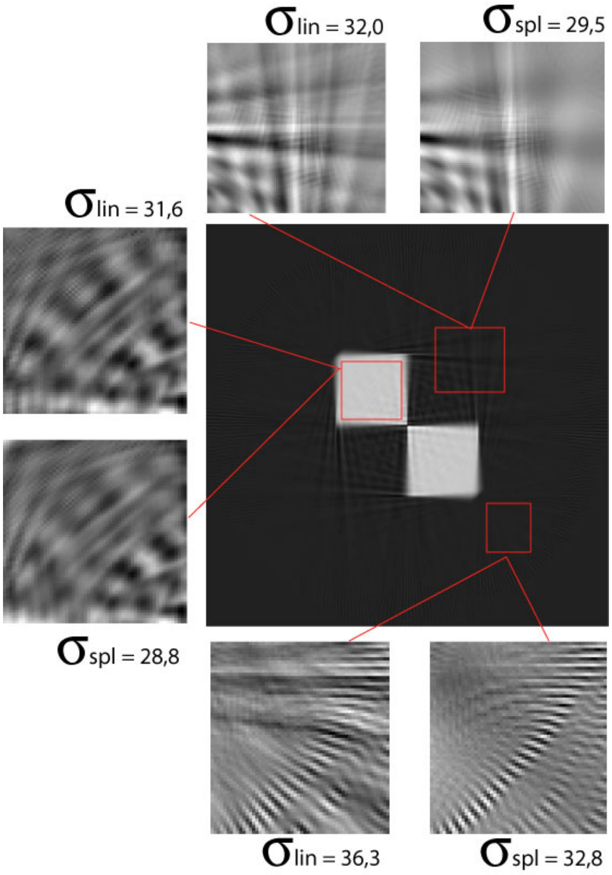

Figure 4.8: `06-stdev.pdf`: The standard deviation as an estimation of the artefacts in three different regions that are originally homogeneous ($\sigma = 0$, as defined in equation. 2.19). Results after using linear and cubic spline interpolation are marked with σ_{lin} and σ_{spl}.

In fact, it is known [Bachvalov 87] that the error of the cubic spline function, S, to the function I which is interpolated is bound by

$$\max_{x \in [-1,1]} |I^{(q)}(x) - S^{(q)}(x)| \leq Ch^{4-q} \max_{x \in [-1,1]} |I^{(4-q)}(x)|,$$

where C is constant, $h = 2\pi/N$, $q \leq 3$, and $I^{(q)}$ is the q^{th} order derivative of I. The function I in our case is the Radon transform of the function that represents the image. Therefore, the use of cubic splines is justified.

The potential disadvantage of using cubic splines is that they depart from the data near sharp discontinuities. Nevertheless, this effect does not seem to have a significant influence in the usual CT-data matrices employed in the clinical practice. In these cases, the singularities are not large enough to force the spline to separate much from the data.

Parametric or “damped” splines

An example of the potential efficiency of parametric splines is shown in figure 4.10 for the case of 11 fan views. The image quality achieved by rational splines and by exponential

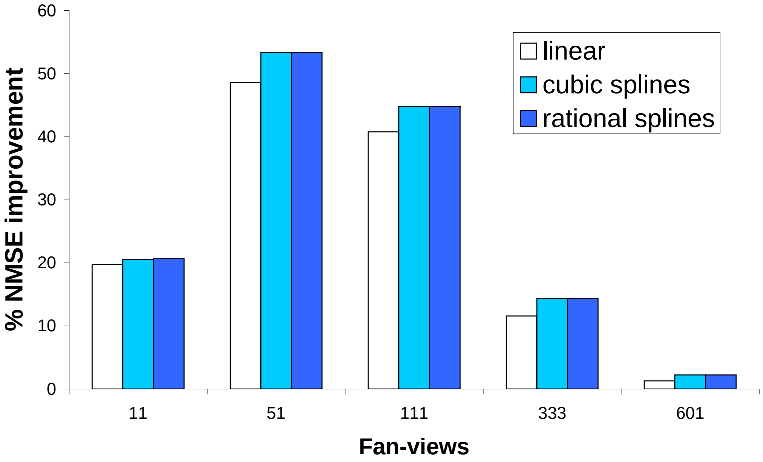

Figure 4.9: Relative decrease in the NMSE of the reconstructions in comparison to the case where no interpolation is used, as defined in equation (4.6).

splines is very similar. Therefore, in the following only results obtained via rational splines are presented.

Parametric splines do not improve significantly the results obtained by cubic splines. Only when the number of fan views is small, the reconstruction accuracy achieved by these splines at the best value of the parameter p appears to be higher than the one achieved by cubic splines (although only by less than 0.25 %, as shown in figure 4.10). This behaviour, however, no longer holds for a larger number of fan views (see table 4.2 and figure 4.9). These splines do not lead to any improvement over cubic splines in the case of large data matrices. The table shows that the MRE is more influenced by the parameter p but not in a very significant way.

Parametric splines were developed to avoid the disadvantages of cubic splines, while maintaining its smoothness. Nevertheless, for a typical medical CT-data matrix, cubic splines are already very close to linear interpolation (as explained above) and any "stretching" added to them by the parameter p may make the curve sensitive to the problems faced by the linear interpolation. Furthermore, they require a longer computing time and an additional step to determine the most appropriate value for the parameter p.

Consequently, these splines do not seem to be beneficial enough for practical medical CT. However, their ability to improve the results obtained by cubic splines may be valuable in some other CT applications such as micro-CT, or whenever only a small amount of views is available (e.g. nuclear medicine or TomSAR, i.e. Tomography with Synthetic Aperture Radars).

Reconstruction accuracy

Precise values of the reconstruction accuracy, after using various interpolation functions, are presented in Table 4.2. The values obtained by the same number of views but without in-

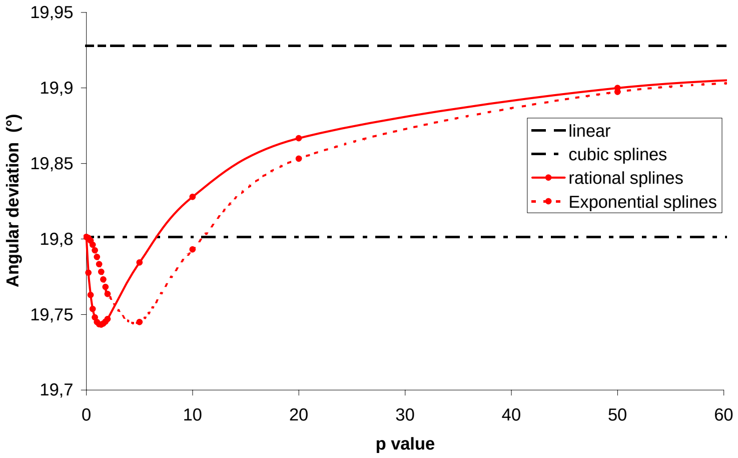

Figure 4.10: **Behaviour of parametric splines in the case of 11 fan views**. The best result is attained at $p = 1.3 \pm 0.1$ for rational splines and at $p = 5.0 \pm 2.5$ for exponential splines. The “angular deviation” shows the Hilbert Angle introduced in equation 2.17.

creasing the resolution, where no interpolation is necessary, are also shown for comparison.

Analysis of the spatial resolution

The measurements of the spatial resolution (figure 4.11.b.) show a similar behaviour to the reconstruction accuracy previously shown. For example at a tenth of the Nyquist frequency, the MTF takes the value 0.85 when no interpolation is used, while the MTF resulting from increasing the resolution and using interpolation is over 0.95. At around half of the Nyquist frequency, i.e. at 35 pixel^{-1}, the MTF becomes zero in the case of no interpolation, while for the other cases it is still over 0.5. The curve corresponding to cubic spline interpolation is the highest of all. The curves for the parametric splines lie between this one and the one for linear interpolation. The slight increase in the lower MTF at around 50 pixel^{-1} is due to the larger amounts of artefacts present in this case, which can be clearly be seen in its profile (dashed curve in figure 4.11.a.).

4.5.2 2-D interpolation

The 2-D Thin Plate Splines introduced in section 4.4 seem to have advantages for the resolution of the reconstructions (figure 4.12). Furthermore, the inhomogeneous blurring produced by the 1-D interpolation process (section 4.3.2) can also be avoided using the 2-D methods. figure 4.13 shows the result of the local method (also introduced in section 4.4) compared to the reconstruction obtained with 1-D splines.

Table 4.2: Accuracy of the Shepp Logan phantom reconstructions.
[a]Normalized Mean Squared Error, [b]Mean Relative Error.

		Interpolation method		
	without interpolation	linear	cub. spl.	best rat. spl. (p)
11 views				
Hilbert angle (°)	24.11	19.93	19.79	19.74 (1.3)
NMSE [a]	0.4086	0.3413	0.3387	0.3379 (1.2)
MRE[b]	0.1800	0.1123 (!)	0.1128	0.1124 (100)
51 views				
Hilbert angle (°)	13.63	9.100	8.684	
NMSE	0.2358	0.1586	0.1511	
MRE	0.08808	0.03595	0.03453	0.03432 (1.1)
111 views				
Hilbert Angle (°)	8.711	6.174	5.9307	
NMSE	0.1517	0.1077	0.1034	
MRE	0.04276	0.01883	0.01834	0.01814 (1.7)
333 views				
Hilbert Angle (°)	5.239	4.694	4.565	
NMSE	0.09140	0.08192	0.07965	
MRE	0.01526	0.009214	0.008788	
601 views				
Hilbert Angle (°)	4.621	4.563	4.521	
NMSE	0.08065	0.07962	0.07888	
MRE	0.009802	0.007920	0.007766	

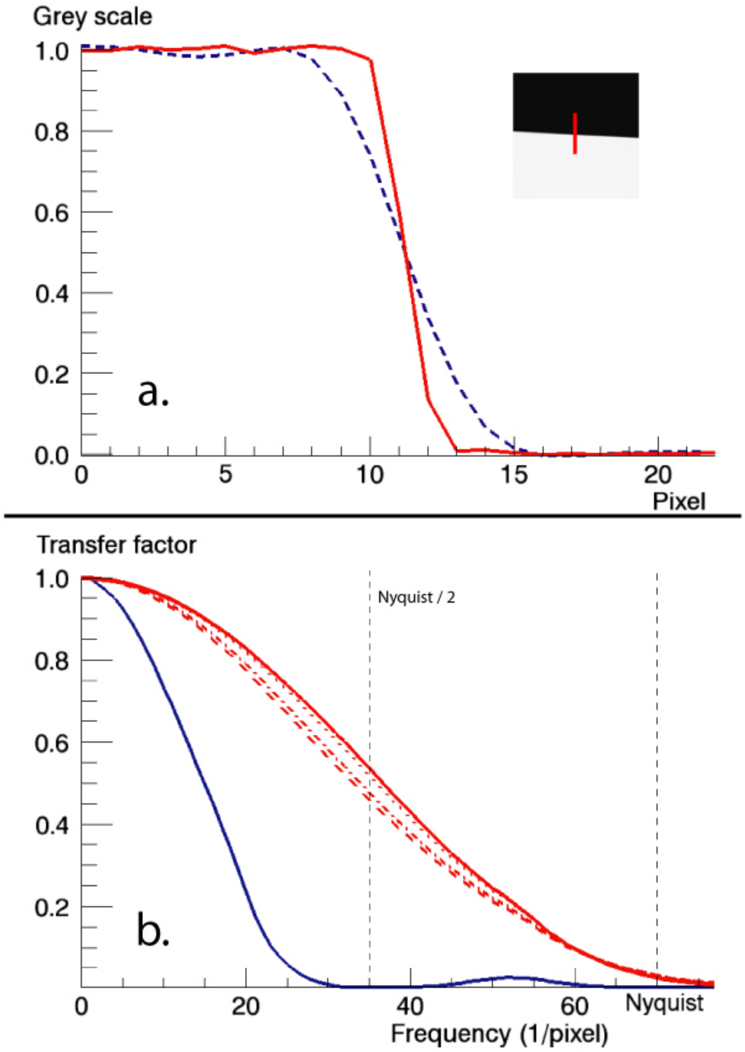

Figure 4.11: **a.**: Grey value of 20 pixels around the reconstructed edge (profiles) used for the MTF measurements shown in part b. of this figure. The solid line corresponds to the cubic spline interpolation and the dashed line corresponds to the case where no interpolation has been used. **b.**: The measured MTF for the different interpolation possibilities. Cubic spline interpolation (upper solid line), rational spline interpolation for $p = 1$ (dotted curve) and $p = 10$ (dot-dashed curve) and linear interpolation (dashed curve). Also shown is the MTF when no interpolation is used (lower solid line). The Nyquist frequency is shown with a vertical line at 70 pixel^{-1}.

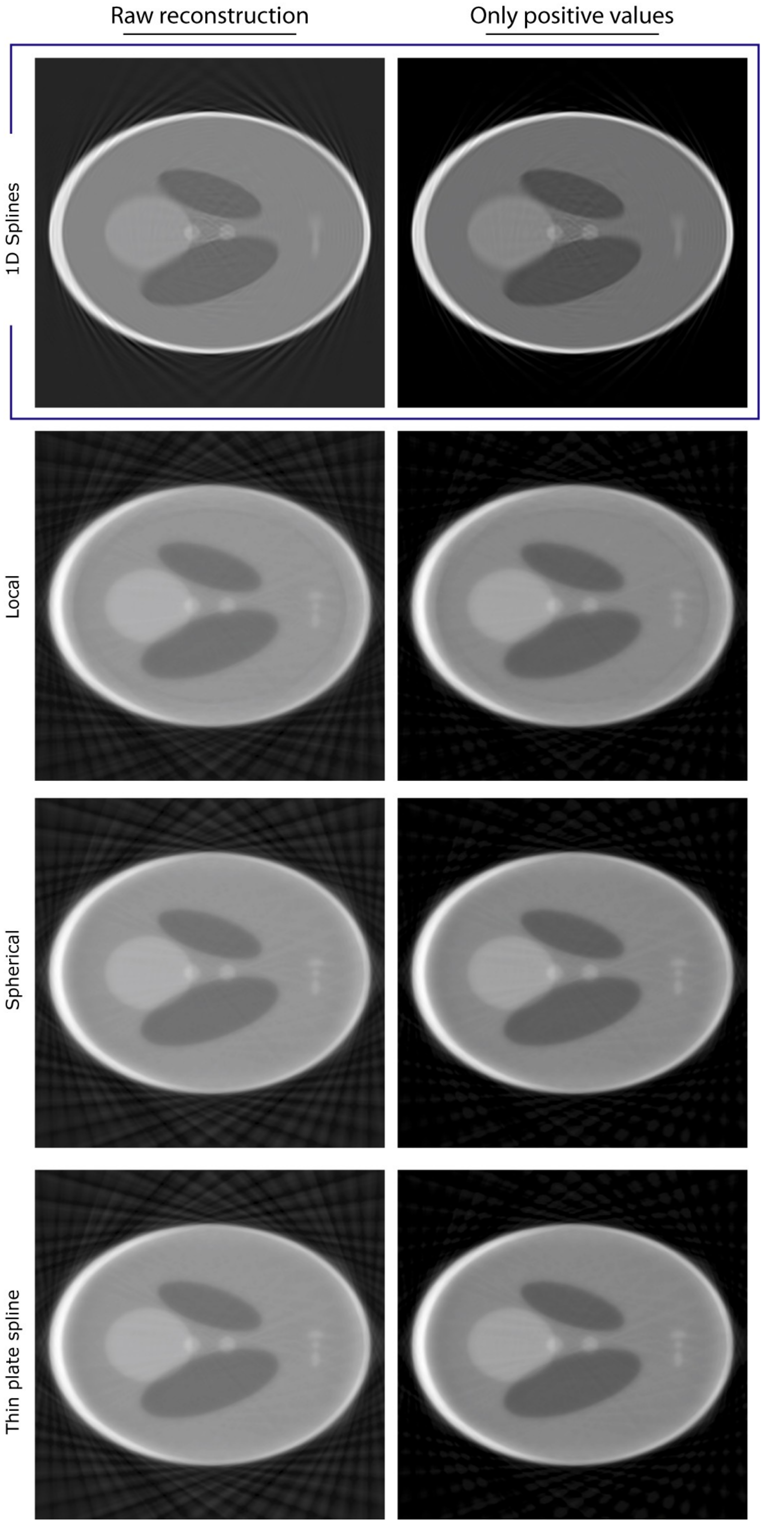
Raw reconstruction
Only positive values
1D Splines
Local
Spherical
Thin plate spline

Figure 4.12: `04-TPSsh.pdf`: Reconstructions obtained using 2-D interpolation methods within the sinogram of the Shepp-Logan phantom. Note the three small ovals at the bottom, which are better resolved using the thin plate splines.

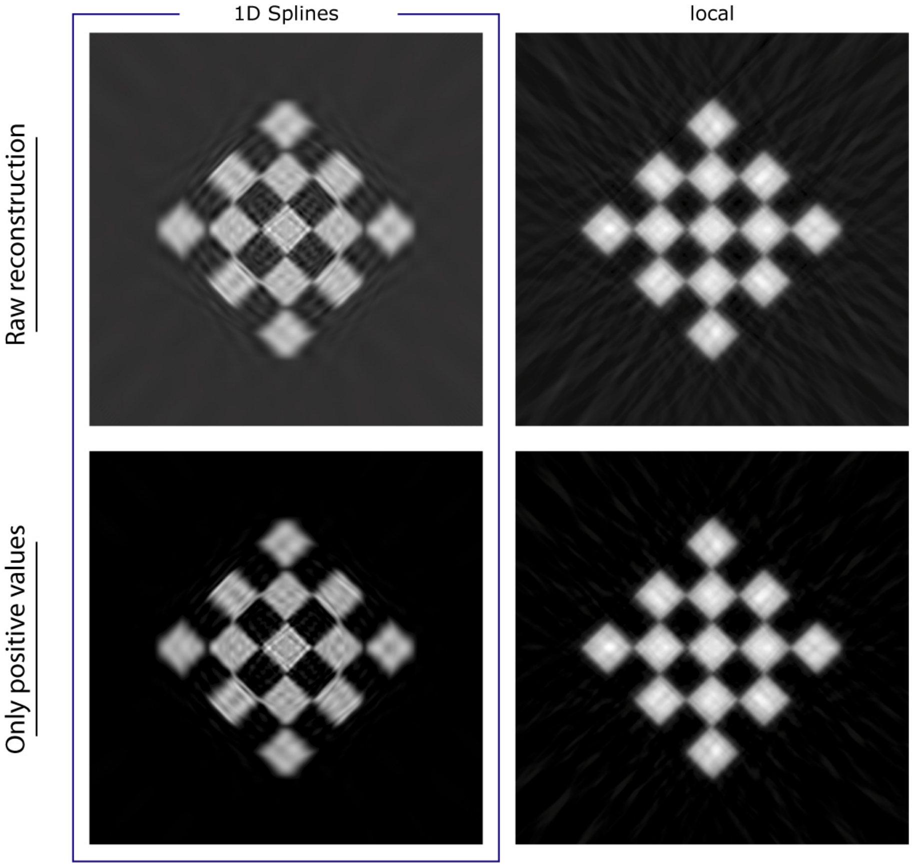
1D Splines
local
Raw reconstruction
Only positive values

Figure 4.13: `04-TPSch.pdf`: Reconstructions of the phantom used in section 4.3.2 to show the drawback of the 1-D interpolation process. **Left:** The same reconstruction shown on the left in figure 4.6, repeated here for comparison. **Right:** Reconstruction of the same data, obtained using the local 2-D method of sinogram interpolation, described in section 4.4.

Part II

Experimental part

Chapter 5

Materials and Methods

This chapter introduces the experimental part of this work. It describes in detail in section 5.1 the design and construction of the device developed to test the idea of the scanner CT D'OR. Section 5.2 deals with the test objects or "phantoms" used in the measurements, whose reconstructions can be found later in chapter 7 on results. Sections 5.3 and 5.4 present the experimental set-ups for the tests of the device, both in the Helmholtz Zentrum München and in the TUM-Klinik Rechts der Isar.

5.1 A test-device for CT D'OR

The purpose if this work was to build a test-device for the scanning geometry of CT D'OR. The device built is a "demonstrator" because it is intended to test the principle of CT D'OR. It was not designed to scan patients. For this test of principle, a ring capable of 2-D scans is appropriate, because 3-D scans can be thought of as a superposition of 2-D slices.

In the following, the details of the device are presented; its dimensions, detectors and shielding elements, the software used for the data acquisition and the software used by the rotation desk to spin the whole assemble during the measurements.

5.1.1 Design

The device needed to be big enough to be able to image objects of clinically-relevant size, but also small enough to fit in the radiation room of our research centre and to be easy to transport to the clinic. Furthermore, the fan-angle of the available radiation sources was limited. It would not have been meaningful to construct a big device if it cannot be irradiated a large portion of its surface. Thus, the device was designed to have a radius of half a meter.

On the other hand, the number of detectors needed to be large enough to obtain enough resolution (to "see the seeds of an orange"), but also small enough to be affordable for a reasonable prize for a demonstrator and be practical to be fixed into the device. Since the number of views acquired in the mask is equal to the number of detectors in it, we decided that about 200 detectors would accomplish a reasonable resolution. For comparison, the first CT-prototype constructed by Hounsfield in 1971 used 360 views (i.e. one projection per degree [Hounsfield 73]).

The device basis chosen is a ring of Plexiglas (PMMA) with 197 holes[1] for the detectors and their shielding elements. The distance from each hole to the centre of the device is 25 cm. The design details are shown in figures 5.1 and 5.2. These figures were given to the workshop of the Helmholtz Zentrum München for the manufacture of the Plexiglas-holder and the shielding elements. Observe that the shape of the mask-detectors is circular, thus forcing a larger size of the shielding elements than the size of the detectors (as explained before in section 2.1.3). Since the test-device was intended for a proof of principle, and not for clinical use with patients, we decided to buy cheaper, practical detectors, rather than more expensive detectors with a more appropriate design.

---

[1] At the time of design, the number of views employed by OPED had to be odd. However, OPED does not have this limitation anymore.

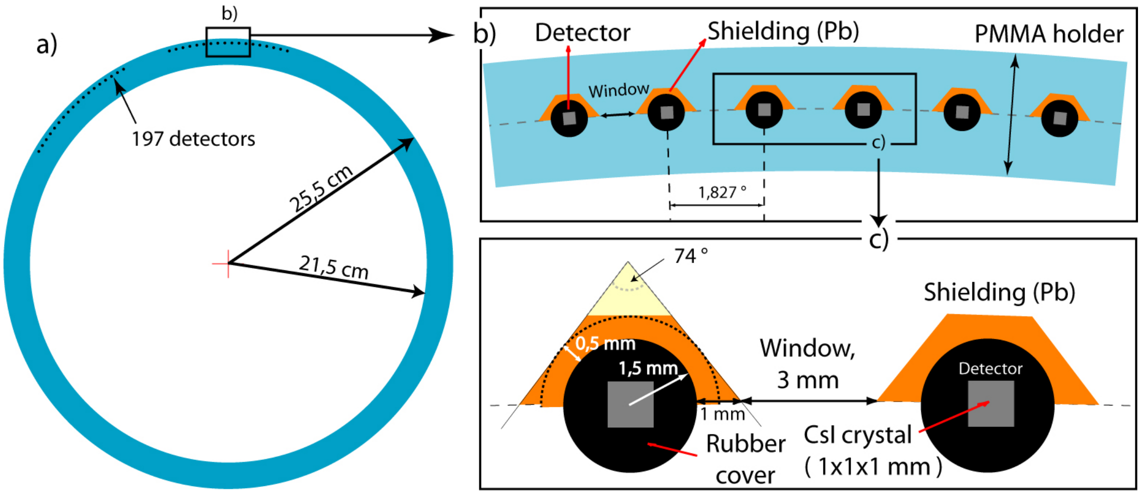
a)
b)
197 detectors
25,5 cm
21,5 cm
b)
Detector
Shielding (Pb)
PMMA holder
Window
c)
1,827 °
c)
74 °
Shielding (Pb)
0,5 mm
1,5 mm
Window,
3 mm
Detector
1 mm
Rubber
cover
CsI crystal
(1x1x1 mm)

Figure 5.1: **Design of the demonstrator's mask (top view)**.

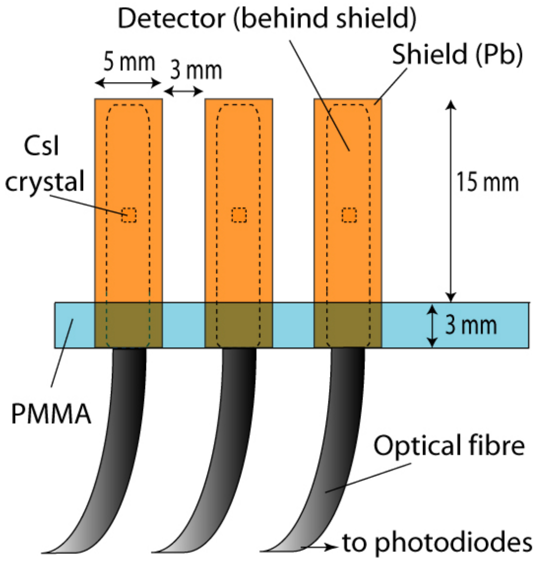
Detector (behind shield)
5 mm
3 mm
Shield (Pb)
CsI
crystal
15 mm
3 mm
PMMA
Optical fibre
to photodiodes

Figure 5.2: **Design of the demonstrator (radial view)**. Note that the efficient surface of the detector is only 1 mm^2.

5.1.2 Detectors

The detector elements are CsI(Tl)-scintillator crystals[2] of 1 mm^3, covered by a reflecting coating of TiO_2 to improve light capture efficiency and wrapped in a protective rubber cover. This "detector head" (Figure 5.3 right) is connected to an optic fiber. This assemble was provided by Radcal Corp. [Sunde 06] (Monrovia, California). The fiber ends in a photo-diode (see Figure 5.3 left) that collects the light for a time to be chosen. The photodiodes and their ports were produced and assembled by IBA Dosimetry GmbH (formerly Scanditronix-Wellhöfer, Schwarzenbruck, Germany). The photodiodes at the end of the optical fibers are very sensitive to any external light. Therefore, we also designed especial cases to keep the photodiodes in the dark (figure 5.4).

The detector response at 50 to 110 keV is shown in section 5.3.1. The detector used to simulate the arc-detector of a CT is described with the second set-up in section 5.4.

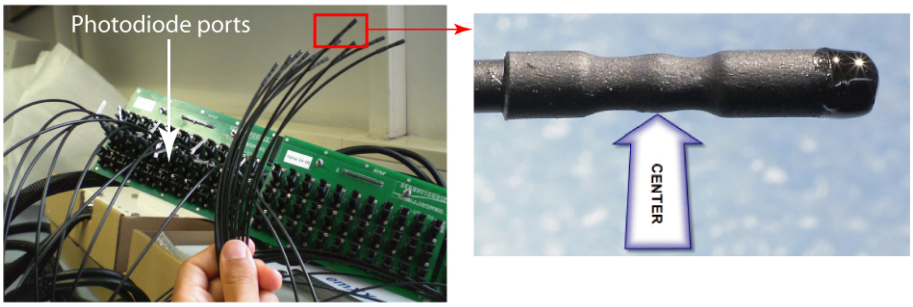

Figure 5.3: The ports of the photodiodes and close-up view of one detector. The right picture was provided by Radcal Corp. [Sunde 06]

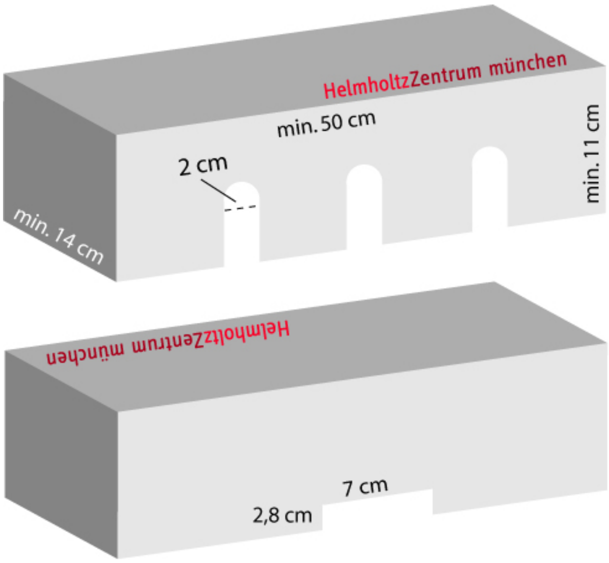

Figure 5.4: One of the two dark cases for the photo-diodes (front and back view). The three little doors at the front are big enough for 33 fibers to pass through each one of them. The slit at the back has the size of the port connexion to the computer.

---

[2] For physical properties of CsI(Tl), see Appendix.

5.1.3 Shielding elements

The lead shielding elements were made by pressing thin stripes of lead inside a press-form constructed especially for our case (Figure 5.5 top-left). An hydraulic press up to 300 bar (Matra-Werke GmbH, Frankfurt, Germany) was available at the workshop for this purpose. The pressed stripes of the desired form were cut into pieces of 1.8 cm length (Figure 5.5 top-right) to shield the whole detector-head on one side.

The shields were glued to the detectors using silicon, and the two together were stuck in the holes of the Plexiglas basis using a stronger type of silicon (figure 5.5 bottom-left). This second kind of silicon was also supposed to fix together the optical fibers and the detector head. However, the large tension forces suffered by the fibers during the measurements made it necessary to use “instant glue” to avoid the fibers being ripped off the detector head. A close-up view of a section with 10 detectors in the finished mask is shown at the bottom-right of Figure 5.5.

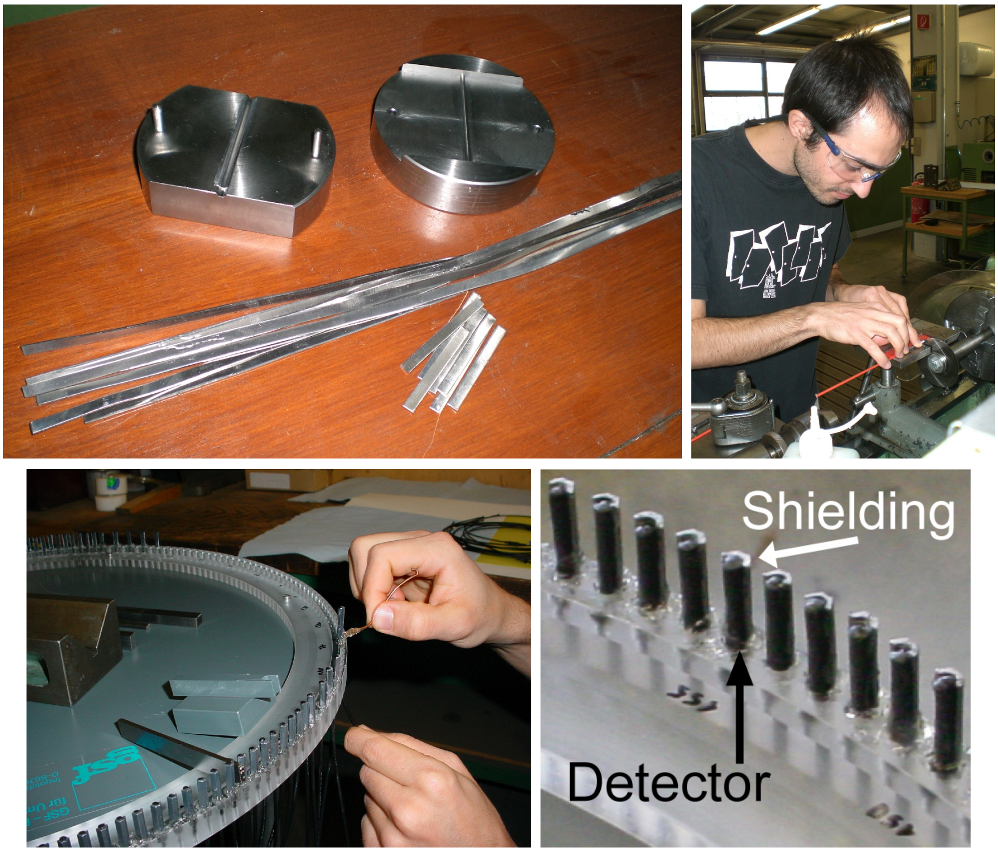

Figure 5.5: Construction of the mask at the factory (for explanation of each picture, see text above).

5.1.4 Data acquisition software

The software for data acquisition from the mask detectors was provided by IBA Dosimetry. It controls two ports, each one having 99 photodiodes. The first device, (Nr. 10458) is connected to detectors 100 to 198. The second device (Nr. 10459) is connected to detectors 1 to 99 (supplied by IBA). The interface enables a) the use of a file with calibration factors for each detector, b) a background correction, and c) the setting of the sample duration. For our purposes, only the last feature resulted useful, as explained in the following:

a. The supplied file with calibration factors had been obtained at a single photon energy and did not take into account the energy dependence of the detector response. Therefore, we had to carry out our own calibration, as described in section 5.3.1.

b. The background correction does not allow for several measurements of the background, but only for one. Therefore, we ignored the automatic background correction. Instead, we carried out ten measurements in absence of irradiation and subtracted the mean of those ten from each measurement with irradiation. This process was done for each detector individually.

c. Data from all detectors at the same time can be acquired in samples of as a short duration as 1 ms. However, we always used sample times above 16 ms. Smaller durations resulted in null samples between the measurements appearing at different moments in each device. Furthermore, smaller duration times would have made the size of the data too large to be practical.

5.1.5 The rotation desk

The device was mounted on a rotation desk from Phytron Elektronik GmbH (Gröbenzell, Germany), and the whole assemble was screwed to an aluminium plate to provide stability. The programs used to control the desk were written using LabVIEW 8.2 (National Instruments, Austin, Texas). The desk rotates a bit less than 360° when it is ordered to rotate 3600 times 0.1°, probably due to rounding errors in its software. Therefore, it was necessary to program a rotation of 365° to ensure a full rotation of the ring.

5.2 Test objects

Each one of the test objects or “phantoms” was designed to accomplish a specific purpose. We used three organic phantoms, two phantoms of Plexiglas to analyze image quality and a clinically-relevant phantom with real bones.

5.2.1 Organic phantoms

The first organic phantom was a pepper half (figure 5.6 left). It was chosen because of its organic tissue, its low absorption, its regions of air (for the high contrast), and its non-circular contour.

The second organic phantom was made of walnuts and corks inside synthetic resin (Voss Chemie GmbH, Uetersen, Germany[3]). The purpose of this phantom was to check if it was possible to image objects with higher absorption properties. Air bubbles were avoided in the resin by using a vacuum pump. The objects lie at different heights, so that one single slice of this phantom cannot catch all objects at the same time.

---

[3] From Voss we used the resin “Polyesterharz Viscovoss GTS” and the separating wax Trennwachs W-2.

The third organic phantom consists of six pepper slices. With this phantom, we wanted to obtain a larger amount of details as with the first one, and so take advantage of the large radius of our device. At the same time, we wanted to check the idea of the "empty scan", explained in section 5.3.4.

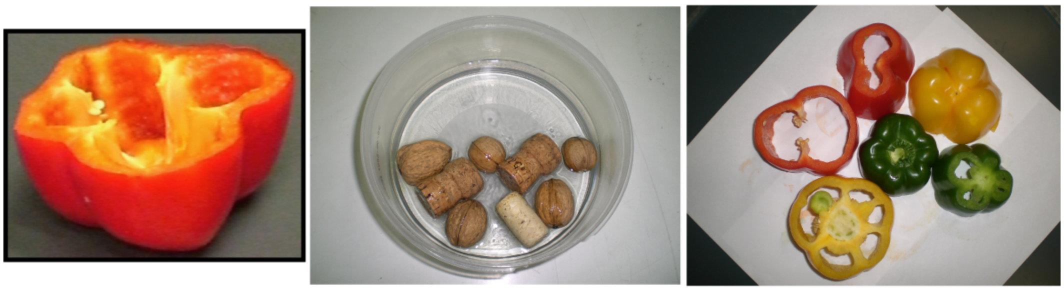

Figure 5.6: The three organic test objects.

5.2.2 Plexiglas semi-disk phantoms

In order to quantitatively characterize the imaging quality of the device, we designed two semi-disks of Plexiglas (figure 5.7). Both of them are designed so that noise and resolution can be measured at the same time from the same scan. Noise can be measured in the homogeneous regions of Plexiglas and air, applying equation 2.19. Resolution can be measured using the discontinuity between air and the flat surface of the phantom. Each phantom provides a different method to measure the resolution:

1. The first phantom presents a discontinuity of edge-type, as it is required by the Fujita edge-method[Fujita 92] to calculate the Modulation Transfer Function (MTF). We also mentioned this method in section 4.2 for theoretical calculations. However, this method was developed to measure the MTF of digital flat-panel detectors and it is not appropriate for CT images, where also the reconstruction algorithm plays a role in the resolution. Therefore, we developed a method to quantify the resolution properties of our detectors together with the algorithm, described in the following paragraph.

2. The edge-surface of the second phantom was coated with a 0.5 mm thin sheet of Tantalum[4] (Ta, Z = 73, from Cometec GmbH, Linsengericht, Germany). Using the coated surface, we reconstructed a profile perpendicular to the edge of the phantom. This reconstruction must be oversampled to avoid aliasing[5]. We then mirrored the air-side of the profile, thus obtaining a symmetric profile of the Point Spread Function (PSF), just as if the Tantalum sheet had been kept hanging in the air. The MTF is then calculated as the real part of the Fourier Transform of the PSF (see results in section 7.1.3).

---

[4] Tantalum is dark, dense, ductile, very hard, easily fabricated, and highly conductive of heat and electricity [Wikipedia 08]. Therefore, it is a good substitute for the more expensive and difficult to manufacture Tungsten (W, Z = 74), recommended in the norm IEC 62220-1:2003(E) [IEC 03]. Tantalum is used in recent papers related to our purposes [Flohr 07]. Stainless steel is also employed sometimes for this purpose [Nickoloff 87].

[5] See Moiré effect (artefacts due to undersampling 2-D images) in [Kak 88].

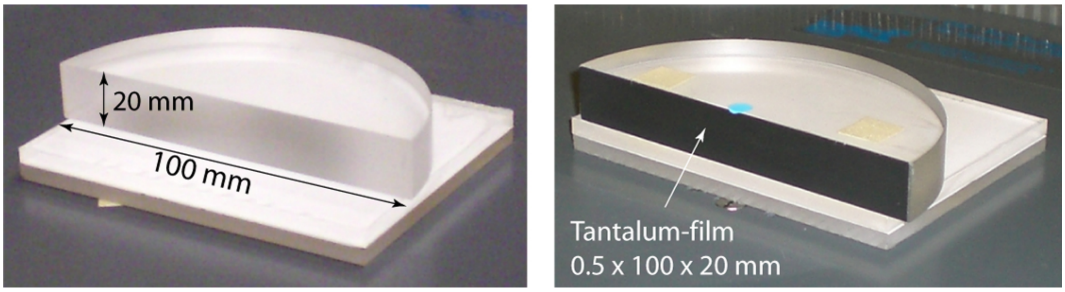

Figure 5.7: The semi-circle phantom without (left) and with the Tantalum sheet (right).

5.2.3 Head-slice phantom

For the clinical measurements, we used a slice of an Alderson-Rando phantom, shown in Figure 5.8. It is used for dosimetry at the Institute of Radiation Protection of the HMGU. It contains real bones and human tissue equivalent material. The slice chosen is at the height of the nostrils, so that we can reconstruct regions of air and analyze regions of high contrast.

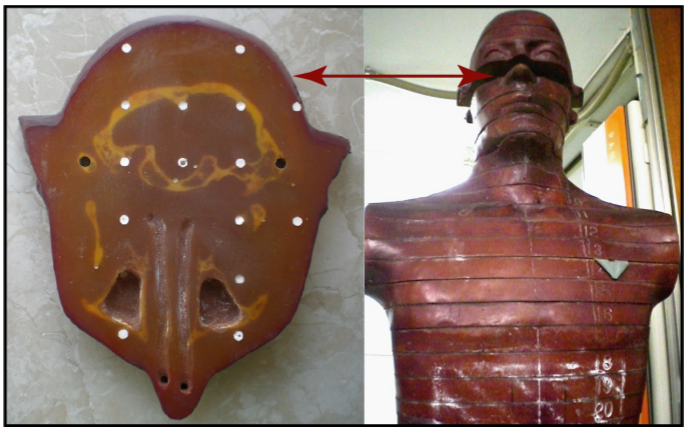

Figure 5.8: The head-slice from an Alderson-Rando phantom.

To check its internal structure, a CT-scan of the phantom is shown in figure 5.9 (obtained with a Siemens Somatom Sensation 64 with a slice thickness of 4 mm).

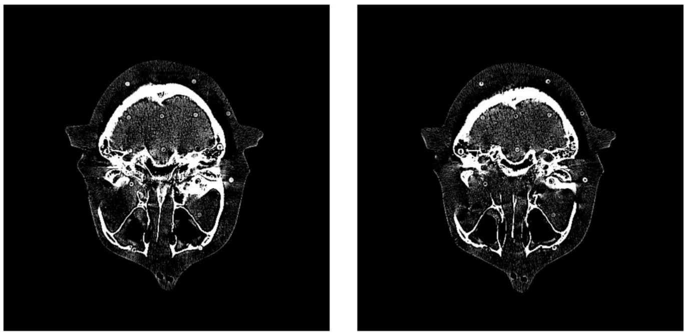

Figure 5.9: A CT-scan of the head-slice.

5.3 First experimental set-up

At first, we tested the device in the HMGU-Secondary Standard Dosimetry Laboratory (SSDL). The calibration of the mask detectors and the determination of the correction factors will be described first, before explaining the data acquisition process.

5.3.1 Detector Calibration

In order to calibrate the detectors before their installation in the device, they were irradiated in sets of 18 detectors at a distance of 169 cm from a radiation source (X-ray tube MCN 323 by Philips, Eindhoven, the Netherlands), as shown in figure 5.10. The size and the homogeneity of the irradiation field was checked with a fluorescent screen while wearing lead protection. The dose at that distance was measured with a ionization chamber M23361 - 290 (Physikalisch-Technische Bundesanstalt PTB, Braunschweig), the calibration of which was as well tested using a radioactive check source of Sr^{90}/Y^{90} and an Unidos dosemeter (PTW, Freiburg, Germany) also calibrated.

The detector responses were obtained for different input photon-energy spectra and different dose rates, as shown in table 5.1. The corresponding radiation-spectra are shown in figure 5.11.

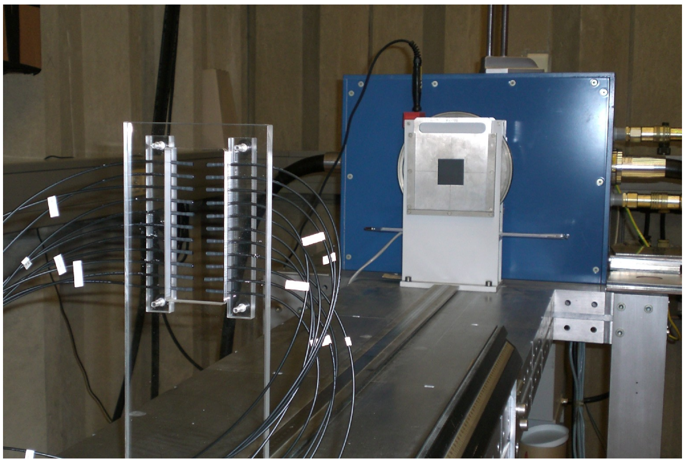

Figure 5.10: Set-up for the detector calibration.

Table 5.1: The parameters employed in the calibration of the detectors. An Al filter of 4.05 mm was used in all measurements.

Peak voltage (kV)	Current (mA)
50	3.75, 5, 7.5, 10, 12.5, 15
70	3.75, 5, 7.5, 10, 12.5, 15
90	3.75, 5, 7.5, 10, 12.5, 15
110	3.75, 5, 7.5, 10, 12.5, 15

Technical details of the radiation source can be found in section 5.3.3 and in the appendix.

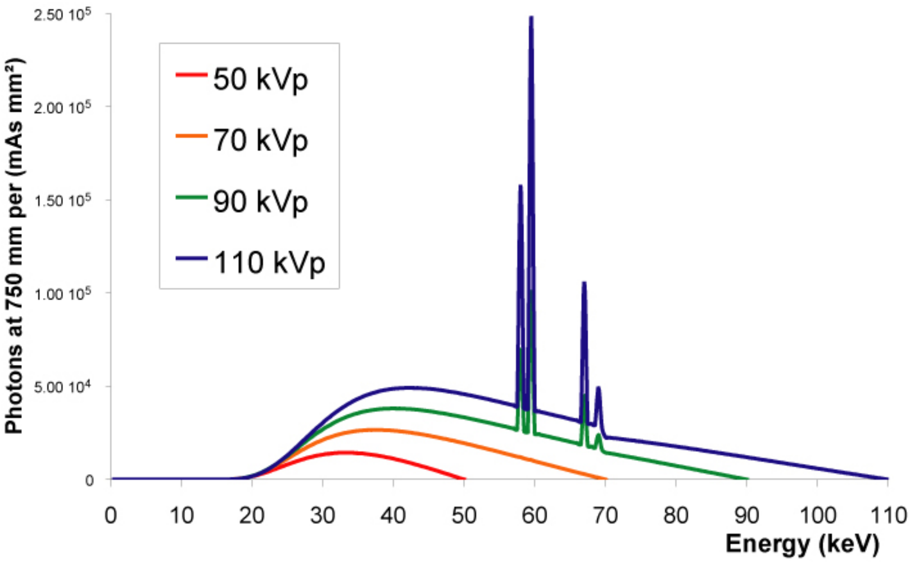

Figure 5.11: **X-ray spectra used for the calibration** corresponding to 50 (top-left), 70 (top-right), 90 (bottom-left) and 110 (bottom-right) kVp, attenuated by 4.04 mm Al, as given by the catalog of [IPEM 97].

A calibration factor can be obtained for every detector and every energy as the proportionality relation between absorbed dose and detector response (the slopes S_{50}, S_{70}, S_{90} and S_{110} of each curve in figure 5.12). This calibration can be used to estimate the dose in μGy from the detector readings at a given X-ray spectrum.

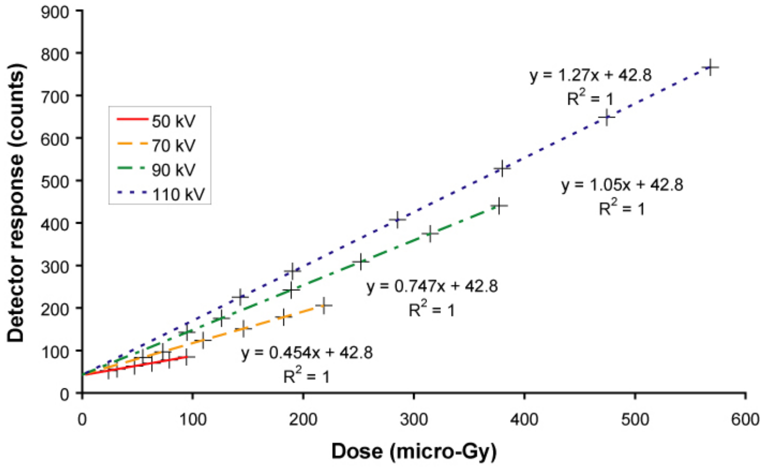

Figure 5.12: **Dependence of the detector response on the X-ray spectrum** (calibration curves). Example for detector number 1, measured in 1 s. All other detectors show a similar linear behavior, but with different slopes.

These calibration curves are rather heavily energy-dependent. For practical purposes, the spectrum of the radiation leaving a patient and arriving at a given detector is not easy to determine. To study this difficulty, we measured the detector response for a given X-ray spectrum applying different filters at the source and obtained the lines shown in figure 5.13.

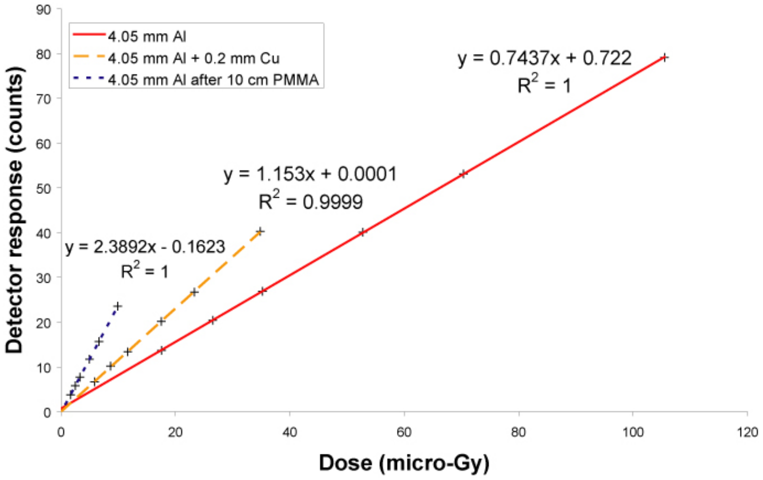

Figure 5.13: Dependence of detector response on the filtration. Example for detector No. 7, measured in 1 s.

5.3.2 Homogenization factors

The procedure described here is an attempt to homogenize the relative detector responses experimentally. We used this idea for the first measurements, and it might be useful in the future. Nevertheless, we have not used it in the rest of this work because it proved unnecessary once a normalization a-posteriori is carried out, as explained later in section 6.1.1.

If we define $S_{v,i}$ as the inverse of the slope obtained in figure 5.12 for the detector i at the incident photon spectrum corresponding to v kVp, we can obtain a homogenization factor by defining

$$F_{v,i} := \frac{S_{v,i}}{\overline{S_v}}, \; v = [50, 70, 90, 110], \tag{5.1}$$

where

$$\overline{S_v} = \frac{\sum_{i=1}^{198} S_{v,i}}{198}. \tag{5.2}$$

The factors $F_{50,i}$, $F_{70,i}$, $F_{90,i}$ and $F_{110,i}$ are only slightly energy-dependent (see table 5.2). They cannot be used to estimate the dose anymore, but they take into account to some degree the relative relation among the detectors. This information is required to carry out a correct reconstruction. For the detector number i, the mean correction factor that will improve its interpretation of the reading is given by

$$F_i = \frac{1}{4}\left(F_{50,i} + F_{70,i} + F_{90,i} + F_{110,i}\right). \tag{5.3}$$

An example of this process for the first 5 detectors is given in table 5.2. You can observe that the slopes S are very dependent on the energy spectrum, but the F-factors are not.

The sum distributions of the slopes S and the F-factors obtained for all detectors are shown in figure 5.14.

However, as stated at the end of last section, these factors were only used for the first measurement. Afterwards, they were substituted by a normalization a posteriori (section 6.1.1).

Table 5.2: Calculation of the correction factor for the first 5 detectors.

	S_{50}	S_{70}	S_{90}	S_{110}	F_{50}	F_{70}	F_{90}	F_{110}	F
Detector No. 1	0.440	0.268	0.190	0.157	0.998	0.948	1.009	1.005	**0.990**
Detector No. 2	0.407	0.245	0.174	0.144	0.922	0.867	0.923	0.919	**0.908**
Detector No. 3	0.471	0.285	0.203	0.169	1.068	1.009	1.078	1.082	**1.059**
Detector No. 4	0.377	0.227	0.162	0.134	0.854	0.806	0.859	0.859	**0.844**
Detector No. 5	0.362	0.218	0.155	0.129	0.821	0.772	0.824	0.827	**0.811**
$\overline{S}_{ofall197}$	0.441	0.282	0.188	0.156					

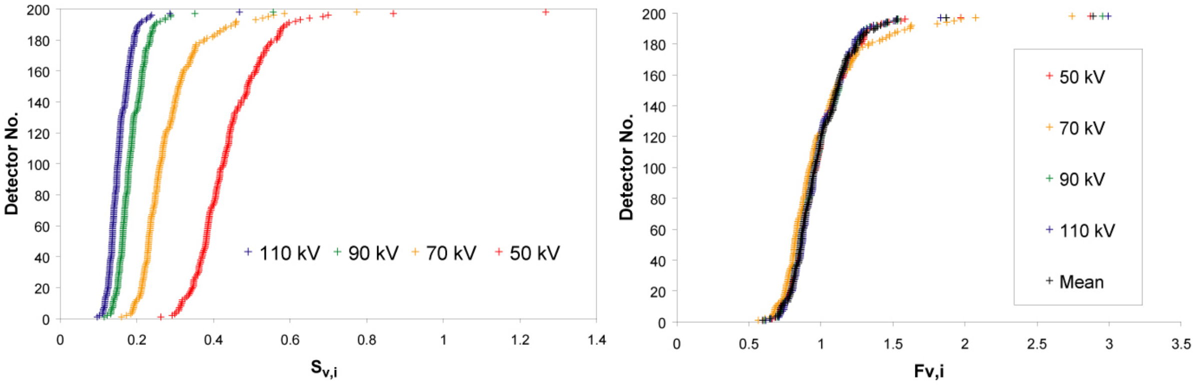

Figure 5.14: The sum distributions of the slopes $S_{v,i}$ obtained for all photon energy-spectra and all detectors (left) and the sum distribution of the corresponding F-factors, $F_{v,i}$ and their mean F_i.

5.3.3 Data acquisition

The constructed mask was mounted on a rotation desk and the whole assemble was placed in front of a Philips X-ray tube MCN 323 (Eindhoven, the Netherlands, its technical details can be found in the appendix), as shown in figure 5.15. The field of radiation of the source was collimated by a square slit, thus providing a maximum fan angle of 8 degrees. Therefore, the irradiated circular region in the centre of the device at the chosen distance to the focal spot has the radius indicated in Table 5.3.

In order to emulate a continuous rotation, the ring was set to rotate 3600 times in small steps of 0.1°. An exposure time of 2 seconds between two consecutive rotation steps was included to increase the amount of photons received by the detectors. Hence there are 7200 samples of 1 s for each detector during one whole cycle, which thus took 2 hours.

All measurements were carried out at a tube-voltage of 96 kV, current of 9.6 mA, the generally used filtration of 4.05 mm Al, a focal spot of 1.2 mm and an anode angle of 22°. The rest of the parameters of the measurements are shown in Table 5.3. The X-ray spectrum is shown in Figure 5.16.

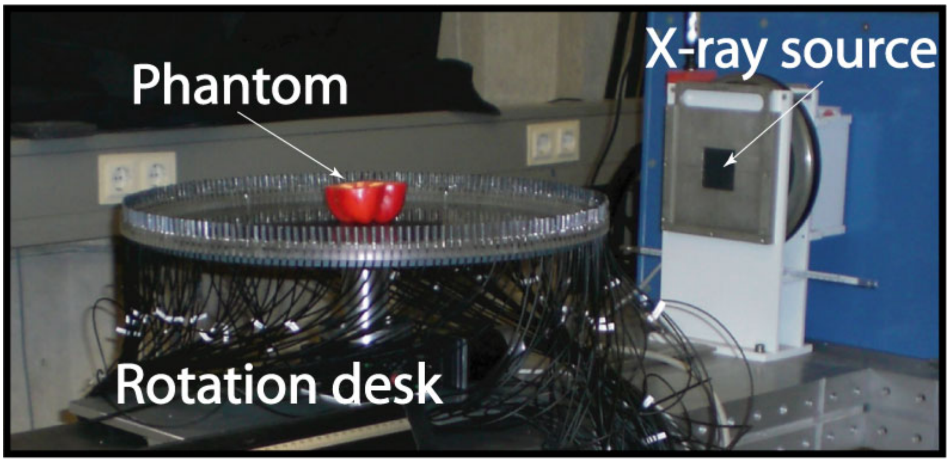

Figure 5.15: The constructed mask in the Secondary Standard Dosimetry Laboratory.

Table 5.3: Parameters of the measurements using the first set-up (in the GSF).

Phantom	Distance Focus-centre (± 0.5 cm)	Radius of Field of View (± 0.1 cm)
Red pepper	100.0	7.0
Tantalum Film	155.0	10.8
Nuts and corks	155.0	10.8
Three peppers	149.5	10.4
PMMA Semicircle	100.0	7.0

5.3.4 Empty scan

The Radon data $\mathfrak{R}_i$ needed for the reconstruction can be obtained as the logarithm of the intensity I_0 provided by the source at the situation of the detectors, divided by the intensity I_i received at the detector "i" (see Figure 5.17),

$$\mathfrak{R}_i := log\left(\frac{I_0}{I_i}\right). \tag{5.4}$$

The radiation received by each detector in our device is slightly affected by the different dimensions of the shielding elements and the windows. Therefore, to calculate the Radon data one has to obtain the corresponding intensities $I_{0,i}$ in each detector during an empty scan (without any phantom), and then calculate the individual Radon data as

$$\mathfrak{R}_i := log\left(\frac{I_{0,i}}{I_i}\right). \tag{5.5}$$

In the cases where no empty scan was carried out, the value of I_0 was estimated as the maximum intensity received in the detectors, i.e. during the moments that they are receiving direct radiation, that is

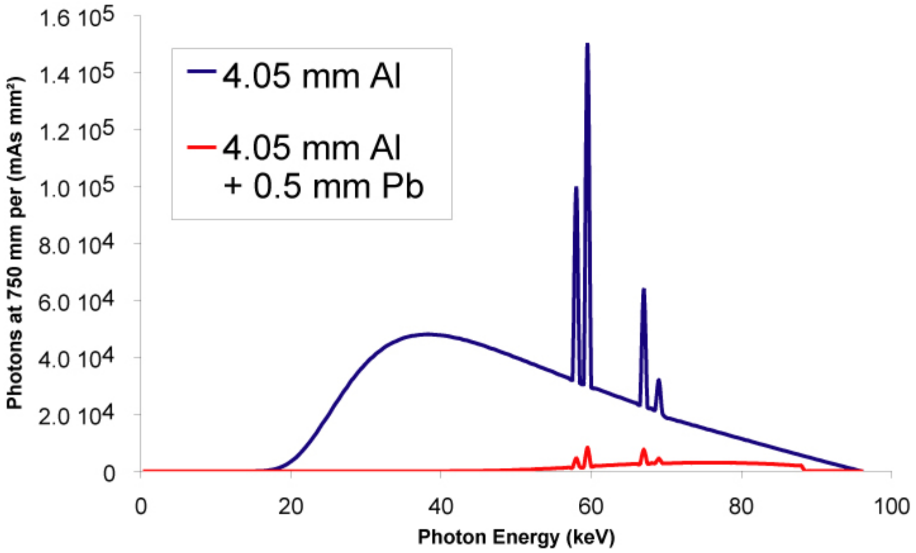

Figure 5.16: **Radiation spectrum for the measurements in the SSDL** corresponding to 96 kVp, attenuated by 4.05 mm Al and with an anode angle of 22°. The red curve corresponds to a filtered spectrum with 0.5 mm Pb. Data provided by [IPEM 97].

$$\mathfrak{R}_i := log\left(\frac{max(I_i)}{I_i}\right). \tag{5.6}$$

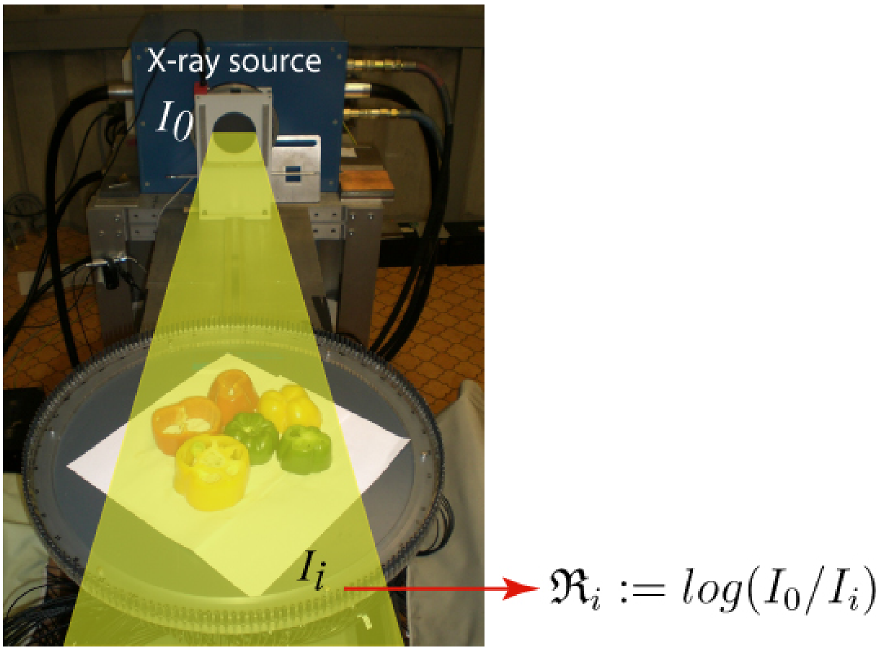

Figure 5.17: Set-up during the measurement with the last organic phantom. The formula in equation 5.4 is exemplified here for clarity.

5.4 Second experimental set-up

Once we had ensured functioning of the mask, we took the test-device to the Institute of Diagnostic Radiology at the Technical University Hospital Rechts der Isar to use one of their clinical devices. The set-up is shown in figure 5.18.

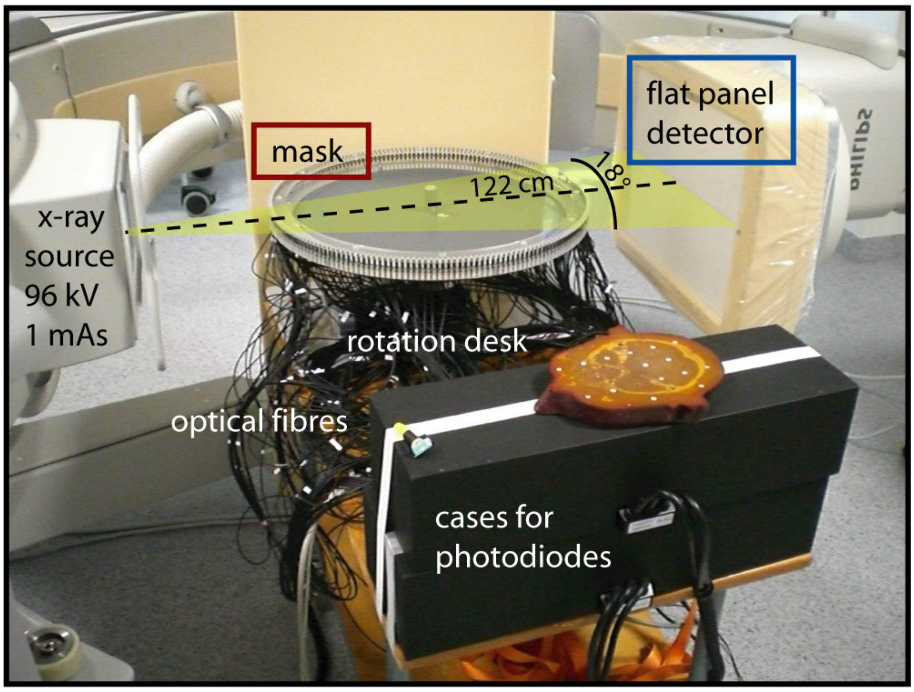

Figure 5.18: **The experimental set-up** during the alignment tests. The phantom used in the measurements can be seen in the foreground (and more closely in figure 5.8).

The main difference between this second set-up and the first one is the use of a clinical C-arm ELEVA Multidiagnost from Philips Healthcare (Eindhoven, the Netherlands). Therefore, the C-arm enables higher radiation intensity and the acquisition of a second, independent and complementary sinogram (as described in section 2.1.2). This device will be described therefore in first place. Afterwards, the conformance calibration and the alignment of both detector sets, as well as the data acquisition process will be explained.

5.4.1 Clinical C-arm device

The main two parts of the C-arm device are the pulsed source at one end of the "C", and the flat detector at the opposite side. C-arms are typically used for interventional radiology, but they are also being tested for CT applications in recent research (see e.g. [Orth 08]).

Pulsed source

The most significant difference with the first set-up is that this source provides pulsed instead of continuous radiation. The clinical devices providing continuous radiation and available did not work with digital data. Therefore, it would have been impossible to export the images and analyze them outside with a computer. However, we solved this pulsing difficulty using an appropriate sample time (see figure 5.19); the sample-time in the mask detectors is such that it is not possible to have two pulses in a single sample. The opposite case of one pulse being separated in two samples is harmless because those pulses can be easily added to recover the information. Nevertheless, very small sample duration would have made the size of the files impractical. So, we had to find the compromise shown in figure 5.19.

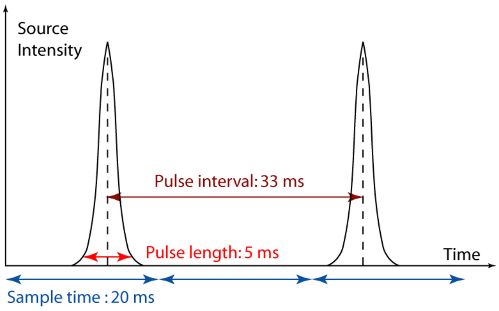

Figure 5.19: Intensity from the pulsed source. The beginning and the end of each sample is indicated with blue arrows.

Flat panel detector

The flat panel was used to simulate the arc-detector described in the theory of CT D'OR in chapter 2. However, for our case, we only need one row of the flat panel to reconstruct our 2-D slice (see discussion about the slice width in next section). The pixels of the flat panel detector are averaged into a single element of the produced image. Afterwards, the images are stored in the header of the device, which uses DICOM (Digital Imaging and Communications in Medicine) format, and they can be saved in the PACS (Picture Archiving and Communication System) of the hospital. The dimensions of the flat detector and of the resulting DICOM image are indicated in Figure 5.20.

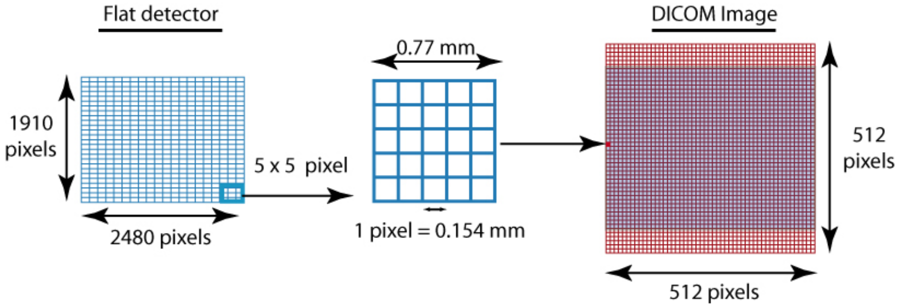

Figure 5.20: Dimensions of the flat panel detector, its pixels and the corresponding DICOM images used in this work.

5.4.2 The slice width

The slice width in the reconstructions from this set-up is determined by the following factors:

1. The vertical extension of the scintillator crystals in the mask, which is 1 mm.
2. The size of an image pixel k, which is given by

$$k = 0.154 \left(\frac{\text{mm}}{\text{detector pixel}} \right) \times 4.84 \left(\frac{\text{detector pixel}}{\text{image pixel}} \right) = 0.75 \left(\frac{\text{mm}}{\text{image pixel}} \right), \quad (5.7)$$

   where the factor 4.84 is the quotient of the size of a raw image in the flat detector (2480 x 2480) and the size of a DICOM stored image (512 x 512). The stored images are squares, although the flat panel receives data in a surface area of size 2480 x 1910 pixels.
3. The thickness of the slice where all scintillators crystals are found, which has been measured using the images shown in figure 5.21. Since small parts of some crystals can be seen over and below the grayed row, the width of the slice where all scintillators lie can be given as 1.2 ± 0.4 mm.
4. The vertical alignment of the focal spot of the X-ray source with the plane of the scintillator crystals. This factor does not contribute to a further error in the slice width, because the alignment of the front and back rows of scintillators in the image (moving the C-arm up and down) ensures that the focal spot is also aligned with them. Otherwise, one would observe both rows of crystals at different heights.

5.4.3 Conformance of both detector sets

In order to conform the measurements with the flat panel, simulating the arc-detector, and the ones with the mask detectors, it is necessary a calibration of both detector sets together, as well as an alignment of the center of the ring with the center of the flat panel.

Calibration

Since both sets of detector elements are of very different physical nature, it is necessary to carry out a calibration to homogenize their computed response at a given radiation dose.

For the conformance calibration, we carried out two empty scans: one in the same way as in the first set-up, and one using an additional filter of 0.1 mm Cu and 1 mm Al. The filter, collocated directly at the source, ensures that all detectors receive the same radiation quality. The additional filter was introduced to simulate to some degree the modification of the incident photon spectrum by the inelastic scattering processes in a scanned object. This modification is strongly energy dependent in this energy range (E $\simeq$ 100 keV) because of the photoeffect scattering and its $1/E^3$ dependence [Krane 88].

It is assumed that every detector-response is linear with the received radiation intensity, as checked for the mask detectors in section 5.3.1. The reading of each detector i during the empty scan was assigned a value $R_{e,i}$, and the reading during the scan with the additionally filtered radiation was assigned the value $R_{f,i}$. The conformance calibration consists in correcting each reading R_i during the phantom scan through

$$I_i := \frac{R_i}{R_{e,i} - R_{f,i}} + b_i, \quad (5.8)$$

where the background b_i was measured doing ten measurements without any radiation and subtracting their mean from all detector readings. This correction ensures that the values I_i are in the same range for every detector, because they take into account the response of the detector to two different spectra by the inclusion of $R_{e,i} - R_{f,i}$.

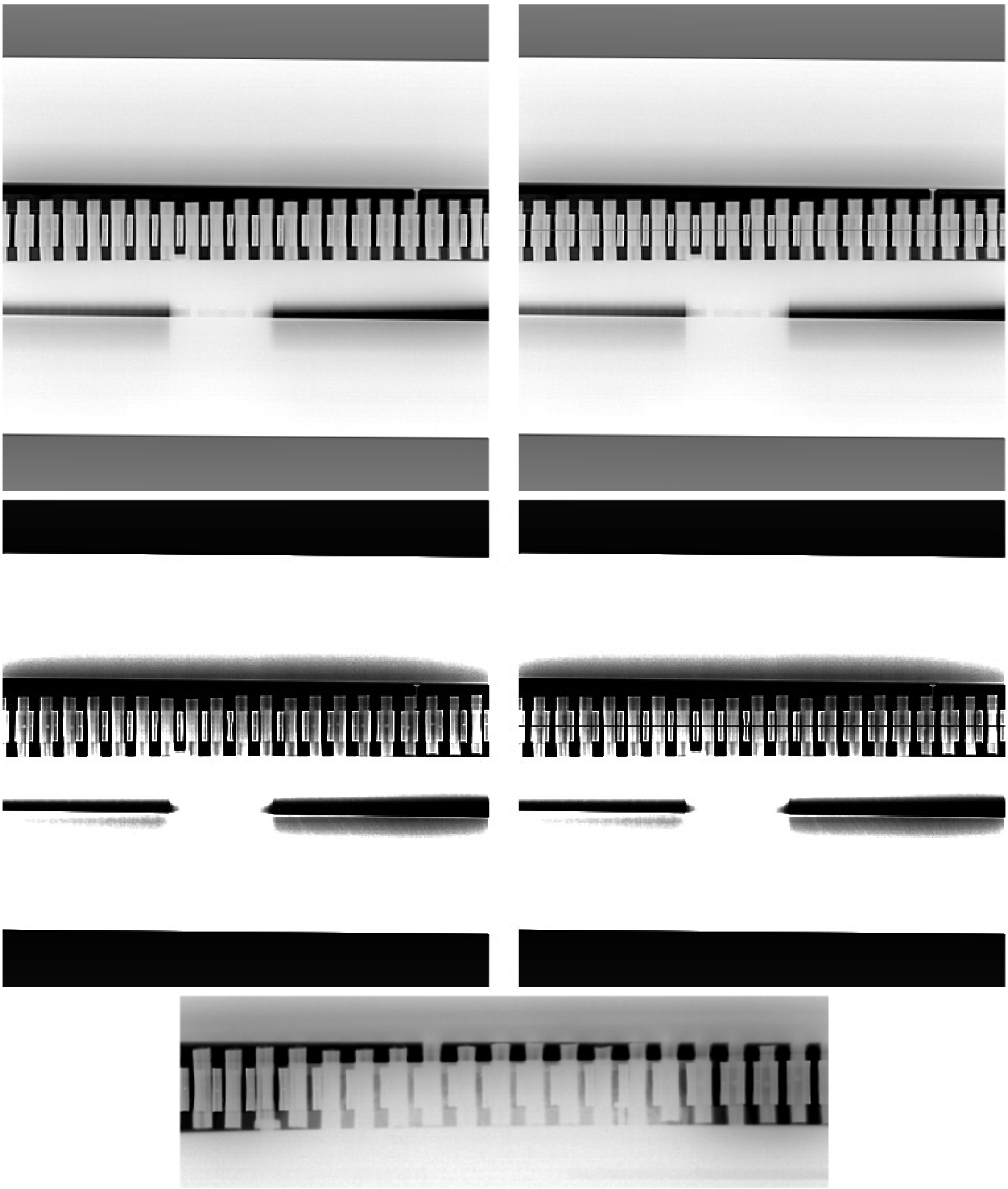

Figure 5.21: **Top left**: An example of a raw DICOM image acquired by the flat panel detector during an empty scan. **Top right**: The same image showing in gray its row number 237, where all mask-scintillators lie almost completely. The thickness of this line is one pixel, which corresponds to 0.75 mm following equation 5.7. The same images have been processed below to show the crystals more clearly. **Bottom**: An example of an image acquired during a phantom scan (only the relevant region).

Alignment

The flat panel and the mask need to be aligned before the measurements, so that the central ray, marked with a dashed line in figure 5.18, enters the ring through a window and exits the ring through a detector, arriving at the flat panel detector approximately in the middle. Three metal nails were used to distinguish the two detectors forming the window at the entrance, say No. 151 and No. 152, and the detector directly in the opposite side, detector No. 53.

The first step of the alignment was to acquire images to check that detector 53 is seen between detectors 151 and 152. An object in the middle of the mask would then also be seen between the two front nails. But this does not ensure that the central ray is passing through the center of rotation. To check the alignment of the central ray with the middle of the mask, we placed a 2 cm-wide cylinder of aluminium in the middle of the mask (± 1 mm) and recorded a fluoroscopy series of images during a mask-rotation of 180°. Were the central ray not irradiating the cylinder, then this cylinder would move significantly during the rotation and we would shift the table towards the correct middle. On the contrary, if the cylinder moved less than the width of one window during that rotation, then the alignment was correct. One recorded series proving a correct alignment of the set-up can be found in the CD attached to this thesis.

5.4.4 Data acquisition

The clinical X-ray source is not prepared for long periods of irradiation. So we had to carry out a scan of 360 degrees in series of 30 degrees, stopping for about 5 minutes after every two or three series to permit cooling of the source. One whole scan took about 45 minutes[6]. We used a photon energy quality of 96 kV, the intrinsic filtration of the device (0.1 mm Cu and 1 mm Al) and an average current of 1 mAs (since the x-ray pulses have a duration of 5 ms approximately, the intensity in every pulse was 200 mA). The corresponding X-ray spectrum is very similar to the one shown in 5.16. The rest of the parameters of each measurement are shown in table 5.4. In the second measurement with the head slice, we used by mistake images that had been processed by the C-arm's software instead of the raw data, as shown in the table. The effect of this is noted in the data, but the reconstruction does not look significantly affected. The data of the two last measurements were not analyzed in the present work. Therefore, their parameters are not included in the table.

Table 5.4: Parameters of the measurements in the Clinic.

Phantom	Distance Focus-centre (± 0.5 cm)	Distance source-FD (± 0.1 cm)	Raw data
Head slice	76.0	122.0	yes
Head slice & empty scan	74.0	122.0	no
Tantalum Film	–	-	yes
Calibration	–	-	yes

---

[6] The device for projection radiography Kodak DirectView 7100 (Carestream Health, Inc., Rochester, NY), acquired recently by HMGU, also uses pulses of radiation, but it could help to make a very exact scan, because it includes a flat detector, lasers to align the device very precisely and a proper software. Nevertheless, previous attempts have shown that it would take days of continuous work to complete a full scan, because images are recorded at a maximum speed of one per 45 seconds.

Chapter 6

Data Treatment

The process of converting the raw experimental data from the demonstrator into a sinogram that can be used for image reconstruction needed a lot of effort. Each step in the theory of CT D'OR and each experimental deviation from it implied calculations. These were carried out with the help of programs written in Interactive Data Language (IDL, ITT Visual Information Solutions, Boulder, USA).

In section 6.1, the data treatment of the separate sets of mask-data and arc-data is presented and exemplified with one selected measurement. Afterwards, section 6.2 describes the data treatment to obtain the complete sinogram. At the end, section 6.3 presents a brief description of the codes for the OPED reconstruction algorithm. The names of the corresponding IDL programs are referenced in `type writer font` after the explanation of each step all along this chapter, and all the codes are included in the attached CD.

6.1 Operations needed for each data set

This section describes the processes needed to obtain the independent sinograms and the independent reconstructions (figure 6.1), as well as the process of joining both sets of data into the complete sinogram for the final image reconstruction (figure 6.4). Some of these steps are the same as the ones operated on data from conventional technologies [Hsieh 03].

6.1.1 Data from the mask detectors

The processes operating on the mask-detectors data is exemplified in figure 6.2 and described below.

Cut - All measurements during which the rotation desk was standing still, as well as the measurements corresponding to the port number 198 were cut away of the matrix because they are useless. The raw data are thus transformed in a measurement corresponding to exactly 360°-data. At the same time, the data corresponding to positions of the detectors between the phantom and the source were set to zero. Observe that these data (thick band in the matrix of raw data) are missing after the Cut. It may be necessary to check the image `06-Treatment1.pdf` in the attached CD.

Peak integration - The temporal evolution of every single detector shows peaks corresponding to the moments during which it was receiving full or partially shielded radiation (as explained in the theory of CT D'OR in figure 2.2 and as obtained experimentally in figure 7.12). These peaks were integrated independently and sent to a separate matrix

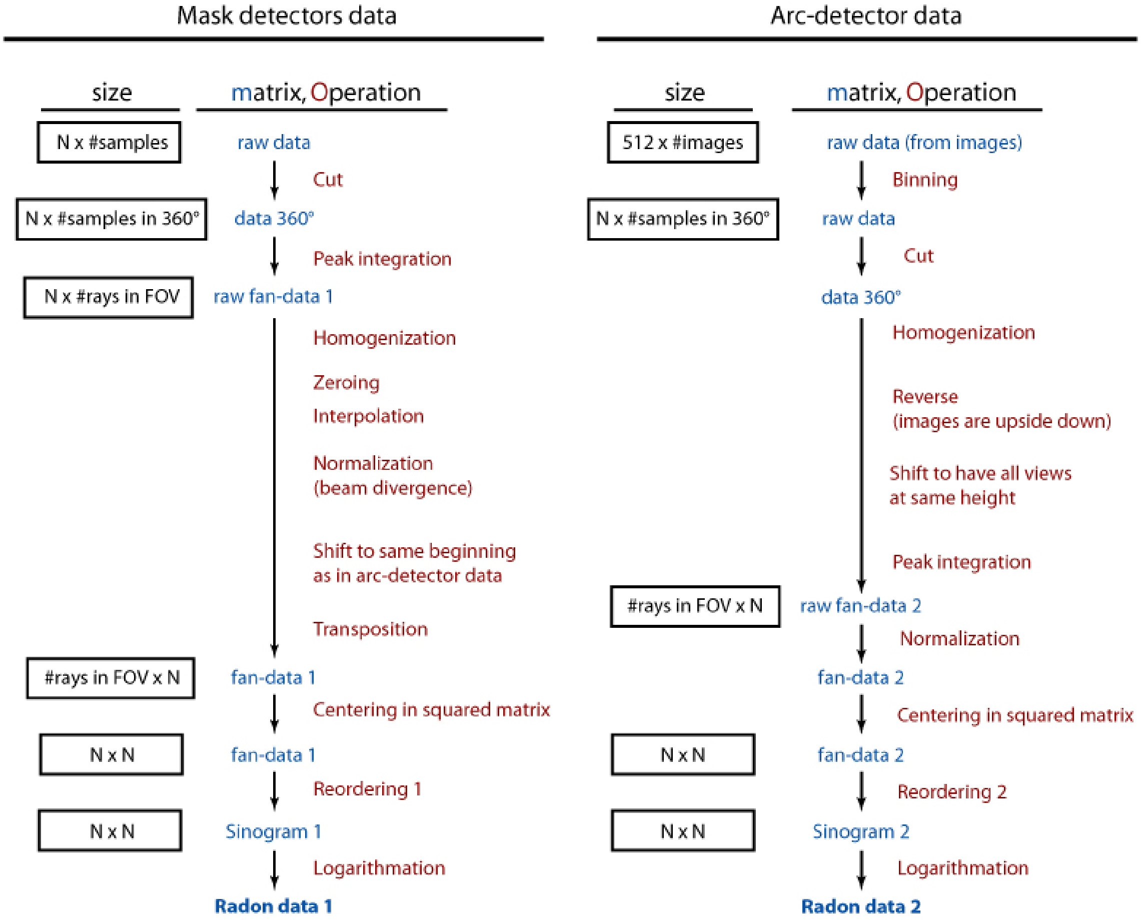
Mask detectors data
size
matrix, Operation
N x #samples
raw data
Cut
N x #samples in 360°
data 360°
Peak integration
N x #rays in FOV
raw fan-data 1
Homogenization
Zeroing
Interpolation
Normalization
(beam divergence)
Shift to same beginning
as in arc-detector data
Transposition
#rays in FOV x N
fan-data 1
Centering in squared matrix
N x N
fan-data 1
Reordering 1
N x N
Sinogram 1
Logarithmation
Radon data 1
Arc-detector data
size
matrix, Operation
512 x #images
raw data (from images)
Binning
N x #samples in 360°
raw data
Cut
data 360°
Homogenization
Reverse
(images are upside down)
Shift to have all views
at same height
Peak integration
#rays in FOV x N
raw fan-data 2
Normalization
fan-data 2
Centering in squared matrix
N x N
fan-data 2
Reordering 2
N x N
Sinogram 2
Logarithmation
Radon data 2

Figure 6.1: The schema of the data processing for each kind of data separately. N represents the number of detectors in the mask (N = 197). FOV means Field of View.

of fan-data. This matrix has a size of 197 detectors x 61 data per detector in the example of figure 6.2. This "61" is the number of rays inside a fan-view, which equals the number of mask detectors inside the radiation beam in a single moment.

The previous steps are included in the IDL programs `mustering1_find.pro` and `muster_1.pro`. The first program needs the distance d_{CF} from the center of the mask to the focal spot as input value. This is usually very difficult to measure with precision, because the focal spot is inside the X-ray apparatus, which cannot be opened. Therefore, the program tries values of d_{CF} with high precision around the input value until it finds the optimal distance. This optimal value is characterized by the best match of the experimental peaks and their calculated distribution, which is dependent on that distance. The patterns for that distribution are generated by `muster_1.pro`, taking into account that the peaks are found in the positions

$$p_i = \psi_i + \arccos(r \cos \psi_i), \tag{6.1}$$

where r is the radius of the mask expressed as a fraction of d_{CF}, and the angles ψ_i are given by the lengths of the shielding elements, detectors and windows, as detailed in [Tischenko 08].

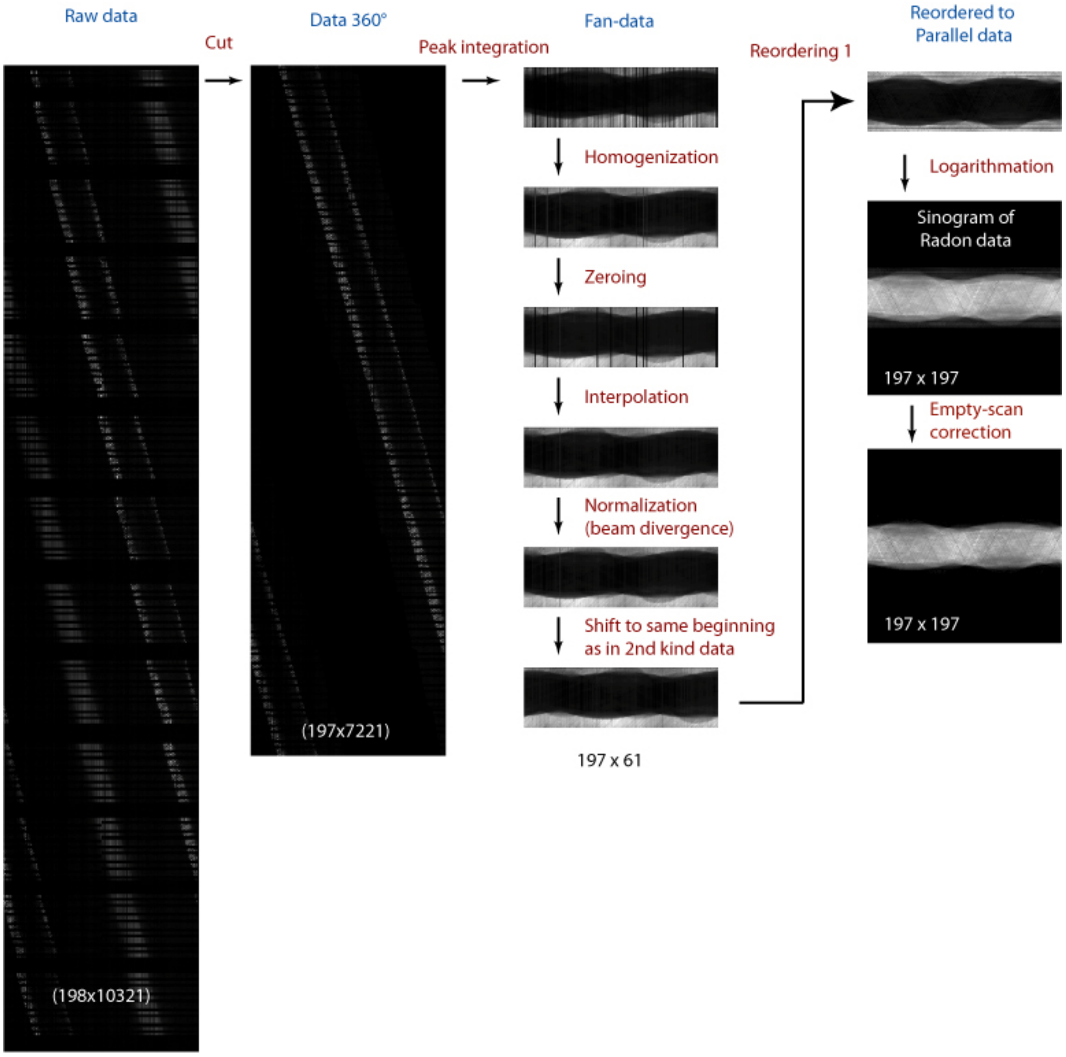
Raw data
Cut
Data 360°
Peak integration
Fan-data
Reordering 1
Reordered to Parallel data
Homogenization
Zeroing
Interpolation
Normalization (beam divergence)
Shift to same beginning as in 2nd kind data
Logarithmation
Sinogram of Radon data
Empty-scan correction
(198x10321)
(197x7221)
197 x 61
197 x 197
197 x 197

Figure 6.2: Matrices obtained during the treatment of the mask-detectors data from the measurement with the device at the hospital Rechts der Isar of TUM. The first two matrices have their dimensions expressed in brackets because their size has been reduced to fit in the figure.

Homogenization - The calculation of the homogenized matrix N from the integrated matrix I ignores all zero elements. The non-zero elements $I_{i,j}$ are transformed as

$$N_{i,j} = I_{i,j}\frac{m}{M_j}, \tag{6.2}$$

where m is the maximum value of the vector M, whose j^{th} element M_j is the mean value of the non-zero data from detector j.

This homogenization circumvents the need of an energy calibration of the detectors, which is impossible for practical reasons[1]. Due to the high energy-dependence of the detectors responses, this correction “a posteriori” produces a better homogenization of the detectors response than the experimental calibration described previously in section 5.3.1.

---

[1] It would be necessary to measure the spectrum of the radiation arriving at each single detector in each moment to apply the corresponding calibration factor.

Zeroing - Around 5 % of the detectors showed a response that was not in concordance with the rest (either because they were torn apart during the measurement or because they showed a too low signal). These “outliers” were therefore set to zero and their measurements were substituted by interpolation.

Interpolation - A 1-dimensional cubic spline along every row, containing data at a constant distance to the centre as in figure 4.7, was used to fill in the few empty cells of data through interpolation.

Normalization - A normalization due to beam-divergence was carried out at this stage. The influence of it is, however, very small, because the divergence of the beam is very small in comparison to the distance from the detectors to the source. The vertical divergence is only 0.04 %, and the horizontal divergence is 5 %. Both percentages imply unnoticeable differences in the normalization factors [Tischenko 08].

Shift - The fan-data of the mask detectors are not acquired in the same sequence as the fan-data of the arc-detectors. Therefore, these mask data were shifted to begin at the same point as the arc data.

Reorder - The data acquired with this fan geometry can be transformed into data of a parallel geometry by simple reordering, as explained in section 2.2.1.

Logarithmation - The matrix of Radon Data $\mathfrak{R}$ was finally obtained from the interpolated matrix of parallel data P by

$$\mathfrak{R}_{i,j} = \ln\left(\frac{\max(P_{i,j})}{P_{i,j}}\right). \tag{6.3}$$

All these steps are included in the program `sinogmus.pro`, which includes a list of initial values in the beginning for the different phantom data that have been acquired in this work.

If the data from the empty-scan P^e are taken into account, the Radon data are more rigorous when they are calculated as

$$\mathfrak{R}_{i,j} = \ln\left(\frac{P^e_{i,j})}{P_{i,j}}\right). \tag{6.4}$$

IDL Program: `aircorr2.pro`.

6.1.2 Data from the flat panel detector

The processes operated on the data of the flat panel detector is exemplified in figure 6.3 and described below.

The initial matrix of raw data contains no black rows because the flat detector acquires data only when the source irradiates it. However, the beginning and the end of the measurement contain repetitive data that must be cut to one exact rotation of 360°.

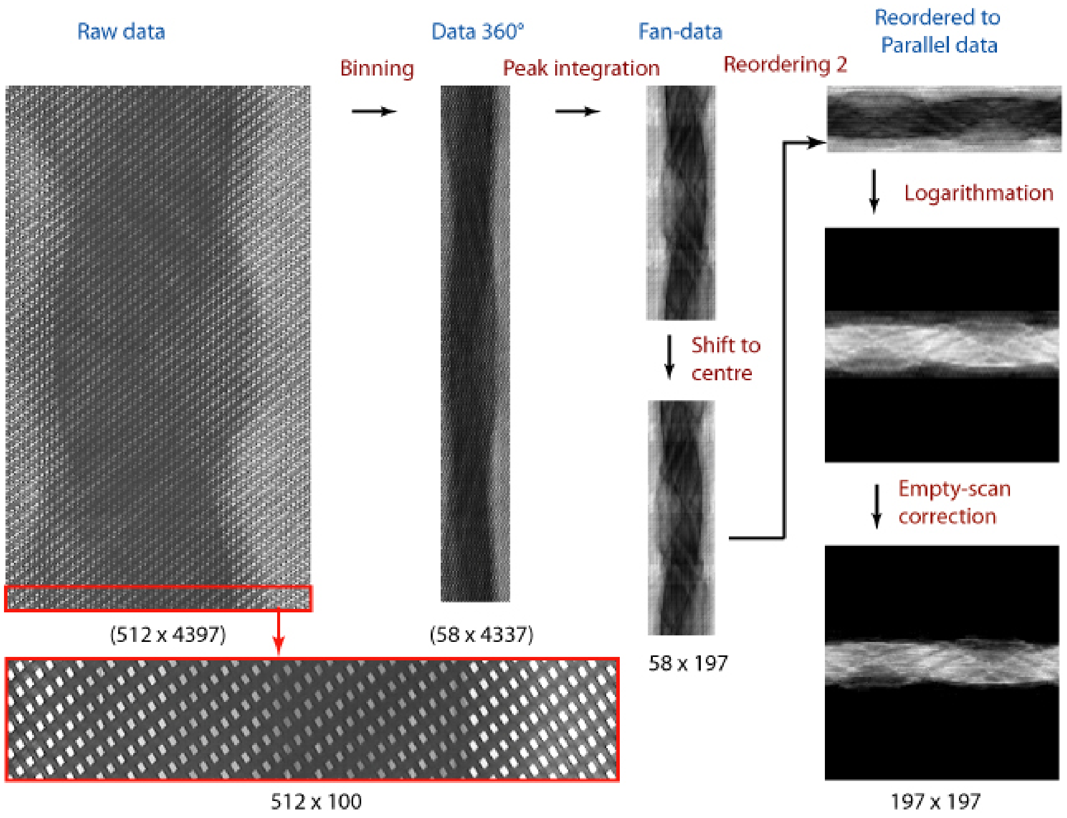
Raw data
Binning
Data 360°
Peak integration
Fan-data
Reordering 2
Reordered to Parallel data
Logarithmation
Shift to centre
Empty-scan correction
(512 x 4397)
(58 x 4337)
58 x 197
512 x 100
197 x 197

Figure 6.3: Matrices obtained during the treatment of the gantry-data for the same measurement as the one shown in figure 6.2.

The size of this matrix is 512 pixels in the DICOM image x 4397 pulses acquired in 365°.

IDL Program: `checkdata.pro`.

Binning - The process of binning corresponds to integrating the signals of all instances during which one bin receives radiation belonging to one full stripe like the ones shown in figure 2.3. Care must be taken to integrate only the rhombic regions of data, seen in the magnified portion of the matrix at the bottom of figure 6.3, and not the background signal surrounding them. In the example shown in Figure 6.3, the 360°-data matrix obtained has a size of 58 (bins illuminated by the fan) x 4337 (pulses acquired in 360°).

IDL Programs: `binmuster2.pro` and keyword `/plus` inside program `sinogclin.pro` (or alternatively the program `sinogclin2.pro`).

Integration - As in the mask-data, the temporal evolution of every single flat panel detector-bin shows peaks corresponding to the instances in time during which it was receiving direct radiation (theoretically explained in figure 2.2 and shown experimentally in figure 7.12). These peaks were again integrated independently and sent to a separate matrix of fan-data. In this case, the peaks are equidistantly distributed, because they represent the same ray of all views as explained in section 2.1.2.

The resulting matrix in figure 6.3 has a size of 58 (bins or rays per fan) x 197 (rays detected in each bin - or number of fans). If you compare this matrix with the fan data obtained in last section, there is a lower amount of rays per fan in these arc data (58) as in the mask data (61). This is due to the asymmetric form of the fan, which was wider on one side as on the other side of the source. In order to keep symmetry in the data, we kept an equal number of bins on each side of the central ray.

IDL Programs: `mustering2.pro, muster_eq.pro` (or alternatively the program `sinogclin2.pro`, which uses the subroutine `binpix.pro`).

Shift to centre - Again due to the asymmetry of the fan, we had to shift the arc data three columns to the left in the example shown in figure 6.3, so that the data are centered in the matrix.

The step of Reorder and the interpolation of the missing 50 % of data are carried out by the IDL programs `reorder2.pro` and `intwtw.pro` (or alternatively the program `sinogclin2.pro`, which makes use of the subroutine `interpolating.pro`).

The steps of logarithmation and empty scan correction are the same as in the mask data.

All these steps and subprograms (except cut and binning) are included in the IDL programs `sinogclin.pro` and `aircorr2.pro`.

Note that in these data, there is no step of Homogenization, because the whole flat detector is already calibrated in the clinic regularly. Nevertheless, in the example of figure 6.3 one can observe regions of different brightness in the fan data matrix. The flat detector carries out different normalization procedures of the data every time it saves a different fluoroscopy series. This could have been avoided by saving the raw images, as we had done until then, instead of the processed ones, as we did in this case by mistake.

6.2 The data set merging into the full sinogram

The process followed to obtain the complete sinogram from the two sets of fan data is sketched with a flux diagram in figure 6.4, exemplified in figure 6.5 and described below.

Scaling - The arc data were scaled to have the same maximum as the mask data. However, the different physical nature of both detector sets poses serious problems to homogenize their responses (See discussion later in section 8.2.1).

Joining - The two sets of fan-data were joined to a $2N \times 2N$-matrix of fan-data, where N is the number of views, following the theory of CT D'OR (section 2.1). As expected, in the obtained matrix there is 1/4 of data missing, which correspond to virtual rays ranging from one detector to another (see section 2.1.2).

Reorder - The fan-data are then reordered to a sinogram of size $2N \times N$. Due to the special geometry of this sinogram, its appearance is not as smooth as the one of other sinograms, as can be seen in the enlarged portion.

Interpolation - The interpolation of the missing data can be carried out using 1-D splines or the 2-D methods described in section 4.4. For the simulation described in 3.1, the interpolation was done in the fan-data.

All these steps are carried out with the IDL program `reorder_fan2N.pro` .

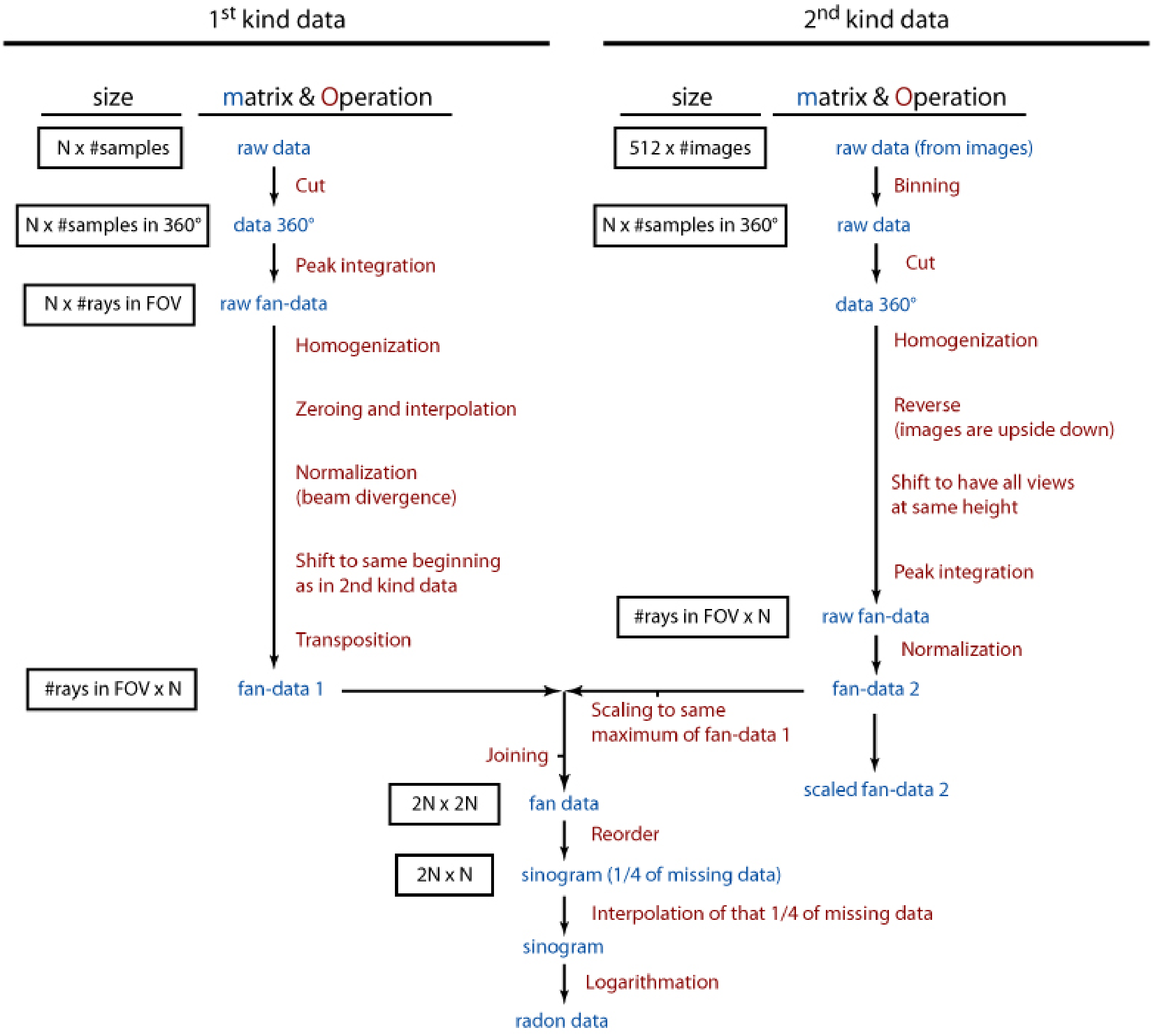
1st kind data
2nd kind data
size
matrix & Operation
N x #samples
raw data
Cut
N x #samples in 360°
data 360°
Peak integration
N x #rays in FOV
raw fan-data
Homogenization
Zeroing and interpolation
Normalization (beam divergence)
Shift to same beginning as in 2nd kind data
Transposition
#rays in FOV x N
fan-data 1
size
matrix & Operation
512 x #images
raw data (from images)
Binning
N x #samples in 360°
raw data
Cut
data 360°
Homogenization
Reverse (images are upside down)
Shift to have all views at same height
Peak integration
#rays in FOV x N
raw fan-data
Normalization
fan-data 2
Scaling to same maximum of fan-data 1
scaled fan-data 2
Joining
2N x 2N
fan data
Reorder
2N x N
sinogram (1/4 of missing data)
Interpolation of that 1/4 of missing data
sinogram
Logarithmation
radon data

Figure 6.4: The schema of data processing for joining both sets into the final sinogram.

6.3 The reconstruction code-program OPED

OPED for data of 1st and 2nd kind

This program was written in C using the standard routines FFTW3 [Frigo 06]. They only contain a small participation of myself in the second one - the first one was written by Yuan Xu and Oleg Tischenko completely.

OPED to reconstruct the final sinogram

The program `oped_hugo_z.pro` to reconstruct the final sinogram was written in IDL by the author of this work after the theoretical article of Tischenko, de las Heras, Xu and Hoeschen [Tischenko 08]. As described at the end of section 2.2.2, the steps followed in this program are:

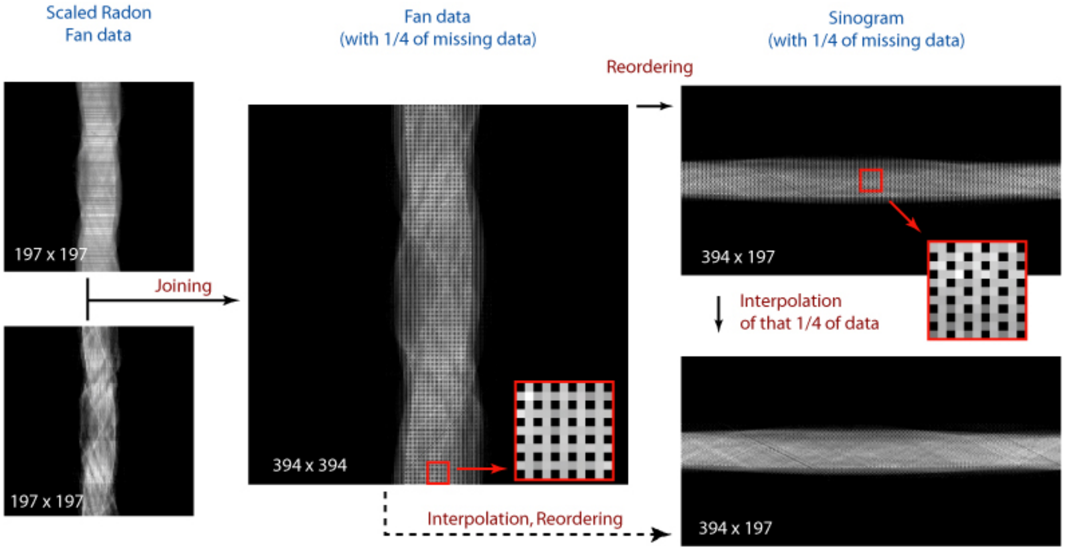
Scaled Radon
Fan data
197 x 197
197 x 197
Joining
Fan data
(with 1/4 of missing data)
394 x 394
Reordering
Sinogram
(with 1/4 of missing data)
394 x 197
Interpolation
of that 1/4 of data
394 x 197
Interpolation, Reordering

Figure 6.5: Matrices obtained during the process of joining both sinograms shown separately in figures 6.2 and 6.3. The possibility of interpolating the fan-data matrix and then reordering, marked with a dashed line, could have been easier because the coordinates of the interpolation grid are continuous in this case, as can be seen in the magnified matrix portions.

1 Calculate the matrix of $\lambda' s$ (see equation 2.14), which are the coefficients of the expansion in Chebyshev polynomials.

2 Calculate the Chebyshev polynomials in each point or matrix pixel (x, y) and the corresponding expansion in each point.

This program includes the possibility of reconstructing only a portion of the image (like a zoom, hence the “z” in the name).

Chapter 7

Results

The main result of this work is that the theory of CT D'OR is sound, because it has been possible to obtain reasonably good images using the two data sets independently, as well as to prove the complementarity of both sets. However, each test object has been useful to check a specific property of the demonstrator (see section 5.2), and that is why each single reconstruction is presented here separately. The description of results is divided into two sections:

7.1. The reconstructions obtained with the demonstrator using the first experimental set-up in the HMGU, where only the mask detectors where available.

7.2. The reconstructions obtained with the second set-up in the university hospital Rechts der Isar. In this case, reconstructions of the first and second kind of data sets are shown, as well as the reconstructions from the complete sinogram.

Each one of the reconstructions from the demonstrator are shown in the following sequence where relevant:

- a picture of the original phantom,
- the sinogram,
- the raw reconstruction as given by the OPED algorithm,
- the same reconstruction where all negative values have been set to zero.

The last element of this sequence is the meaningful one for image quality measurements and comparisons, because negative values in the reconstruction are only a by-product of polynomial expansions due to the Gibbs phenomenon (see section 2.2.5). However, the raw reconstruction is very convenient to observe the structure of artefacts.

Some features of the images need to be observed in a computer screen. In this cases, the name of the corresponding pdf file in the attached CD is given in the caption in `type writer text`.

7.1 Results from the first set-up

In the HMGU, we carried out scans of organic phantoms and the two plexiglas phantoms.

7.1.1 The first reconstruction: a pepper slice

As explained in section 5.2, we chose a pepper half for the first scan because it is organic, its structures are easy to recognise, it contains air regions (high contrast), and it presents a relatively low absorption to X-rays. Its low absorption properties made the data treatment faster (in a record time of 5 days), since the peaks were very easy to separate using a cut-off level (figure 7.1).

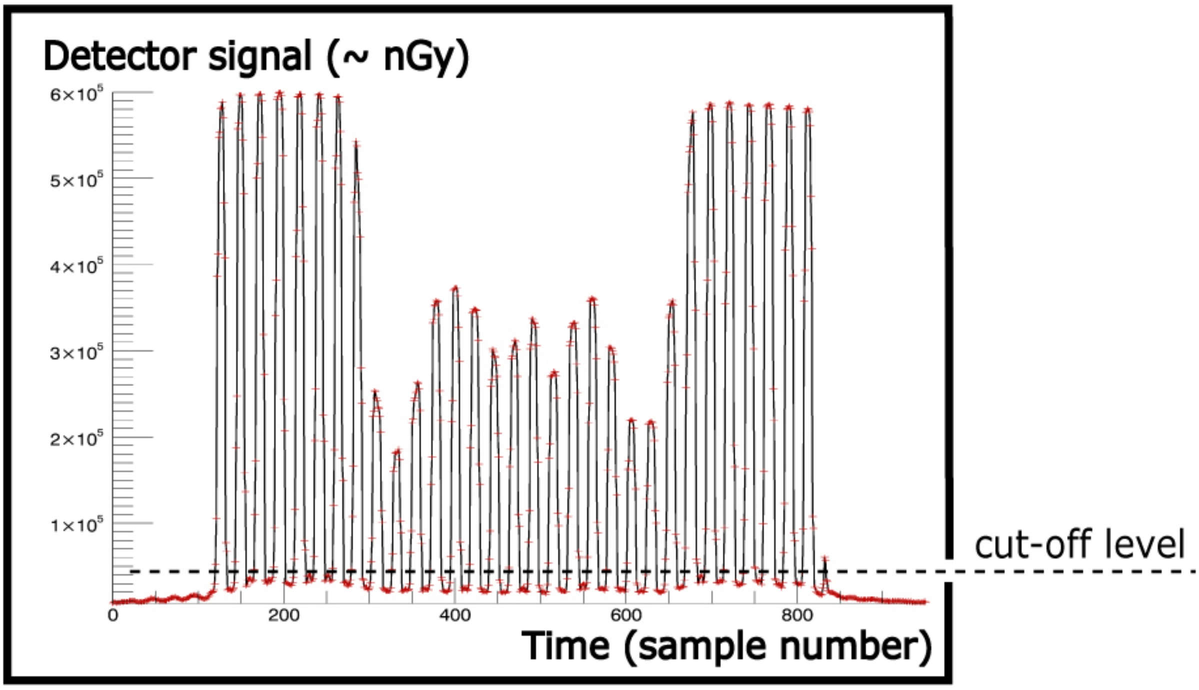

Figure 7.1: **The relevant raw data from detector number 1** during the scan of the half pepper. The largest peaks left and right correspond to instances of direct irradiation of the detector. The middle region informs of the phantom's structure. A common cut-off value can be set to separate all peaks from each other.

Following the process described in section 6.1.1, we constructed the sinogram and obtained the reconstruction shown in figure 7.2. Note that the contour of the pepper is doubled. This results from the incomplete rotation of the desk (explained in section 5.1.5), which we amended in the following reconstructions (see figure 7.8, for comparison).

The air regions, the four lobules of the pepper and the regions of higher density can be easily recognised in the reconstruction. This reconstruction is overall historical, because it was the first experimental proof that the idea of CT D'OR (using the new features of peak integration and rearrangement of fan-data without rebinning) can actually produce a reasonable reconstruction [de las Heras 07].

7.1.2 Other organic phantom reconstructions

a. The phantom made of nuts and corks in resin

The phantom made of nuts and corks in resin was the first proof that the demonstrator can image objects with large absorption too. It is not possible to find a cut-off value to separate

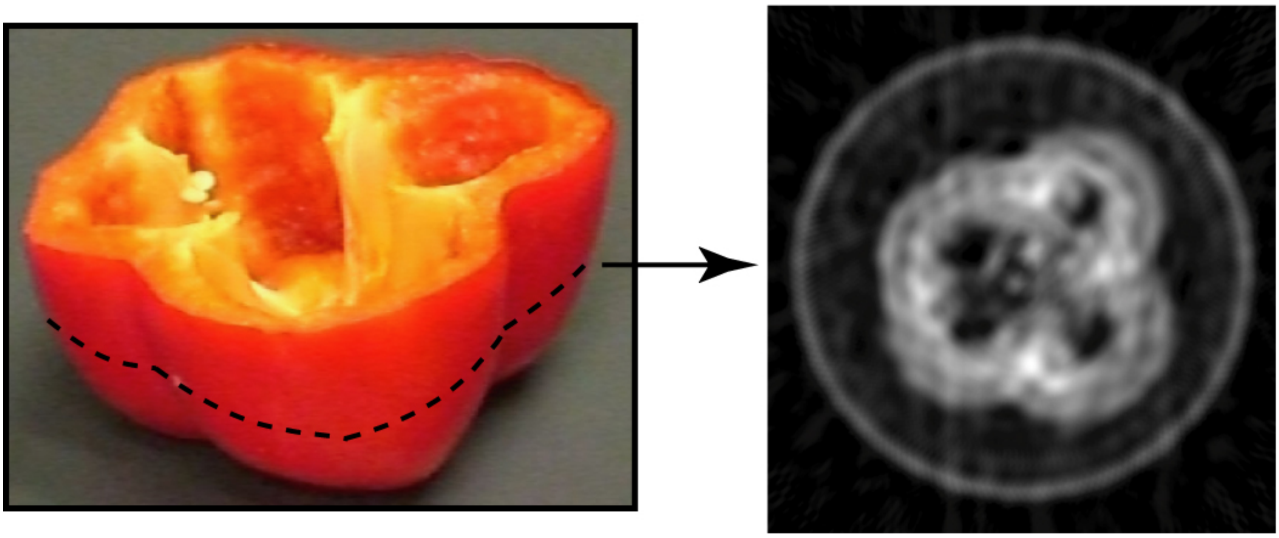

Figure 7.2: [`07-first_rec.pdf`] The first phantom and its reconstruction. The dashed line on the left figure indicates the height of the slice that was reconstructed.

the peaks of the raw data in this case because this phantom presents a much higher absorption, as it can be seen in the small peaks in the middle of figure 7.4. Therefore, it was necessary to use the calculated pattern presented in equation 6.1 to integrate the peaks, as described in section 6.1.1. Each data region where the pattern is non-zero is integrated into a single pixel of the fan-data matrix.

Following the process described in section 6.1.1, we can obtain the sinogram shown in figure 7.3 and the reconstruction shown in figure 7.5. The difference between the raw reconstruction and the image obtained by setting the negative values to zero can be observed only in the pdf-file contained in the attached CD: they are too subtle to be observed in this print.

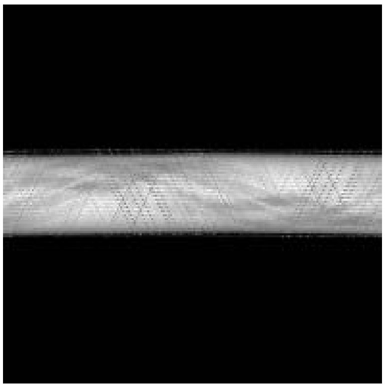

Figure 7.3: [`07-sresin.pdf`] **Sinogram from the resin phantom data**.

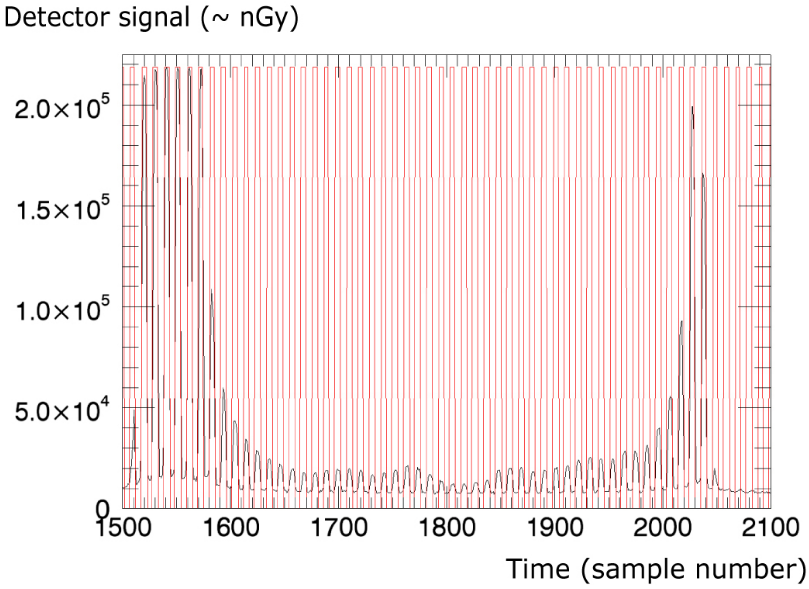

Figure 7.4: **In black: The relevant section of the raw data from one detector** during the measurement with the resin phantom. In **red**: **The calculated pattern from equation 6.1 for the peak distribution**: Observe that every data point contained in a peak is inside a region where the pattern function is non-zero.

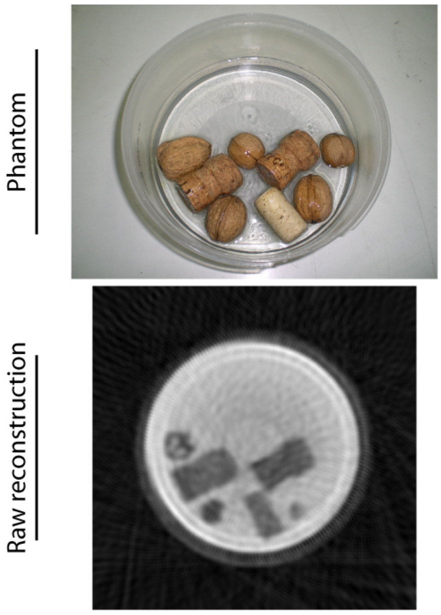

Figure 7.5: [`07-nutscorks.pdf`] The phantom made of nuts and corks in resin and its reconstruction.

This reconstruction shows the demonstrator's ability to obtain sensible data from objects with larger absorption than a pepper. Note that not all nuts and corks are at the same height, and therefore, the reconstruction of one slice cannot look exactly as the phantom does from above.

b. The phantom made up of six pepper slices

Before this phantom's scan, a previous empty scan (as described in section 5.3.4) was made. We chose peppers again for this reconstruction because of the previous successful experience and to correct the double structure resulting from a desk rotation of less than 360°. The distance to the source was increased (as indicated in Table 5.3) to obtain a larger field of view. Figure 7.6 shows the data for the phantom scan and the empty scan together. The obtained sinogram and the corrected one are shown in figure 7.7.

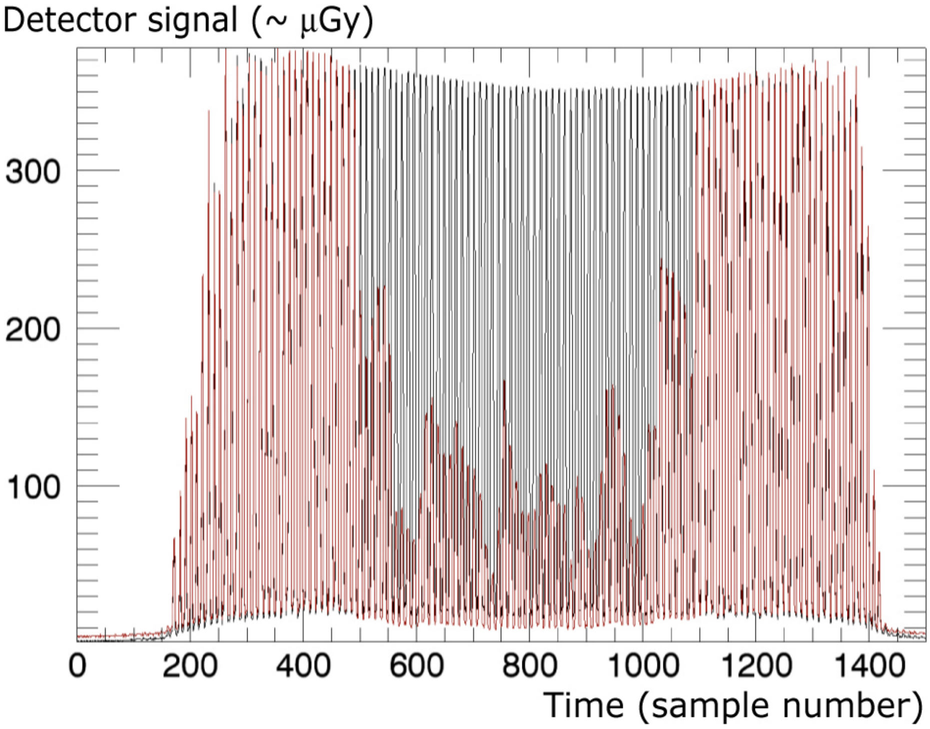

Figure 7.6: Raw data from one detector during the empty scan (black) and during the phantom scan (red).

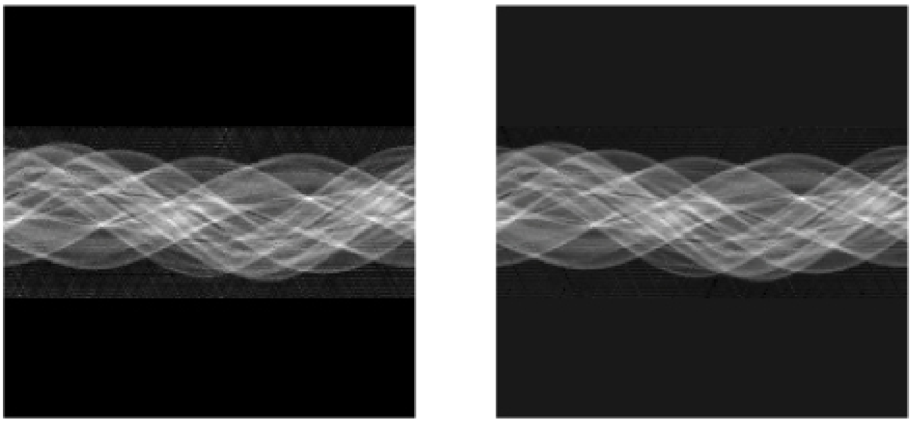

Figure 7.7: [`07-s3.pdf`] The sinogram obtained from the scan of the three peppers (left) and the same one after correcting the Radon data using the empty scan (right). Note that the background signal almost dissapears, whereas the pepper structures remain the same.

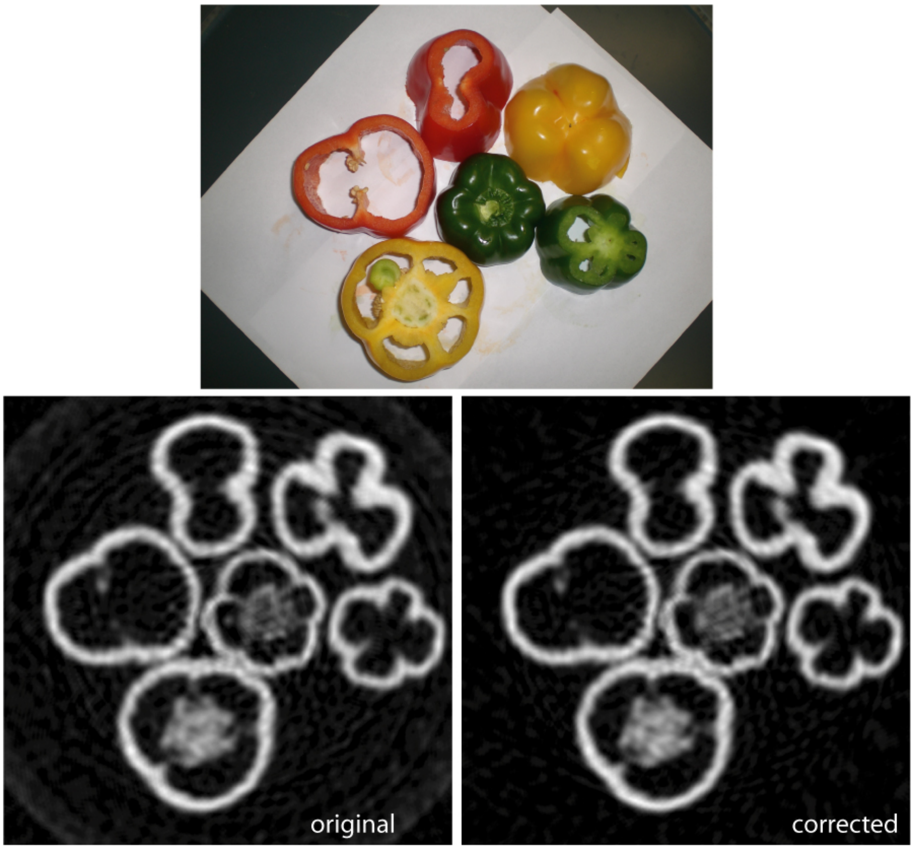

Figure 7.8: The phantom consisting of slices of three peppers (top) and its reconstruction from the original sinogram (bottom left) and from the background corrected sinogram (bottom right).

7.1.3 Image quality assessment

As explained in section 5.2.2, quantitative assessment of the image quality is possible e.g. using the two semi-circle phantoms. The raw data from one detector in each case are shown in figure 7.9. The corresponding sinograms are shown in the top part of each graph. The reconstructions of both phantoms are shown in figure 7.11. Observe that most artefacts are not appearent anymore once the residual negative values are set to zero, as explained in the first page of this chapter.

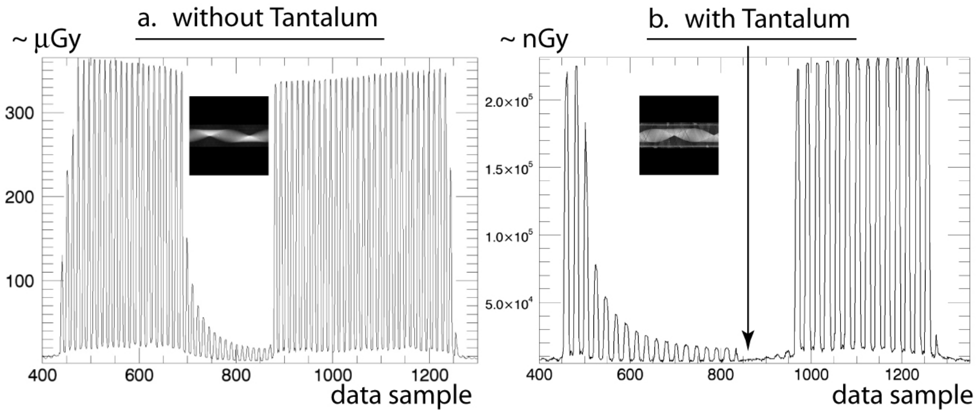

Figure 7.9: The relevant section of the **raw data from one detector** and the sinograms from the plexiglas semi-circles. **a.** without the Ta-sheet and **b.** with the Ta-sheet.

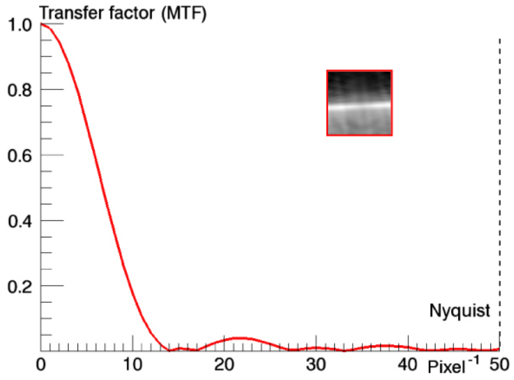

Figure 7.10: Measurement of the MTF using using the shown region from the reconstruction with the Tantalum sheet, as described in section 5.2.2.

The Modulation Transfer Function (MTF) from the reconstruction with the Ta-sheet is shown in figure 7.10. It was calculated following the method described in section 5.2.2. The object of these measurements was to find a quantitative way to compare measurements carried out using our device, especially when comparing these results with the ones obtained using both detector sets in the clinic (see next section). However, a rigorous image quality analysis would need a more comprehensive study including the different sources of noise (from the data and the electronic, independently of the noise from the reconstruction algorithm), and the calculation of the MTF from oversampled reconstructions of edge profiles. This analysis has been set out of the scope of this work.

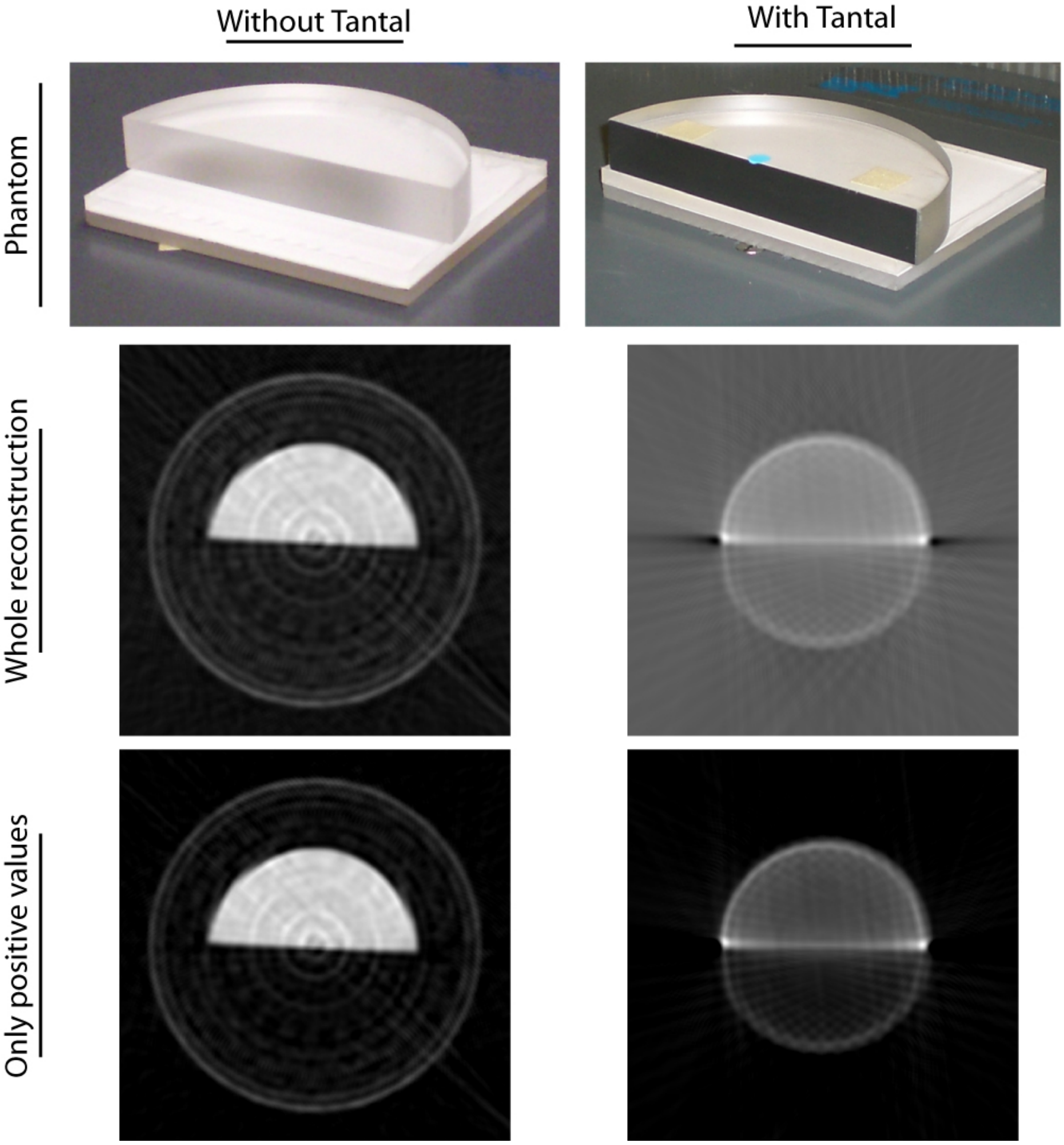
Without Tantal
With Tantal
Phantom
Whole reconstruction
Only positive values

Figure 7.11: [`07-semicircle.pdf`] **The semi-circle phantoms and their reconstructions** only from mask-detector data.

7.2 Results from the set-up with flat panel detector

In the clinic, we used a flat panel detector to simulate the arc. Thus, we obtained the two independent reconstructions (section 7.2.1) and also arranged the sinograms to obtain the final combined reconstruction of the head slice phantom (section 7.2.2).

7.2.1 The two independent data sets

The two kinds of data acquired with the mask and the arc detectors for the head slice phantom are shown in figure 7.12. The peaks are cleaner in the arc data (figure 7.12 b.) because the images of the flat detector are acquired synchronised with the pulses of the source, that is, every 33 ms. In the case of the mask detectors (figure 7.12 a.), samples are acquired every 16 ms. Thus, useless null samples are generated which, of course, do not distort the values of the peak-integrals.

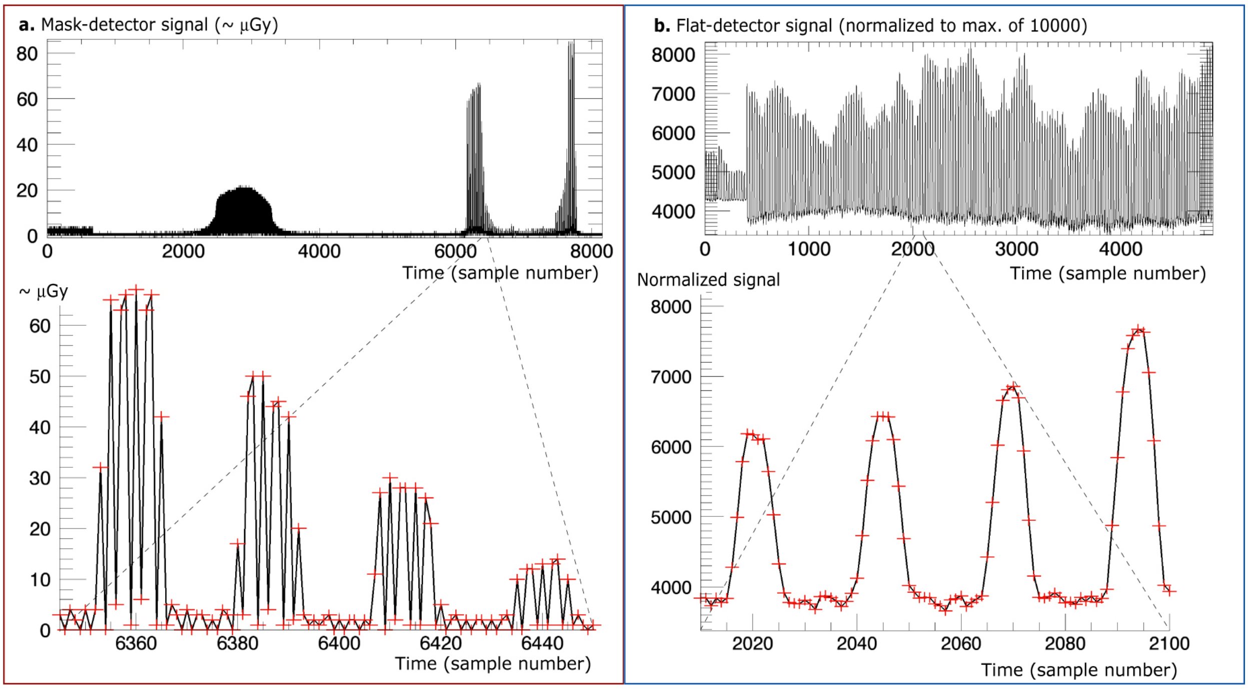

Figure 7.12: The data received **a.** by one mask-detector and **b.** by one bin of the flat detector. A small region of each sample has been magnified to better visualize the peaks that represent the "rays" (grey stripes in figure 2.3). Each red "+" sign represents one single data sample.

The two independent sinograms and the two resulting reconstructions obtained with the set-up in the clinic are shown in figure 7.13 and figure 7.14. According to the theory, the reconstruction from the arc detectors has lower resolution but higher contrast and lower noise [de las Heras 08a][1].

---

[1] This result was presented with a talk at the SPIE Medical Imaging Conference in February 2008 in San Diego (California, USA) and it was nominated to the Michael B. Merickel Best Student Paper Award.

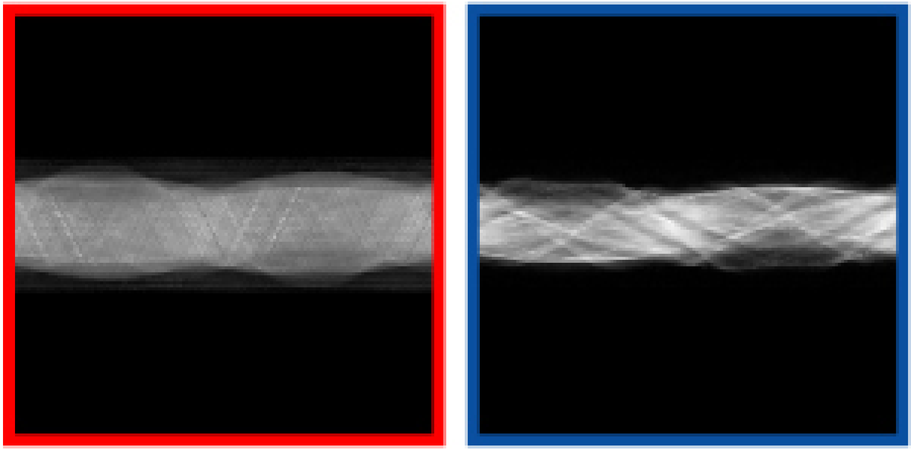

Figure 7.13: [`07-sin12.pdf`] **Left:** Sinogram of the head slice phantom from mask detectors. **Right:** Sinogram from the flat panel arc detectors.

The results using this set-up for the second time, including an empty scan, are shown in figure 7.15. This second scan of the head-slice is not only useful for the correction of the external ring artefacts, but also to check the reproducibility of our image quality. However, this time we saved only the treated images instead of the original ones. Therefore, the soft tissue in the reconstruction of the second kind was better reconstructed in the first case (figure 7.14). Observe also that the empty scan does not bring any visible improvement to this reconstruction, This is due to the careful step of “binning”, described in section 6.1.2.

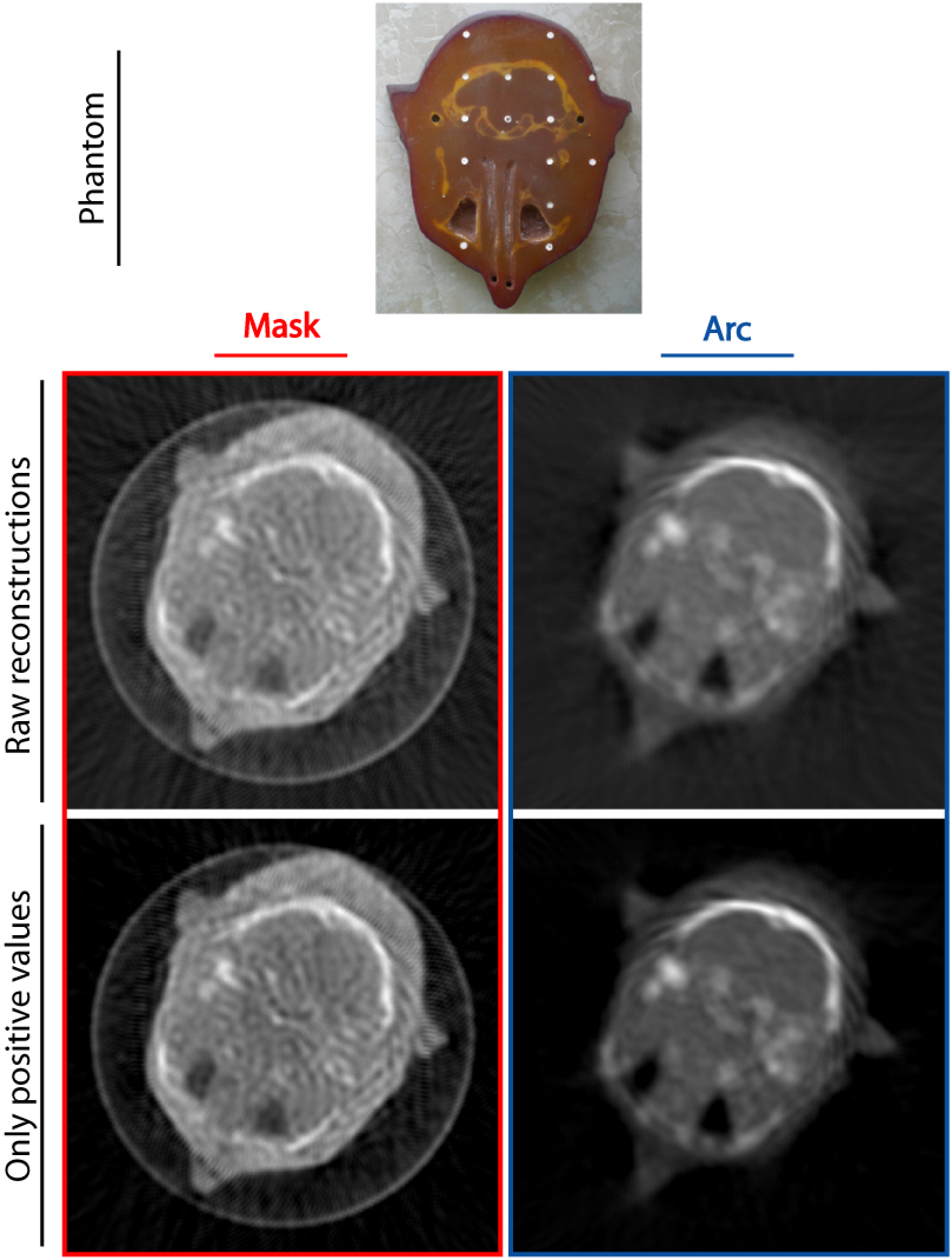
Phantom
Mask
Arc
Raw reconstructions
Only positive values

Figure 7.14: [`07-rec12.pdf`] The first reconstructions of the head slice phantom.

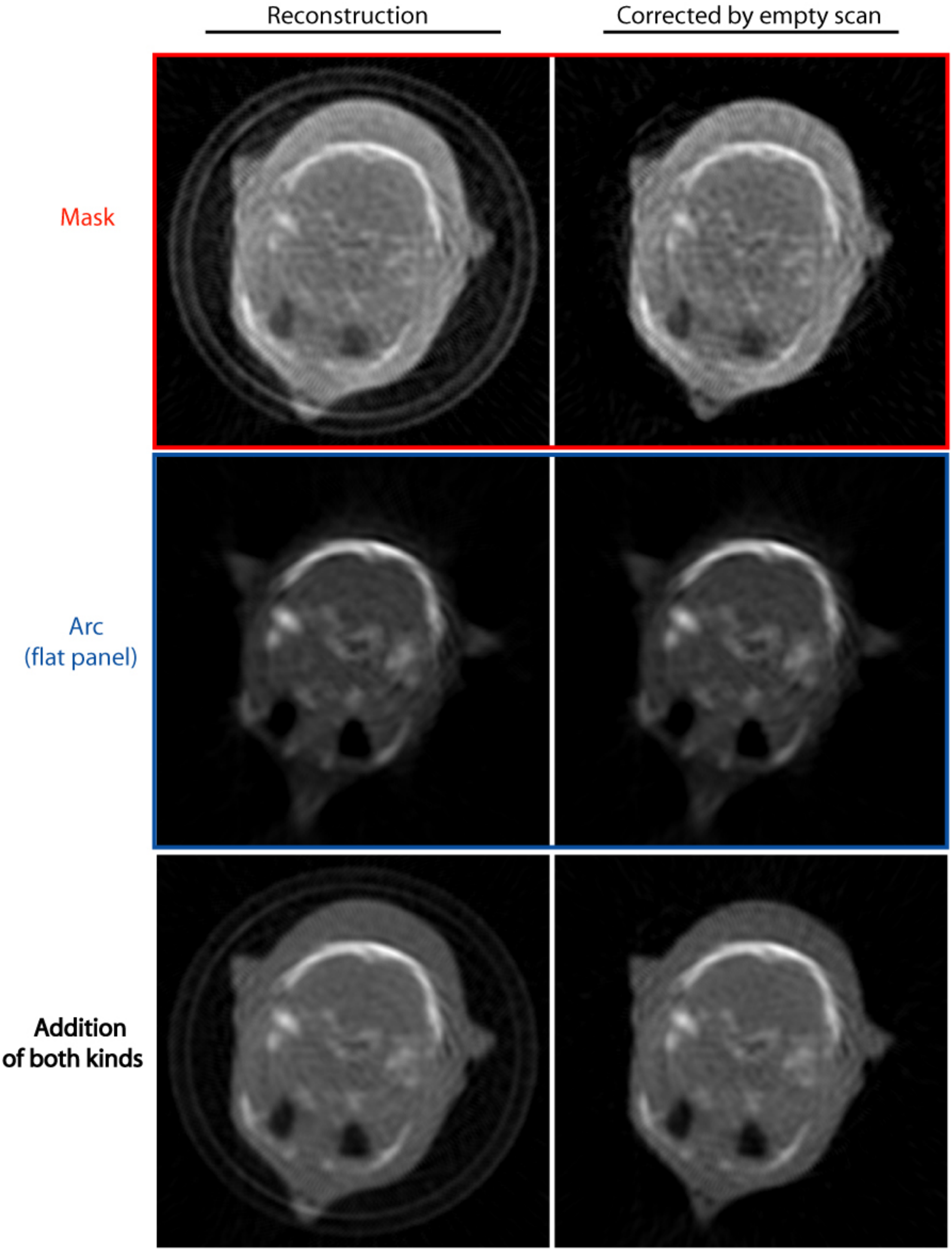
Reconstruction
Corrected by empty scan
Mask
Arc
(flat panel)
Addition
of both kinds

Figure 7.15: [`07-corr1.pdf`] The empty scan correction applied to the mask-data (top), the arc-data (middle) and the addition of both (bottom). The negative pixels have been set to zero in all images.

7.2.2 The final combined reconstruction

In both cases (with and without the empty scan), we obtained the complete sinogram joining both kinds of data together. In the first case without empty scan, all reconstructions can be seen in figure 7.16. Note the ring-artefacts, which were the reason that motivated the empty scan and will be discussed in section 8.2.1.

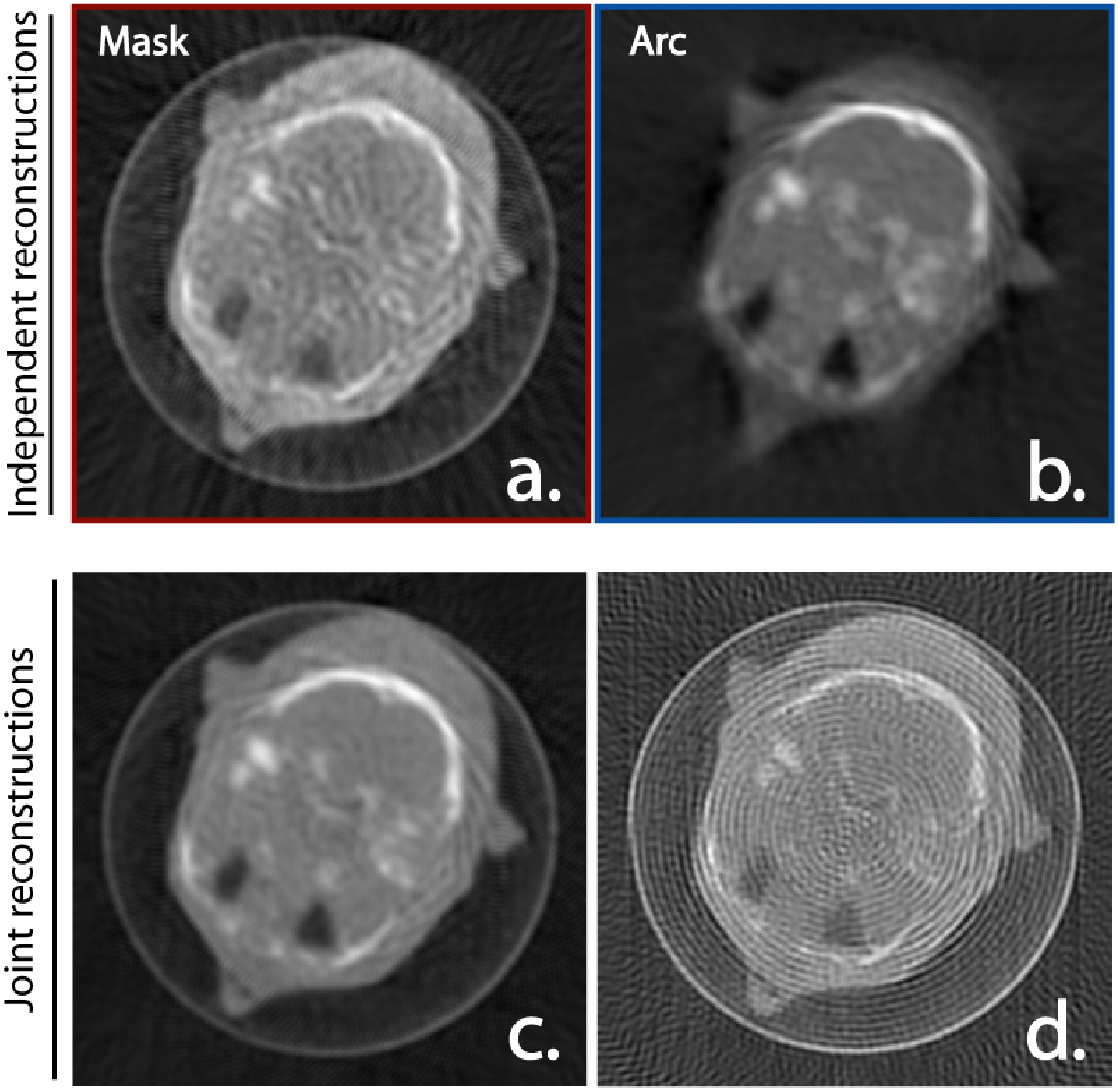

Figure 7.16: [`07-recons.pdf`] **The reconstructions of the head slice**. **a.** The reconstruction from the mask detectors. **b.** The reconstruction from the arc detectors. **c.** The simple addition of both reconstructions (after being normalised to have an equal maximum), which is useful to check the same orientation of both images. **d.** The final reconstruction from the complete sinogram.

The corresponding complete sinogram is shown in figure 7.17.

In the second case, i.e. with the correction from the empty scan, the combined reconstruc-

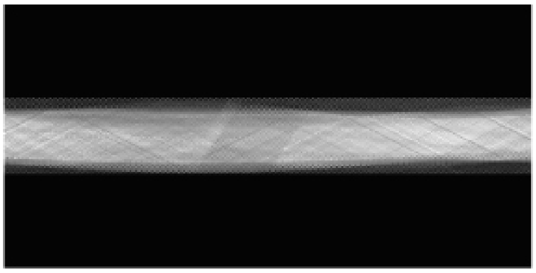

Figure 7.17: [`07-sinog12.pdf`] **The complete sinogram**, containing the data from both sinograms together. The different sensitivities of the detectors acquiring each kind of data produce stripes in this sinogram, which appear as ring-artefacts in the reconstruction.

tion is shown on the left of figure 7.18. In the middle of figure 7.18 you can see that only the large, outer ring-artefacts are avoided through the empty scan, whereas the smaller, regular ring-artefacts remain. These artefacts are the main drawback of the experimental set-up used in this work, and they will be discussed later in chapter 8. One can only “clean up” the image by applying an appropriate filter, as shown on the right in figure 7.18. Expanding the sinogram and reconstructing from the expanded sinogram is equivalent to applying a low-pass filter, which deletes the lowest frequencies present in the image. Such a filter is especially effective against regular structures like the ring-artefacts, but it blurs the image and can thus remove useful information. It is therefore not recommendable for clinical images.

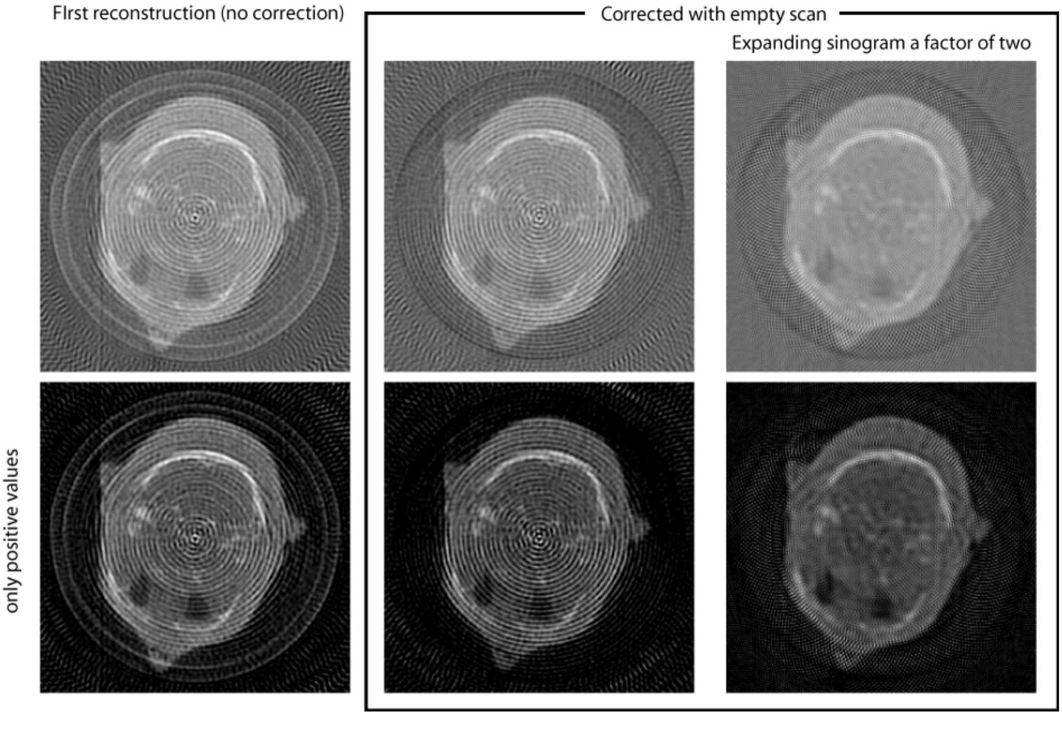
FIrst reconstruction (no correction)
Corrected with empty scan
Expanding sinogram a factor of two
only positive values

Figure 7.18: [`07-corr4.pdf`] **Left**: Complete reconstructions after the second measurement. **Middle**: Complete reconstructions after the empty scan correction. **Right**: Expanding the sinogram by a factor two is like filtering away the regular ring-structures.

Chapter 8

Discussion

This chapter discusses the results obtained with the test device developed in this work.

Section 8.1 comments on the quality of our reconstructions. Section 8.2 enumerates the drawbacks of the simplified test device. This section includes numerous tasks that should still be performed in this project. The results of the dosimetric radiation transport simulation are discussed in section 8.3, along with an experimental comparison between our algorithm OPED and the conventional FBP. In section 8.4, we briefly describe two unexpected obstacles that were encountered when using the clinical C-arm device, which we had not anticipated in the beginning. Finally, taking all this points into account, next chapter gives suggestions to construct an optimized prototype in the future.

8.1 Image Quality

Reconstructions from the first set-up (mask detectors only)

The visual quality of the reconstructions using only the ring-data (especially the one of the peppers), is surprisingly good regarding that they are obtained with only 197 projections and 82 rays per view in the case of the peppers[1].

The reason that the reconstruction of the peppers from our constructed test-device is better than the reconstructions of the other phantoms lies in the optimal absorption of the peppers for the available source and detectors. The detected peaks are much easier to recognise (figure 7.6) and integrate than in the case of the other phantoms, and therefore the structures in the sinogram are much better defined (figure 7.7).

The artefacts observed in these reconstructions are typical in low-resolution reconstructions. For example, they are also present in the reconstruction from the prototype of Inverse Geometry CT-scanner developed recently by the team of Norbert Pelc at the Stanford University [Schmidt 06], as you can observe in figure 8.1. These artefacts appear due to the approximations carried out when data have a low resolution.

Reconstructions from the second set-up (mask and arc detectors)

As noticed in section 2.1.2, the reconstruction from data obtained with the mask detectors (figure 7.16 a.) has a better resolution than the one obtained with the flat panel from the arc data (figure 7.16 b.). This arc-reconstruction has less noise and better contrast (note

---

[1] For comparison, the original Hounsfield's prototype of 1971 took 160 parallel readings through 180°, each 1° apart [Hounsfield 73].

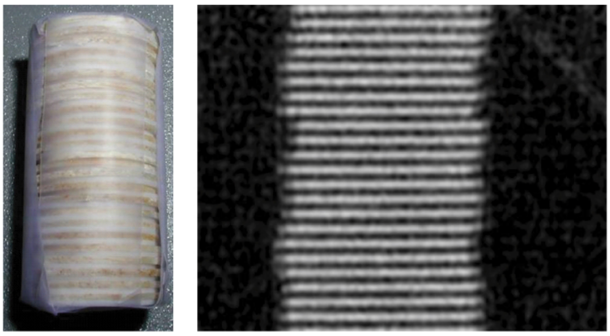

Figure 8.1: [`08-Rec_IGCT.pdf`] Results from a recent study with Inverse Geometry CT [Schmidt 06]. **Left**: The phantom used in the study is a cylinder made up of dense discs, separated by less dense material. **Right**: The reconstruction of its central longitudinal slice, obtained by the test-device used in the study. Note the same kind of artefacts as in our reconstructions (especially visible in the dark regions).

for example the darker regions of air). This is mainly due to the double collimation of the rays arriving at the flat panel, which reduces the amount of scattered radiation reaching this detector. The simple addition of both reconstructed images does not result in an improvement of the resolution (figure 7.16 c.). On the other hand, in the image reconstructed from the combined sinogram (figure 7.16 d.), an increase in resolution can be observed, since the edges of the structures seem to be better defined than in any other of the reconstructions.

Nevertheless, this last claim might still be an illusion due to the clear ring-artefacts. These are due partly to the different sensitivities of the two sets of detectors (even though the independent sinograms have been normalized to have the same maximum value before being rearranged together), and partly to the spline-interpolation scheme of the missing 25 % of arc data (about the need for this interpolation, see section 2.1.2). The regular ring-artefacts can be filtered away expanding the sinogram by a factor of two and reconstructing again, as shown in figure 7.18. However, a prototype with the same kind of detectors in the arc and in the mask is necessary to completely avoid these artefacts. This might be difficult for technical reasons and because of the shields needed.

8.2 Drawbacks of the test-device developed in this work

Several measures can be undertaken to further improve the quality of the reconstructed images. What our simplified test-device lacks is summarised below. Suggestions to solve or reduce each of these points in the future are enumerated in section 9.2.

1. The most important of all disadvantages of our demonstrator is that the ring detector and the external detector are not of the same kind. Therefore, it is impossible to match both responses perfectly and ring-artefacts appear in the final reconstruction (figure 7.16 d.).

   Design of the ring:

2. Our mask-ring is made up of only 197 detectors, which correspondingly acquire only 197 views in the ring. The number of views in the final sinogram is 394, adding the contribution from the arc. For comparison, the number of views acquired in a conventional CT-scanner is around 4000 distributed over 360°.

3. The thickness of the shieldings is larger than the effective surface of the detectors. As a result, 75% of the photons are lost during measurements with our demonstrator, as explained in section 2.1.3 and discussed later in section 9.2. Of those photons, 1/3 are are absorbed in the shieldings before entering the mask and 2/3 are lost due to the small efficient surface of the detectors.

4. The feature described in section 2.1.1 to substract the scattered radiation and thus potentially correct for scatter noise has not yet been explored with experimetal data. In the case of our single-slice demonstrator, this correction seems to be impossible to apply, because the portion of scattered photons in the plane of the scintillators is too small (the radiation passing through the shieldings is larger, see section 3.3).

5. The mask-ring was designed for 2-D reconstructions only.

   Construction of the ring:

6. Not all windows have exactly the same size, because they were fabricated manually. These irregularities cause stripes in the sinograms (figure 7.13) and ring-artefacts in the reconstructions. They can be partly corrected performing the empty scan (see figures 7.8 and 7.15), and taking only a small number of data around the maximum of the peaks during the step of integration of both types of detector data.

7. Furthermore, the shape of the shieldings was designed for a distance of 1 m from the ring-center to the source, but this distance varied in every experiment, and thus the artefacts are different in each reconstruction.

8. Despite great care, it was not possible to set all scintillator crystals in exactly the same plane manually, as explained in section 5.4.2.

   Whole assembly

9. The position of the source focal spot is known only approximately, both in the first set-up as in the clinical C-arm device. This poses a problem to determine the position of the central ray, whose exact position is important for the reconstruction algorithms.

10. The source of the first set-up has a very low power (maximum current of 10 mA), thus the scans using this source needed two hours to let a significant amount of photons reach the detectors.

11. The clinical device has a pulsed source and is not prepared for long periods of radiation. Therefore, it is necessary to start and stop the irradiation 13 times to get a full scan. These series must be joined manually afterwards (see section 5.4.4), which is time-consuming and inexact.

12. The time needed for a scan using this second set-up was also very large (about an hour) because, for this test of principle, we wanted to observe the form of the peaks in both types of data (figure 7.12). Nevertheless, to acquire one pulse per peak would have been enough to obtain a good reconstruction because the power of this source satisfies the clinical needs (current intensities of more than 200 mA).

8.2.1 Different detector sensitivities

The different sensitivities of the detectors is a drawback of our test device that needs a longer discussion.

On the one hand, the sensitivity of the flat panel detector elements are very different from the mask detectors, even though they are both made of CsI. Apart from that, the mask detectors also have different sensitivities among themselves.

The detector elements of the flat panel have a very different sensitivity from the sensitivity presented by the ring detectors. In the examples of raw data depicted in figure 8.2, you can observe that the lowest and highest readings are in a very different relation to each other in each case. Using the minimum values as a reference level, we have in each case,

$$\text{Mask-detector: } \frac{\text{highest absorption - minimum}}{\text{lowest absorption (air) - minimum}} = \frac{3}{86} \longrightarrow 3\%$$

$$\text{Flat panel element: } \frac{\text{highest absorption - minimum}}{\text{lowest absorption (air) - minimum}} = \frac{2100}{4800} \longrightarrow 44\%$$

It may practically not be possible to calibrate both detector sets to give the same reading at the same dose, because the clinical device normalizes the data automatically, as described in section 8.4.2[2].

The mask detectors show differences among themselves because they come from two different production lots [Sunde 06]. We have found two different behaviours in the sensitivities of the ring-detectors, as shown in figure 8.3. Unfortunately, RADCAL Corp. could not say which detectors correspond to which lot, or how many there are of each kind, These differences generate inclined stripes in the sinogram (figure 7.3) or horizontal lines in the fan-data (see figure 6.2 after the step of peak integration), especially in the case where the phantoms present high absorption.

8.3 Comparison to conventional devices

Simulated comparison

The image in the middle of figure 3.1 shows that the version of OPED for the complete sinogram, written by the author in IDL-language, gives a similar image quality as the one of the reconstruction obtained using FBP (bottom left in figure 3.1). Therefore, this version of OPED is correct, even though it has not been optimized yet. Furthermore, this OPED reconstruction proves that the ring-artefacts obtained in the final reconstruction of the experimental data cannot come from a mistake in the OPED-code.

On the other hand, the reconstruction obtained using the CT D'OR geometry, on the right of figure 3.1, does not show either a significant loss of image quality, even though it has been obtained after setting to zero and interpolating 1/4 of the pixels in the fan-data, as described in detail in section 3.1.

Experimental comparison

We have reconstructed our experimental mask data of the peppers using a standard FBP-algorithm. The results are compared in figure 8.4. You can observe a blurring in the external

---

[2] In order to make a proper calibration, it should be possible to check the original values in the look-up table of the flat-panel detector system, but unfortunately we had no access to it.

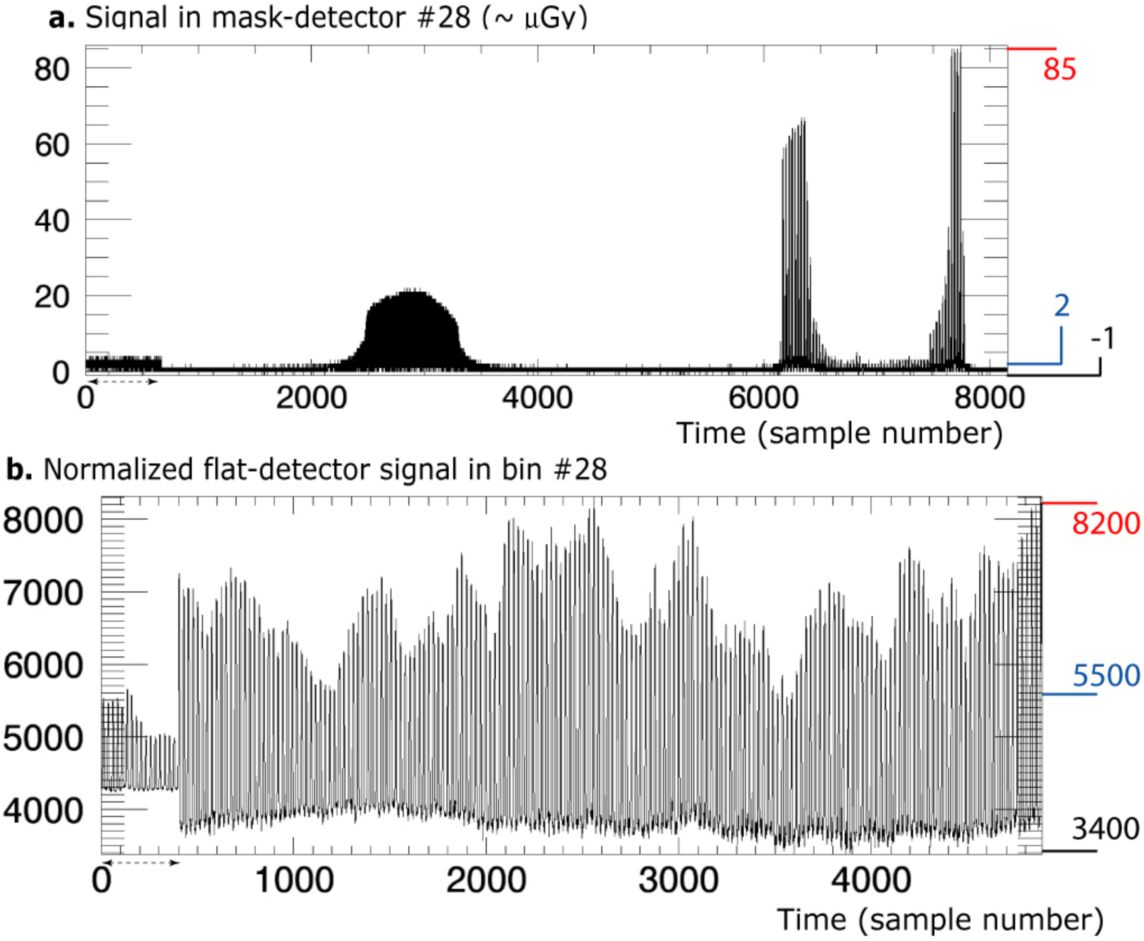

Figure 8.2: **One example of raw data from one mask-detector (above) and one element of the flat panel (below)**. The maximum and minimum readings are marked in red and blue. The absolute minimum, corresponding to a position where the detector is shielded, is marked black. The first series of this measurement, indicated with double arrows under the x-axis, was recorded with a different radiation quality by mistake.

part of the image obtained with FBP. This is a typical effect of the data-rebinning necessary for FBP, because the rebinned data are more spaced in the outer part of the image, as shown in figure 8.5. This effect is increased by larger fan-angles, which is, however, not the usual case of clinical devices. This rebinning is not necessary in the framework of OPED, as explained in section 2.2.

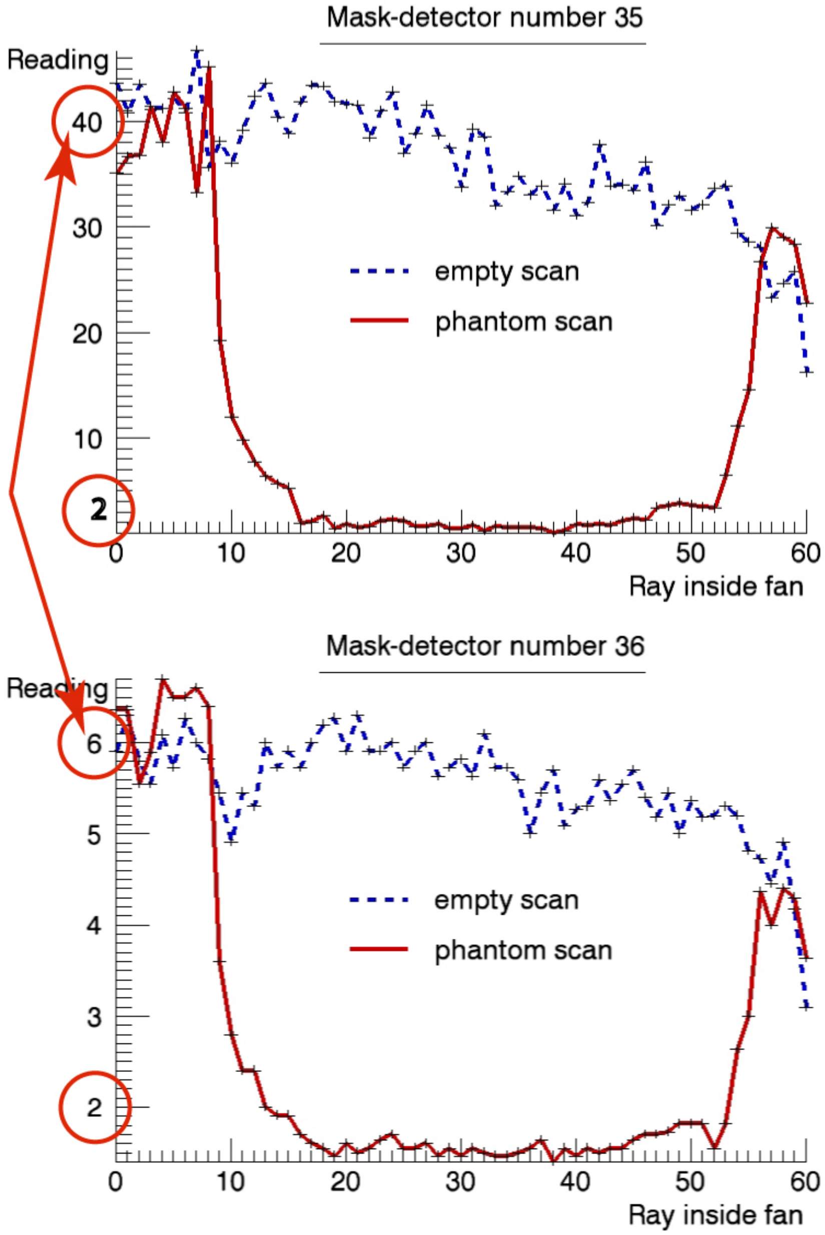

Figure 8.3: The different sensitivities among the mask detectors can be clearly observed in the example of these two detectors, whose sensitivities are different by a factor of 6. Note that the minimum value is in both cases around 1, whereas the maximum value is almost 7 times larger in the upper case. The clear decreasing tendency in both graphs is explained below in section 8.4.1.

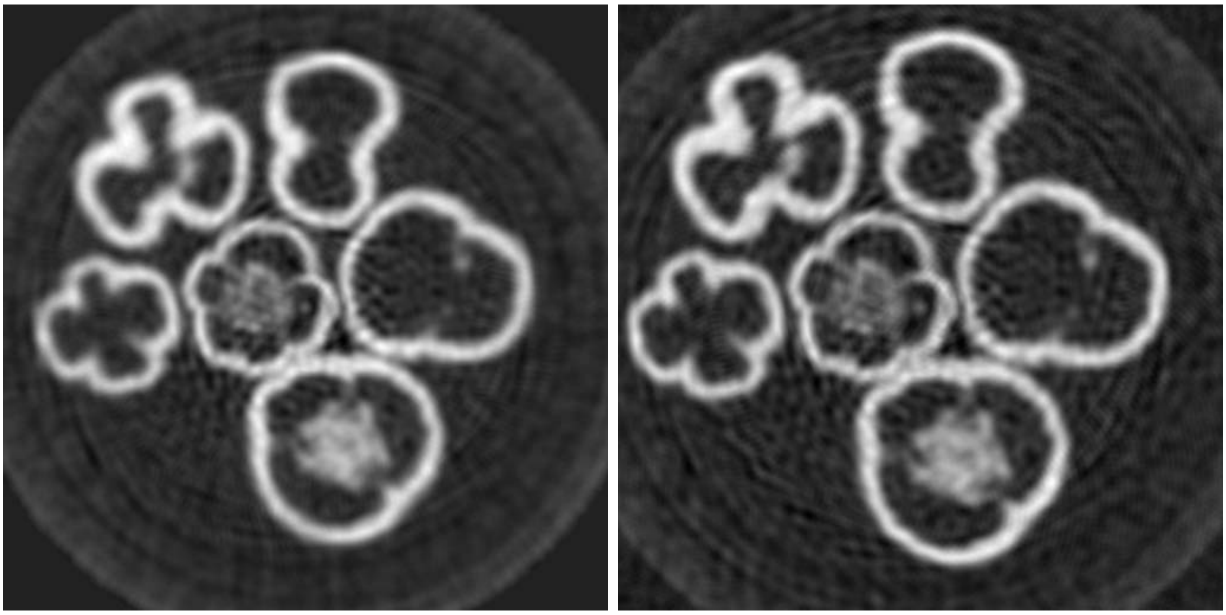

Figure 8.4: Reconstruction of the data from the 2-D scan of the peppers obtained using FBP (left) and OPED (right).

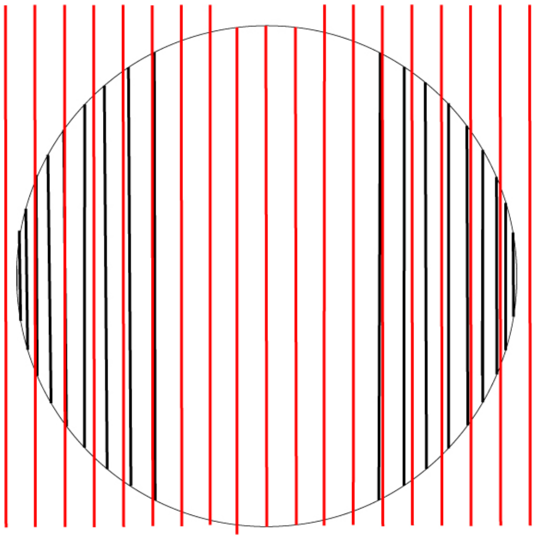

Figure 8.5: **Rebinning to equi-distant rays** (shown in red) is carried out in the framework of FBP. You can see that they are more distant from each other in the outer part of the image as the rays used in the geometry of the system OPED-CT D'OR (shown in black). In the centre of the image, the resolution is almost the same.

8.4 Problems with the clinical C-arm device

During the analysis of the clinical data, we discovered two features of the C-arm device, which resulted in additional uncertainties in the obtained reconstructions.

8.4.1 Heel effect

We discovered an asymmetric distribution of the intensity in the beam of the C-arm of about 30%. The Heel effect [Oldnall 08] observed in the C-arm was measured both in the flat panel as in the mask detectors (see figure 8.6) This effect is physically produced by the different path-lengths that the photons travel through the anode material, which is shorter on the side of the cathode, and therefore the photon-fluence on this side is higher.

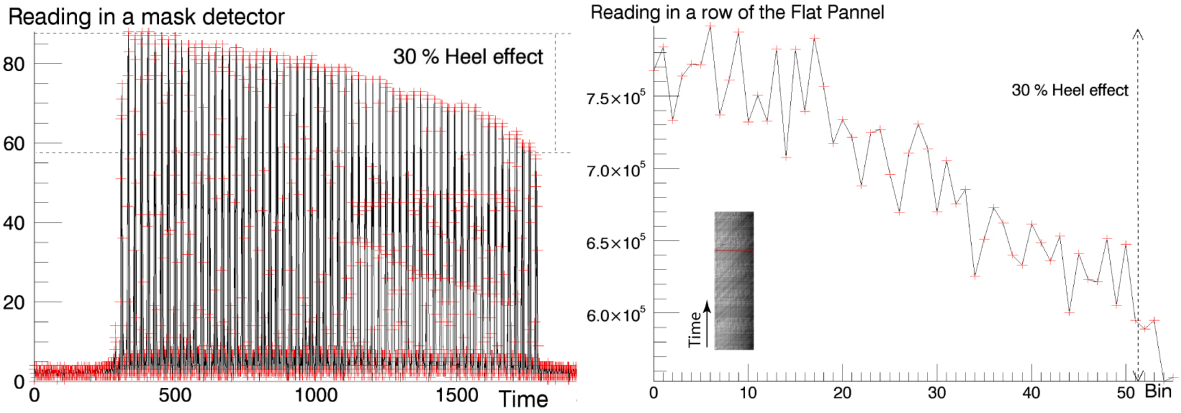

Figure 8.6: **The Heel effect in the ELEVA C-arm device**, observed by the integrated data during the empty scan (where the intensity should always be constant). **Left**: Measurement of a mask-detector over time. The photon fluence is clearly lower on the right part of the beam. **Right**: Measurement from the Flat panel at a single moment. This precise moment is marked in red in the matrix of the whole fan-data, shown on the left bottom corner. The photon fluence at the flat panel is also 30 % lower on the right part of the beam.

8.4.2 Automatic brightness normalization

To carry out a simultaneous calibration of both the mask detectors and the flat panel detectors, we obtained the readings in both detector sets at two given radiation qualities, using two different filters at the source. We discovered another feature of the software that processes the images in the clinical device. The maximum grey value of any image is always normalized to a reading of 10000 units, independent of the dose received at that point. Furthermore, this correction is included even if the device is forced to keep the raw data, not the processed data. Given that the flat panel works in such a “black-box manner”, it was even more difficult to match its measurements with the ones from the mask detectors.

Chapter 9

Summary and Outlook

This work presents an alternative scanning geometry for Computed Tomography with Double Optimal Reading, called CT D'OR. With this geometry, the Radon data are acquired after the X-ray beam is collimated through a special mask, which enables an efficient data collection and may reduce the patient dose. We have demonstrated with a test-device that the scanning geometry CT D'OR acquires data for two independent and complementary reconstructions. Additionally, we have shown with a Monte Carlo simulation that the image quality attained using this scanning geometry is equivalent to the one attained by conventional geometries.

The last aim of this work is to serve as a starting point for the construction of a future device that can contribute to reduce the increasing radiation exposure due to medical imaging applications to the population in industrialized countries.

9.1 Experimental dosimetric comparison

On a short term, there is an additional test that should be carried out using our simplified test-device: an experimental dosimetric comparison of the CT D'OR geometry with conventional geometries. For this purpose, two consecutive scans should be performed:

1. In the first place, one should scan a phantom with our clinical set-up (section 5.4.4) and record the dose placing TLD's (ThermoLuminescence Dosimeters) into or on the surface of the phantom, to measure either absorbed dose or patient entrance dose (or both). This phantom should optimally contain structures that allow the quantitative analysis of the reconstruction quality. After this measurement, one should remove the mask detectors without moving either the phantom or the Clinical C-arm, and replace the TLD's.

2. In the second place, we should do the same scan acquiring the same amount of radiation pulses as we have acquired previously, this time using only the flat panel to collect the data. Care must be taken to use the same detector resolution[1] to guarantee equal data quality for both scans. Nevertheless, the absence of the mask ensures that the radiation received by the phantom is now twice as much as before. The same horizontal portion of the images should be used to obtain a second sinogram, which in this case represents the data from a conventional CT-scan with the same data quality as the test-device developed in this work.

---

[1] This can be achieved by grouping the pixels of the flat panel in regions of the same size as the arc-bins that we had in the first scan. Additionally, the same number of pulses that conformed a peak in the case of the CT D'OR data should be added into a single ray in the second scan to have the same sampling-frequency.

One can then reconstruct the images using the same reconstruction algorithm and verify quantitatively the similar quality of the images. The dose difference can be measured using the TLD's.

9.2 Suggestions for an improved prototype

Each of the following suggestions refers to the corresponding drawback described in section 8.2.

1. The prototype should have the same type of detector-elements in the mask and in the arc. This will allow to obtain more homogeneous sinograms and thus ring-free final reconstructions. Ultra Fast Ceramic, a sintered ceramic gadolinium oxysulfide (Gd_2O_2S) material, has proved superior to other alternatives in the latest years [Kalender 05].

   Design of the ring:

2. Current CT devices acquire the equivalent to 4000 views over 360°, or 2000 views over 180°. A future prototype for CT D'OR should have about the same number of detectors in the mask, which may be a challenge for current technologies because the detectors should be separated by less than 0.1°.

3. The area of the detectors should be as similar as possible to the area of the shieldings, thus losing a minimal amount of information[2]. Non-circular, but flatter mask-detectors are required for this purpose, because they will be easier to shield on one side.

4. In a larger future prototype carrying out measurements of larger phantoms in 3-D and using thicker shieldings, the correction for the scattered radiation may be easier.

5. 3-D reconstructions could have been possible designing an empty ring, where the object could be shifted slowly during the irradiation, just as the table in modern CT's move thorugh the gantry. This way, we could have checked both the spiral and step-and-shoot methods for data acquisition.

   Construction of the ring:

6. The source, the mask and the arc of a future prototype should be assembled together, allowing for the usual rotation of the arc and the source inside the gantry, but always at a fixed distance to the mask.

7. The shieldings of the mask detectors should be fabricated industrially with exactly the same form, taking into account the fixed geometry suggested in the previous point.

8. A future design should contain precise slits that enable an exact vertical alignment of the detector elements in the same plane (in the same way that the plexiglas ring contains very precise holes to keep the detectors at equidistant positions).

   Whole assembly:

---

[2] This information loss, however, does not mean an inneficient use of the dose, because the photons are absorbed in the shieldings before entering the patient. Of course, the efficienct area of the detectors should also be as high as possible to make the best use posible of the photons transmitted through the patient, but this is not a specific problem of the CT D'OR geometry.

9. A new prototype should include a set of lasers (as modern CT devices do) to mark the trajectories of the central rays of the beam. Alternatively, the radiation field can be mapped with a fluorescent screen to find this central rays accurately. This would be unnecessary if a fixed device is manufactured, as suggested above in 6.
10. The X-ray source should have enough power and use continuous radiation during a full rotation of 360° of the device, just as modern CT's do.

Standard phantoms should enable a rigorous quantitative image analysis and comparisons with commercial devices, once the quality of the images is comparable to the ones from conventional devices.

Bibliography

[AAPM 08] Task Group 23 AAPM. *The measurement, reporting and management of Radiation Dose in CT.* In: AAPM report 96. AAPM College Park, MD 2008.

[Bachvalov 87] N. S. Bachvalov, N. P. Zidkov and G. M. Kobelkov. Chislennye metody. Nauka Moscow 1987.

[Barrett 04] H. H. Barrett and K. J. Myers. Foundations of image science. John Wiley & Sons, Inc Hoboken 2004.

[Berenson 08] Alex Berenson and Reed Abelson. *Weighing the Costs Of a Look Inside the Heart* (front page) New York Times, June 29. `http://www.nytimes.com/2008/06/29/business/29scan.html?partner=rssnyt` 2008.

[BfS 08a] BfS. *Einführung zum Thema "Ionisierende Strahlung".* Bundesamt für Strahlenschutz. `http://www.bfs.de/de/ion/einfuehrung.html` 2008.

[BfS 08b] BfS. *Radiation exposures from medical applications.* Bundesamt für Strahlenschutz. `http://www.bfs.de/de/bfs/druck/uus/jb06_Teil_B_IV.pdf` 2008.

[BMU 06] BMU. Umweltradioaktivität und Strahlenbelastung im Jahr 2006, Parlamentbericht. Bundesministerium für Umwelt Berlin 2006.

[Boseley 07] Sarah Boseley. *Call to stop whole body scans for the 'worried well'.* The Guardian (UK) **20th December** 2007.

[Brenner 07] D.J. Brenner and E. J. Hall. *Computed tomography: an increasing source of radiation exposure.* N Engl J Med. **357** 2277–84 2007.

[Brix 05] G. Brix, E. Nekolla and J. Griebel. *Strahlenexposition von Patienten durch diagnostische und interventionelle Röntgenanwendungen.* Radiologe **45** 340–9 2005.

[Brooks 76] R. A. Brooks. *Principles of computer assisted tomography (CAT) in radiographic and radioisotopic imaging.* Phys Med Biol. **21** 689–732 1976.

[Cormack 63] A. M. Cormack. *Representation of a function by its line integrals, with some radiological applications.* J Appl Phys. **34** 2722–7 1963.

[Cormack 92] A. M. Cormack. *75 years of radon transform.* J Comput Assist Tomogr. **16** p. 673 1992.

[Dainty 74] J. C. Dainty and R. Shaw. Image science. Academic Press London 1974.

[Davison 81] M. E. Davison and F. A. Grünbaum. *Tomographic reconstructions with arbitrary directions.* Comm Pure Appl Math. **34** 77–120 1981.

[de las Heras 07] H. de las Heras, O. Tischenko, B. Renger, Y. Xu and C. Hoeschen. *Modelling and testing of a non-standard scanning device with dose reduction potential.* In: SPIE Medical Imaging, edited by Jiang Hsieh and Michael J. Flynn, vol. **6510** of *Proc. SPIE* 6510–137 [Honourable Mention Poster Award] 2007.

[de las Heras 08a] H. de las Heras, O. Tischenko, W. Panzer, Y. Xu and C. Hoeschen. *Experimental proof of an idea for a CT-scanner with dose reduction potential.* In: SPIE Medical Imaging, edited by Jiang Hsieh and Ehsan Samei, vol. **6913** of *Proc. SPIE* 6913–06 [Nominated to Best Student Paper Award] 2008.

[de las Heras 08b] Hugo de las Heras, O. Tischenko, Y. Xu and C. Hoeschen. *Comparison of interpolation functions to improve a rebinning-free CT-reconstruction algortihm.* Zeitschrift für Medizinische Physik **18** 7–16 2008.

[Dunkl 01] C. F. Dunkl and Y. Xu. *Orthogonal polynomials of several variables.* In: Encyclopedia of Mathematics and its Applications vol. **81**. Cambridge Univ. Press 2001.

[EUCT 07] EUCT. *CT Safety and Efficacy: A Broad Perspective.* A research Project of the European Commission coordinated by J. Geleijns 2005-2007.

[Feinendegen 05] L. E. Feinendegen. *Evidence for beneficial low level radiation effects and radiation hormesis.* Br J Radiol. **78** 3–7 2005.

[Flohr 06] T. G. Flohr, C. H. McCollough, H. Bruder, M. Petersilka, K. Gruber, C. Süß, M. Grasruck, K. Stierstorfer, B. Krauss, R. Raupach, A. N. Primak, A. Küttner, S. Achenbach, C. Becker, A. Kopp and B. M. Ohnesorge. *First performance evaluation of a dual-source CT (DSCT) system.* Eur Radiol. **16** 256–68 2006.

[Flohr 07] T.G. Flohr, K. Stierstorfer, C. Süss, B. Schmidt, A.N. Primak and C.H. McCollough. *Novel ultrahigh resolution data acquisition and image reconstruction for multi-detector row CT.* Med Phys. **34 (5)** 1712–23 2007.

[Frigo 06] Matteo Frigo and Steven G. Johnson. *FFTW.* `http://www.fftw.org/` version 3.1.2, 23 June 2006.

[Fujita 92] H. Fujita, D. Y. Tsai, T. Itoh, K. Doi, J. Morishita, K. Ueda and A. Ohtsuka. *A simple method for determining the modulation transfer function in digital radiography.* IEEE Trans Med Img. **11** 34–9 1992.

[Goske 08] M.J. Goske and K.E. Applegate et al. *The Image Gently campaign: working together to change practice.* Am J Roentgenol. **190(2)** 273–4 2008.

[Hall 08] E. J. Hall and D. J. Brenner. *Cancer risks from diagnostic radiology.* Br J Radiol. **81** 362–378 2008.

[Herman 76] G. T. Herman and A. Lent. *Iterative reconstruction algorithms.* Comp Biol Med. **6** 273–294 1976.

[Hoeschen 02] Christoph Hoeschen. *Das reale Strahlenbild bei einer Röntgenaufnahme.* PhD thesis Fakultät für Naturwissenschaften der Otto-von-Guericke-Universität Magdeburg May 2002.

[Hounsfield 73] G. N. Hounsfield. *Computerized transverse axial scanning (tomography). 1. Description of system.* Br J Radiol. **46(552)** 1016–22 1973.

[Hsieh 03] Jiang Hsieh. *Computed Tomography: Principles, Design, Artifacts, and Recent Advances.* In: Monographs vol. **PM114**. SPIE press 2003.

[ICRP 07] ICRP. *Managing Patient Dose in Multi-Detector Computed Tomography (MDCT).* In: Annals of the ICRP vol. **102**. Elsevier Exeter 2007.

[IEC 03] IEC. *Medical electrical equipment Characteristics of digital X-ray imaging devices Part 1: Determination of the detective quantum efficiency.* In: International Standard vol. **IEC 62220-1:2003(E)**. International Electrotechnical Comission Geneva, Switzerland 2003.

[IPEM 97] IPEM. *Catalogue of diagnostic spectra and other data.* Published by the Institute of Physics and Engineering in Medicine (UK) 1997.

[Kachelrieß 00] M. Kachelrieß, S. Schaller and W. A. Kalender. *Advanced single-slice rebinning in cone-beam spiral CT.* Med Phys. **27** 754–72 2000.

[Kak 88] A. C. Kak and M. Slaney. Principles of computerized tomographic imaging. IEEE press New York 1988.

[Kalender 90] W. A. Kalender, W. Seissler, E. Klotz and P. Vock. *Spiral volumetric CT with single-breathhold technique, continuous transport, and continuous scanner rotation.* Radiology **176** 181–3 1990.

[Kalender 05] W. A. Kalender. Computed Tomography. Publics Corporate Publishing Erlangen 2005.

[Kalender 06] W. A Kalender. *X-ray computed tomography.* Phys Med Biol. **51** R29–R43 2006.

[Kawrakow 03] I. Kawrakow and D. W. O. Rogers. *The EGSnrc code system: Monte Carlo simulation of electron and photon transport.* In: PIRS Report vol. **701**. National Research Council of Canada, Ottawa, Canada 2003.

[Krane 88] K. S. Krane. Introductory nuclear physics. John Wiley & Sons, Inc. USA 1988.

[Lakshminarayanan 75] A. V. Lakshminarayanan. *Reconstruction from divergent ray data.* In: Tech. Rep. 92. Dept of Computer Science. SUNY State Univ. of New York at Buffalo 1975.

[Lee 04] C. I. Lee, A. H. Haims, E. P. Monico, J.A. Brink and H.P. Forman. *Diagnostic CT scans: assessment of patient, physician, and radiologist awareness of radiation dose and possible risks.* Radiology **231(2)** 393–8 2004.

[Marr 74] R. Marr. *On the reconstruction of a function on a circular domain from a sampling of its line integrals.* J Math Anal Appl. **45** 357–374 1974.

[Matej 96] S. Matej and R. M. Lewitt. *Practical considerations for 3-D image reconstruction using spherically-symmetric volume elements.* IEEE Trans Med Img. **15:1** 68–78 1996.

[NHS 05] NHS. *Siemens Somatom Sensation Open CT scanner technical evaluation,* Report 05071 November 2005.

[Nickoloff 87] E. L. Nickoloff. *Measurement of the PSF for a CT scanner: appropriate wire diameter and pixel size.* Phys Med Biol. **33 , No. 1** 149–155 1987.

[Oldnall 08] Nick Oldnall. *Xray2000: Anode Heel effect.* `http://www.e-radiography.net/radtech/a/anode$\_$heel.htm` Last update: 25/06/2008.

[Orth 08] R.C. Orth, M.J. Wallace and M.D. Kuo. *C-arm Cone-beam CT: General Principles and Technical Considerations for Use in Interventional Radiology.* J Vasc Interv Radiol. **19(6)** 814–20 2008.

[Piroddi 04] R. Piroddi and M. Petrou. *Analysis of irregularly sampled data: a review.* In: Advances in Imaging and Electron Physics vol. **132** 109–165. Academic Press London 2004.

[Press 07] Associated Press. *Report Links Increased Cancer Risk to CT Scans.* New York Times **November 29** 2007.

[Rabin 07a] R. C. Rabin. *With Rise in Radiation Exposure, Experts Urge Caution on Tests.* New York Times **19th June** 2007.

[Rabin 07b] Roni Caryn Rabin. *Demasiadas pruebas radiologicas? (Translated from New York Times [Rabin 07a]).* El Pais **26th June** 2007.

[Radon 17] J.H. Radon. *Über die Bestimmung von Funktionen durch ihre Integralwerte längs gewisser Mannigfaltigkeiten.* Ber. vor Sächs. Akad. Wiss. **69** p. 262 1917.

[Rögener 07] W. Rögener. *Seduced by the power of images (in German: Verfürt von der Macht der Bilder).* Sueddeutsche Zeitung **80** p. 5th/6th April 2007.

[Schlattl 06] H. Schlattl, O. Tischenko, Yuan Xu and C. Hoeschen. *Scatter noise correction of detector signals for projection-based imaging* European patent application PLA 06A01 Submitted on 10/02/2006.

[Schlattl 08] H. Schlattl and C. Hoeschen. *The built-in capacity of CT D'Or's static ring for scatter correction.* In: SPIE Medical Imaging, edited by Jiang Hsieh and Ehsan Samei, vol. **6913** of *Proc. SPIE* 6913–52 2008.

[Schmidt 04] T.G. Schmidt, R. Fahrig, N.J. Pelc and E.G. Solomon. *An inverse-geometry volumetric CT system with a large-area scanned source: a feasibility study.* Med Phys. **31(9)** 2623–7 2004.

[Schmidt 06] T.G. Schmidt, J. Star-Lack, N.R. Bennett, S.R. Mazin, E.G. Solomon, R. Fahrig and N.J. Pelc. *A prototype table-top inverse-geometry volumetric CT system.* Med Phys. **33(6)** 1867–78 2006.

[Shepp 74] L. Shepp and B. Logan. *The Fourier reconstruction of a head section.* IEEE Trans Nucl Sci. **NS-21** 21–43 1974.

[Silver 05] M.D. Silver. *Comment on "an inverse-geometry volumetric CT system with a large-area scanned source: a feasibility study" [Med. Phys. 31, 2623-2627 (2004)].* Med Phys. **32(2)** p. 635 (see author reply on p. 636) 2005.

[Späth 95] H. Späth. One-dimensional spline interpolation algorithms. A K Peters Ltd Wellesley 1995.

[Sunde 06] Paul Sunde 2006. Private Communication with RADCAL Corp. 07/12/06.

[Theocharopoulos 07] N. Theocharopoulos, J. Damilakis, K. Perisinakis and N. Gourtsoyiannis. *Energy imparted-based estimates of the effect of z-overscanning on adult and pediatric patient effective doses from multi-slice computed tomography.* Med Phys. **34(4)** 1139–52 2007.

[Tischenko 06] O. Tischenko, Y. Xu and C. Hoeschen. *A new scanning device in CT with dose reduction potential.* In: SPIE Medical Imaging, edited by Jiang Hsieh and Michael J. Flynn, vol. **6142** of *Proc. SPIE* 893–899 2006.

[Tischenko 07] O. Tischenko, Y. Xu and C. Hoeschen. *Imaging method and device with dual reading scanner* European Patent EP1780676, filed on 25/10/2005 published on 02/05/2007.

[Tischenko 08] O. Tischenko, H. de las Heras, Y. Xu and C. Hoeschen. *An x-ray 2-D scanner with fixed geometry and double reading system.* To be published 2008.

[Trott 08] Michael Trott. *Gibbs Phenomena for 1-D Fourier Series* The Wolfram Demonstrations Project. `http://demonstrations.wolfram.com/GibbsPhenomenaFor1DFourierSeries/` 2008.

[Voress 07] M. Voress. *The increasing use of CT and its risks.* Radiol Technol. **79(2)** 186–90 2007.

[Wall 06] B. F. Wall, G. M. Kendall, A. A. Edwards, S. Bouffler, C. R. Muirhead and J. R. Meara. *What are the risks from medical X-rays and other low dose radiation?* Br J Radiol. **79(940)** 285–94 2006.

[Webb 90] Steve Webb. From the watching of shadows. The origin of radiological tomography. IOPP Bristol 1990.

[Wikipedia 08] Wikipedia. *Tantalum - Wikipedia, The Free Encyclopedia* 2008. [Online; accessed 24-September-2008].

[Wootters 81] W. K. Wootters. *Statistical distance and Hilbert space.* Phys Rev D. **23** 357–62 1981.

[Worgul 07] B.V. Worgul, Y.I. Kundiyev, N.M. Sergiyenko, V.V. Chumak, P.M. Vitte, C. Medvedovsky, E.V. Bakhanova, A.K. Junk, O.Y. Kyrychenko, N.V. Musijachenko, S.A. Shylo, O.P. Vitte, S. Xu, X. Xue and R.E. Shore. *Cataracts among Chernobyl clean-up workers: implications regarding permissible eye exposures.* Radiat Res. **167(2)** 233–43 2007.

[Xu 06a] Y. Xu. *A new approach to the reconstruction of images from Radon projections.* Adv Appl Math. **36** 388–420 2006.

[Xu 06b] Y. Xu, O. Tischenko and C. Hoeschen. *A new reconstruction algorithm for Radon Data.* In: SPIE Medical Imaging, edited by Jiang Hsieh and Michael J. Flynn, vol. **61422** of *Proc. SPIE* 791–798 2006.

[Xu 07] Yuan Xu, O. Tischenko and C. Hoeschen. *Method and device of reconstructing an (n+1)-dimensional image function from Radon data* United States Patent and Trademark Office US60/640,426. European patent EP1677253, filed on 30/12/2004 published on 19/09/2007.

[zu Castell 08] Wolfgang zu Castell and Rick Beatson. *Scattered data reconstruction of Radon data for Computer Tomography.* Seventh International Conference on Mathematical Methods for Curves and Surfaces, Tonsberg, Norway June 26-July 1, 2008.

List of Figures

1.1 A visualized cardiac-CT 1
1.2 A typical CT scanner. 2
1.3 Origination of a fan-data matrix 3
1.4 Intrinsic problems of current CT-devices 4
1.5 Sources of Radiation 5
1.6 Dose in X-ray examinations 6
1.7 Theories for the effects of low-dose radiation 7

2.1 The idea of CT D'OR 10
2.2 Data acquisition (ideal case) 11
2.3 **The schemas of the data acquired** by one single detector 12
2.4 Three views of each kind of data 13
2.5 Data acquisition (real case) 13
2.6 Loss of data 14
2.7 Relation OPED-CT D'OR through three fans of data 16
2.8 All rays of both geometries 16
2.9 Ray geometry 17
2.10 FBP needs rebinning, whereas OPED does not 21
2.11 Comparison of OPED and FBP 22

3.1 Results from the simulation 29
3.2 Correction for scattered radiation 30
3.3 Attempts to correct scatter 30

4.1 The origin of the missing cells 32
4.2 Justification of the interpolation process; reconstructions from fan data with $N = 111$ fan views made with different values of n. 32
4.3 The need for interpolation 33
4.4 The different interpolating functions 35
4.5 Inhomogeneity measured through the MTF 36
4.6 Drawback of the 1-D interpolation 36
4.7 Explanation of the drawback 37
4.8 Artefacts in homogeneous regions 39
4.9 Bar diagram of relative NMSE decrease 40
4.10 Behaviour of parametric splines 41
4.11 Modulation Transfer Function and Profiles 43
4.12 2-D interpolation methods for Shepp-Logan Phantom 44
4.13 The local method applied to the checkers Phantom 45

5.1 Design of the demonstrator (top view) 50
5.2 Design of the demonstrator (side view) 50
5.3 The ports of the photodiodes and close-up view of one detector 51
5.4 Design of the cases for the photodiodes 51
5.5 Construction of the mask at the factory 52
5.6 Organic test objects 54
5.7 The semi-circle phantoms without and with Tantalum 55
5.8 The head-slice from an Alderson-Rando phantom 55
5.9 A CT-scan of the head-slice 55
5.10 Set-up for the detector calibration 56
5.11 Spectra for calibration 57
5.12 Response dependence with the applied voltage 57
5.13 Response dependence with the filtration 58
5.14 Slopes of calibration and F-factors 59
5.15 Set-up for the first measurement 60
5.16 Spectrum for measurements in SSDL 61
5.17 Set-up for empty scan measurement 61
5.18 Experimental set-up in the clinic 62
5.19 Intensity from the pulsed source 63
5.20 Dimensions of Flat detector 63
5.21 DICOM image acquired by the flat panel 65

6.1 Data processing 68
6.2 Data treatment: example for mask data 69
6.3 Data treatment: example for gantry data 71
6.4 Data processing for whole data 73
6.5 Data treatment: example to join both sinograms 74

7.1 Raw data during the pepper-scanner. 76
7.2 The first reconstruction of CT D'OR 77
7.3 Sinogram from the resin phantom 77
7.4 Data from the resin phantom with pattern 78
7.5 Reconstruction of resin phantom 78
7.6 The data for the three peppers 79
7.7 The sinogram from the three peppers 80
7.8 The phantom made of slices of three peppers 80
7.9 Data from the plexiglas semi-circles 81
7.10 Measurement of the MTF using Ta-sheet 81
7.11 The reconstructions of the semicircles 82
7.12 One data sample of each type 83
7.13 Sinograms from the head slice phantom 84
7.14 Reconstructions from the head slice phantom 85
7.15 The empty scan correction 86
7.16 The final reconstruction 87
7.17 The complete sinogram 88
7.18 Correction 4: Expanding the sinogram 88

8.1 Reconstruction from IGCT demonstrator 90
8.2 The different sensitivities of both detector sets 93

8.3 The different sensitivities among the mask detectors 94
8.4 Experimental comparison of OPED and FBP 95
8.5 Parallel rays for FBP and for OPED 95
8.6 Heel effect in the C-arm 96

List of Tables

4.1 Phantom data and reconstruction parameters 34
4.2 Accuracy of the Shepp Logan phantom reconstructions. 42

5.1 The parameters employed in the calibration of the detectors 56
5.2 Calculation of the correction factor for the first 5 detectors. 59
5.3 Parameters of the measurements using the first set-up (in the GSF). 60
5.4 Parameters of the measurements in the Clinic. 66

Acknowledgements

I want to thank

- My PhD supervisor Herwig Paretzke and my direct supervisors Christoph Hoeschen and Oleg Tischenko for their experienced advice all along the PhD, as well as for the very sensible and careful corrections of this work.

- My mentor, Eliseo Vañó, for his continuous encouragement, even sometimes against his own wishes.

- The German Academic Exchange Service, DAAD, for the supervision, and the program Helmholtz-DAAD for the funding.

- Wolfgang Dietz, Peter Streitenberger and all the staff in the Werkstatt of our center. Peter suffered under the odour of the resin, had the patience to teach me everything I learnt there, and showed a great readiness to help every time I came with new queries.

- Bernhard Renger, who stayed long hours in the clinic with me, especially in the first tests.

- Wolfgang zu Castell and Rick Beatson for the interesting collaboration about 2-D interpolation and for their patience during my writing of this work.

- The PhD student Claudia Brunner, for the idea of adding columns to separate the bins in the flat-panel data, and the student Raphaela Anselman, winner of a price in “DFG-Jugend Forscht”, who helped me by calibrating the detectors of the first set-up.

- Werner Panzer, who helped me and Raphaela to carry out the dosimetry in the SSDL and held great conversations with me about Spain, international politics and German literature during the slow rotation of the ring.

- Yuan Xu, Felix Schöfer, Dieter Regulla, Mike Atkinson and Gunnar Brix for the corrections and fruitful conversations about some parts of this work.

- All the staff in the Medical Physics Group of the Helmholtz Zentrum München, who made my stay in Germany even nicer than I could have ever expected, and helped to destroy the prejudices that Spanish people have about the coldness of Germans.

- My housemates in the Student Hall at Felsennelkenanger, especially Christine Gau. They helped me by listening to my problems and asking basic questions that sometimes came up to be very helpful.

- Patricia Boya and all the colleagues and friends I met at the ESOF Conferences in Munich and Barcelona, for their support to my activities as a communicator of science, which keep me extra motivated in the world of research.
- My parents, because they did the most important of all.

Appendix

Appendix A

CsI(Tl)

Thallium doped Caesium Iodide

Properties

After Glow	Approx 2.0% after 2ms
After Glow	Approx 2.8% after 1ms
Cleavage Planes	None
Decay Constant (µs)	1.0
Density ($g.cm^{-3}$)	4.51
Dielectric Constant	5.65 at 1MHz (298K)
Emission Spectral Range (nm)	375 to 725
Gamma and X-ray absorption coefficients (cm^{-1})	0.48 at 660keV
Gamma and X-ray absorption coefficients (cm^{-1})	10.00 at 100keV
Light Escape Cone to Air (°)	34.1
Light Escape Cone to Glass (°)	57.2
Light Escape from one face to Air (%)	8.6%
Light Escape from one face to Glass (%)	22.9%
Melting Point (°C)	621
Optical Transmission Range	240nm to 70µ
Peak Scintillation Wavelength (nm)	565
Photons/MeV	52,000
Radiation Length (cm)	1.86
Refractive Index at peak emmission	1.78
Soluble in Alcohol	Yes
Specific Heat ($J.kg^{-1}.K^{-1}$)	0.048
Stability	Slightly Hygroscopic
Structure	BCC
Temperature Coefficient of Light Output ($\%.°C^{-1}$)	+0.32
Thermal Conductivity ($W.m^{-1}.K^{-1}$)	1.13 at 298K
Water Solubility (g/100ml H_2O)	44 at 273K
Youngs Modulus (GPa)	5.3

Data provided by ©1999 Hilger Crystals Ltd., E&OE

Physical and scintillation properties of CsI(Tl)			
Photons / MeV	45,000 ~ 65,000	Light output [NaI(Tl) = 100%]	50 % ~ 100 %
effective Z#	51	density	4.51 g / cm^3
melting point	621 °C	hardness [Moh]	2
hygroscopicity	slightly	peak wavelength	540 nm
decay constant	1,1 ns	reflactive index [@560nm]	1.79

Data provided by: **Proteus, Inc.**

PO.Box.747, 120 Senlac Hills Drive,
Chagrin Falls, Ohio 44022 U.S.A.

Phone# +1-440-247-1601
Fax# +1-440-247-1602

e-mail: pparkhurst@proteus-pp.com

Description

The MCN 323 metal-ceramic X-ray tube is a double pole tube which uses a specific ceramic material to insulate the positive and negative high voltage from the housing which is hold at ground potential. The MCN 323 has two focuses.

As the anode is loaded with positive high voltage potential the tube is cooled by insulating oil.

Technical data

X-ray tube data

Maximum tube voltage	320 kV =
Maximum tube loading	
Standard focus	320 kV x 13 mA = 4.16 kW
Small focus	320 kV x 3 mA = 0,96 kW
Duty cycle	
Standard focus	50% at all temperatures, exposure time ≤2 hours
Small focus	100% up till 40 °C
Anode material	tungsten
Anode angle	22°
Emergent beam angle	40°
Inherent filtration value	4 mm Beryllium fixed, (additional 3 mm Al, removable by tool)
Leakage radiation in 1 m distance from focus	<10 mSv/h
Minimum oil flow	22 l/min (>3.2 kW) 14 l/min (≤3.2 kW)
Max. cooling oil inlet temperature	50 °C
Oil pressure	≤850 kPa
Cooling oil	Shell Diala G (dehydrated), free of air bubbles
Surface temperature	≤85 °C
Weight with hand rings	35 kg

High voltage supply

Supply source	DC high voltage generator, symmetrically grounded
Resistor	33 kΩ
Preferably	diode-damping
High tension cable	R12 plug, fastening with screws
Length of cable	max. 20 m C=105 pF/m, min. 160 kV
Electrical shielding	all metal housing grounded

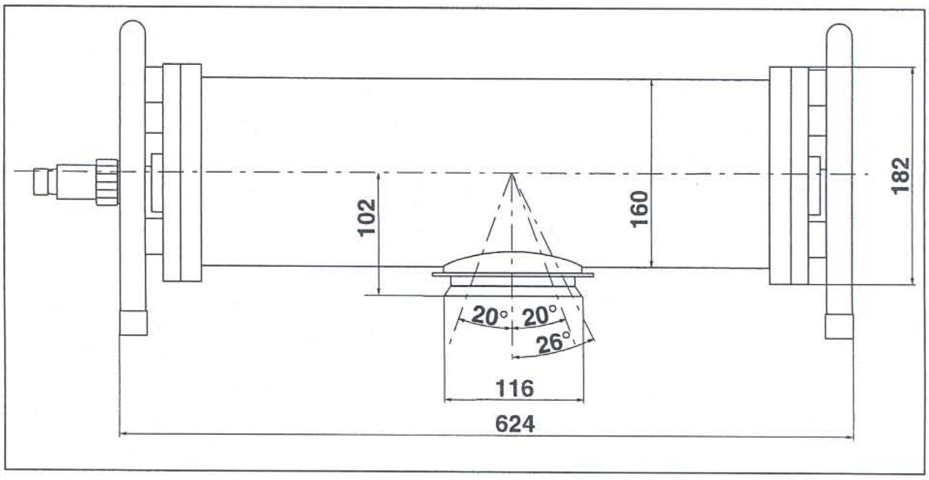

Dimensions in mm

Curriculum Vitae

Born: 25th June 1980
Address: HMGU – ISS
Ingolstaedter Landstr. 1
85764 Neuherberg
Germany

Telephone: +49 89 3187 3773

E-Mail: hugo.heras@daad-alumni.de

Hugo de las Heras

Education

1 / 8 / 2005 - today **PhD in Physics** – Technical University of Munich and Helmholtz Zentrum München – founded by German **Helmholtz-DAAD grant**.

6 / 1998 - 9 / 2004 **MSc in Theoretical Physics** – Univ. Complutense of Madrid (UCM).
Course: *Latin origins of scientific vocabulary* – UCM; 40 hours (2000).

9 / 2000 – 6 / 2001 **Erasmus grant** - University of Nottingham (UN), England.
Course: *Communication skills* – UN; 80 hours (2001)

Relevant Experience

9 / 2007 – 7 / 2008 **Weekly lab supervision** – Tech. Univ. München (Physics department).

9 / 2004 – 7 /2005 **Internship grant** - San Carlos University Hospital Madrid. Medical Physics Group.

1 / 2004 – 6 / 2004 **Collaboration grant** – Department of Theoretical Physics, UCM.

Languages

Spanish: Mother tongue.

English: Excellent level read, written and spoken (C2).
Certificate of proficiency in English - Cambridge University (June 2001).

German: Excellent level read, written and spoken (C2).
Zentrale Oberstufenprüfung – Goethe Institut (December 2008)
Course *"German for experimental Sciences"* – UCM; 80 hours (2002).

French and **Italian**: Good level spoken and read.

Computer Skills

Windows XP: MS-Office, **SPSS**, **LabView,** Adobe **Illustrator.**

Programming languages: **IDL, Fortran**, **Matlab**, **LaTeX**.

LINUX system: Basic knowledge.

Awards

2 / 2008 **Finalist Best Student Paper Award** – SPIE Medical Imaging Conference, USA.

9 / 2007 **EFOMP Congress Award (European Feds. of Medical Physics)** – Pisa, Italy

2 / 2007 **Poster Price Honourable Mention** – SPIE Medical Imaging Conference, USA.

9 / 2006 **Price to the best Young Researcher**- German Society of Medical Physics.

Other Interests

Swimming, theater playing, reading, travelling, science communication.

(List of Presentations and Publications in next pages)

Munich, 20th January 2009

List of scientific **Poster and Oral presentations** as first author (except where stated)

Date	Conference name - Place - Kind of presentation - Remarks
12th Nov 2008	School Orientation day - Helmholtz Zentrum München (Germany) – **Invited** talk and small-group seminars
18th July 2008	ESOF 2008 – Barcelona (Spain) - (volunteer in Outreach Activities)
18th Feb 2008	SPIE Medical Imaging - San Diego, California (USA) - Talk
19th Dec 2007	Medical Physics Seminar - German Cancer Research Center, Heidelberg (Germany) - **Invited** Lecturer
10th Dec 2007	Medical Physics Seminar - University Clinic Rechts der Isar, Munich (Germany) - **Invited** Lecturer
22nd Oct 2007	Course on Medical Imaging - Faculty of Medicine of the Complutense University, Madrid (Spain) - **Invited** Lecturer
25th Sep 2007	German-Austrian-Swiss Meeting of Medical Physics - Bern (Switzerland) – Poster (presented by Christoph Hoeschen)
20th Sep 2007	Xth EFOMP Congress (1st European Conference on Medical Physics) Pisa (Italy) - Talk
18th – 30th Mar 2007	WE-Heraeus Physics School - Bad Honnef (Germany) - short lecture
26th Mar 2007	DPG Meeting - Regensburg (Germany) - Talk – Presented by Christoph Hoeschen
17th Feb 2007	SPIE Medical Imaging - San Diego, California (USA) – Poster
20th Sep 2006	37th annual Meting DGMP - Regensburg (Germany) – Talk
15th July 2006	ESOF 2006 - Munich (Germany) - (only participant)
13th Mar 2006	DPG Meeting - Heidelberg (Germany) - Talk
13th Sep 2005	DGMP, EFOMP, IOMP Meeting - Nürnberg (Germany) – Poster from San Carlos Hospital in Madrid - (not first author)
27th Mar 2004	V edition Madrid for science - Madrid (Spain) – Talk and interpretation
17th Mar 2004	Astronomical seminar - Astronomical Society of Madrid, Madrid (Spain) **Invited** lecturer

Abbreviations:

SPIE: Society for Optical Engineering
EFOMP: European Federations of Organizations of Medical Physics
DPG: German Society of Physics
DGMP: German Society of Medical Physics
ESOF: European Science Open Forum
IOMP: International Organization for Medical Physics
UCM: Complutense University of Madrid (Spain)

List of **Publications**

Comparison of the interpolation functions to improve a rebinning-free CT-reconstruction algorithm Hugo de las Heras, Oleg Tischenko, Yuan Xu and Christoph Hoeschen. Paper 604 / 2006. Zeitschrift für Medizinische Physik, Z. Med. Phys. **18** (2008) 7-16.

Transition from screen-film to digital radiography: evolution of patient radiation doses at projection radiography Eliseo Vañó, José M. Fernández, José I. Ten, Carlos Prieto, Luciano González, Roberto Rodríguez, Hugo de Las Heras. Radiology, **243(2)** (2007) 461-6.

SPIE: Medical Imaging 2007. Punto de vista de investigadores pre-doc Hugo de las Heras and Andreu Nadal. Revista Española de Física Médica, REFM, **8(1)** (2007) 40-41.

Experimental proof of an idea for a CT-scanner with dose reduction potential Hugo de las Heras, Oleg Tischenko, Bernhard C. Renger, Yuan Xu, Christoph Hoeschen. **SPIE Medical Imaging (2008)**, 6913 - 06.

Modeling and testing of a non-standard scanning device with dose reduction potential Hugo de las Heras, Oleg Tischenko, Werner Panzer, Yuan Xu, Christoph Hoeschen. **SPIE Medical Imaging** (**2007)**, 6510 – 137.